

Columbia University
in the City of New York

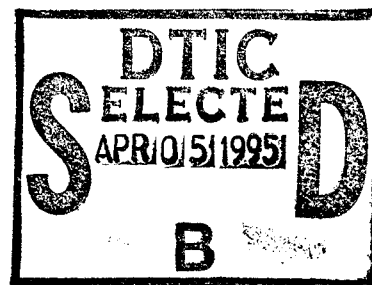
Theoretical and Experimental Research on a Millimeter-Wavelength Free-Electron Laser



Thomas C. Marshall

1995

19950403 105



Work Supported by ONR Grant N00014-89J-1652

Plasma Physics Laboratory

Department of Applied Physics

School of Engineering and Applied Science

Columbia University

New York, New York 10027

REPORT DOCUMENTATION PAGE			Form Approved OMB No. 0704-0188	
Public reporting burden for this collection of information is estimated to average 1 hour per response, including the time for reviewing instructions, searching existing data sources, gathering and maintaining the data needed, and completing and reviewing the collection of information. Send comments regarding this burden estimate or any other aspect of this collection of information, including suggestions for reducing this burden, to Washington Headquarters Services, Directorate for Information Operations and Reports, 1215 Jefferson Davis Highway, Suite 1204, Arlington, VA 22202-4302, and to the Office of Management and Budget, Paperwork Reduction Project (0704-0188), Washington, DC 20503.				
1. AGENCY USE ONLY (Leave blank)	2. REPORT DATE April 1995	3. REPORT TYPE AND DATES COVERED Feb.1, 1989-Jan. 31, 1995; Final		
4. TITLE AND SUBTITLE Theoretical and Experimental Research on a Millimeter-Wavelength Free Electron Laser		5. FUNDING NUMBERS		
6. AUTHOR(S) T. C. Marshall				
7. PERFORMING ORGANIZATION NAME(S) AND ADDRESS(ES) Department of Applied Physics Columbia University New York City, NY 10027		8. PERFORMING ORGANIZATION REPORT NUMBER Plasma Laboratory Report No. 128		
9. SPONSORING/MONITORING AGENCY NAME(S) AND ADDRESS(ES) Office of Naval Research, Physics Division 800 N. Quincy Street Arlington, VA 22217-5660		10. SPONSORING/MONITORING AGENCY REPORT NUMBER		
11. SUPPLEMENTARY NOTES				
12a. DISTRIBUTION/AVAILABILITY STATEMENT Approved for public release - distribution unlimited		12b. DISTRIBUTION CODE		
13. ABSTRACT (Maximum 200 words) Six years' research on the Columbia Free Electron Laser are summarized with an introduction and a selection of key reprints. Topics include: optical guiding, sideband instabilities, statistical properties of wiggler radiation, radiation pulses emitted from the FEL, superradiant and optical fiber models of radiation pulses, the inverse FEL accelerator experiment, angular steering of the FEL radiation pattern, and the travelling wave amplification of very short FEL pulses to very high power.				
14. SUBJECT TERMS Free Electron Laser Radiation			15. NUMBER OF PAGES	
			16. PRICE CODE	
17. SECURITY CLASSIFICATION OF REPORT Unclassified	18. SECURITY CLASSIFICATION OF THIS PAGE Unclassified	19. SECURITY CLASSIFICATION OF ABSTRACT Unclassified	20. LIMITATION OF ABSTRACT	

NSN 7540-01-280-5500

Standard Form 298 (Rev. 2-89)
Prescribed by ANSI Std. Z39-18
298-102

INTRODUCTION

This report is a summary of the principal research accomplishments completed under contract N00014-89J-1652 on experimental and theoretical research relating to Free Electron Lasers, in particular the millimeter-wavelength FEL facility at Columbia University. The research spans a period of approximately six years.

Following this introduction, the remainder of the report consists of a compilation of published research papers. These comprise a representative sample (but not complete) of the major research findings. Also not to be overlooked is that the research resulted in the award of seven doctorates, supported all or in part by the ONR. There now follows in this section an overview of these findings.

Section I consists of three papers on the subject of optical guiding, originating from prior ONR and NSF grants. The first paper expands on the results presented in an earlier Physical Review Letter, and demonstrates that optical guiding effects occur in a diffraction-dominated regime of "refractive guiding exponential growth" using spatial measurements of the transverse structure of the fields. The second and third papers describe the effect of optical guiding on the sideband instability frequencies, and therefore comprise an independent measurement of guiding in the regime of saturated growth.

Section II is a letter describing measurements of the statistical properties of wiggler radiation made on the Brookhaven storage ring. This is a report on an experiment which was motivated by earlier work on the photonics of the FEL by Bhattacharjee and Gjaja, in the preceding ONR grant.

Section III is comprised of five papers on radiation pulse effects in the FEL. The first paper is a reworking of the linear theory of superradiance which accounts for radiation spikes on or near short electron pulse FEL radiation. The second theory paper models the FEL as an optical fiber, and finds that inherent dispersive properties favor the production of solitary wave pulses of radiation. This idea was pursued experimentally in the next three papers: the first describes the initial discovery of short spiking pulses in our millimeter FEL, and the next two papers refine the measurements in connection with sidebands and "slippage", and compare data with the predictions of solitary-wave theory.

Section IV reports results from our "inverse FEL accelerator". This experiment was initially supported by the NSF and ONR, and now activity in free electron accelerators is supported at Columbia by the DOE, division of High Energy Physics. This paper is the first experimental proof of the IFEL principle, originally outlined by R. Palmer in 1972.

Section V is made up of two papers which reconfigure the undulator to achieve unusual radiation effects. The first deals with harmonic radiations and is a theory study. The second reports on a measurement in which the undulator is used to convert the FEL radiation into a mode which steers the radiation off-axis.

Section VI, the last paper, is a recent Physical Review Letter which describes how an undulator can be programmed so that a narrow optical pulse can be amplified to very high intensity - of the order of the electron beam intensity- while retaining a nearly Gaussian profile. The resultant pulses are ~ 350 fsec in the IR and ~ 50 psec at 200GHz; since the pulses are only a few wavelengths long, this technique may have application to impulse radar.

Further studies of the use of beam pre-bunching to achieve coherence and phase stability are being continued under a new ONR grant at present.

Accession For	
NTIS GRA&I	<input checked="checked" type="checkbox"/>
DTIC TAB	<input type="checkbox"/>
Unannounced	<input type="checkbox"/>
Justification	
By	
Distribution/	
Availability Codes	
Dist	Avail and/or Special
A-1	

Theory and observation of optical guiding in a free-electron laser

A. Bhattacharjee, S. Y. Cai, S. P. Chang, J. W. Dodd,
A. Fruchtman,* and T. C. Marshall

Department of Applied Physics, Columbia University, New York, New York 10027

(Received 5 June 1989)

Optical guiding in a Raman free-electron laser (FEL) is studied theoretically and experimentally. Two complimentary theoretical approaches to the problem of optical guiding in a waveguide containing a filamentary electron beam are given and shown to be in good agreement with each other in the exponential gain regime. Evidence for optical guiding of 2-mm-wavelength radiation along the electron beam in the Columbia University FEL is obtained experimentally by analysis of spatial "ring-down" data of the optical wave profile and compared with numerical simulations. These data are presented for the exponential gain regime. A similar experiment at signal saturation conditions shows a much less well-defined ring-down. We give plausible experimental as well as theoretical arguments why the ring-down pattern is less well defined. Based on the observations presented in this paper, it is not possible to validate optical guiding at saturation.

I. INTRODUCTION

In a free-electron laser (FEL), the electron beam is not only the source of energy for the radiation field, but can, in addition, distort the wave front and alter the phase velocity of the radiation. The modified index of refraction can then cause the optical beam to propagate almost self-similarly along the electron beam despite the presence of arbitrarily strong diffraction. This effect, known as optical guiding,¹⁻⁴ has been the subject of considerable theoretical research recently.⁵⁻¹³ Two qualitatively different mechanisms for guiding have been elucidated in the literature.¹⁴ The first one is gain guiding, in which loss of optical power by diffraction is compensated for by the amplification of the radiation. In order that gain guiding may dominate, a necessary condition is that the gain length be shorter than or comparable to the Rayleigh range for the radiation. The second mechanism, and more subtle than the first, is refractive guiding which can occur even if the gain length is larger than the Rayleigh range. The occurrence of refractive guiding involves the phase shift of the radiation. In the linear regime, the real and imaginary parts of the refractive index (n) characterizing the electron beam^{1,2,15,16} can, under certain conditions, satisfy the relation $\text{Re}n > 1$ due to the phase shift even when the gain, proportional to $\text{Im}n$, is negligible. When refractive guiding dominates, the self-similarity of the optical beam results from the interference of refracted wave fronts which compensate exactly for diffractive losses. Since refractive guiding does not rely on the presence of intrinsic gain, it can occur at saturation, which can be beneficial for the performance of long, "tapered" FEL's.

There have been a few experimental observations of optical guiding. The experiment at Los Alamos National Laboratory¹⁷ has shown a "bending" effect of the radiation contained in the optical resonator. Optical guiding influenced by gain guiding effects has been observed in

the Stanford University FEL.¹⁸ The MIT experiment,¹⁹ originally interpreted as evidence of optical guiding, is now understood to be wave-profile modification induced by electrostatic effects. For a valuable commentary on the Stanford and MIT experiments, the reader is referred to Ref. 20.

Experimental evidence of optical guiding obtained from the Raman FEL at Columbia has been reported recently.²¹ The experiment is done in a highly overmoded waveguide, and optical guiding is detected by measuring the spatial "ring-down" of the amplified radiation at a point downstream from the termination of the electron beam, using a waveguide probe. The measurements show that optical guiding occurs in the regime of exponential growth, under circumstances for which the Rayleigh range (~ 2.5 cm) is considerably shorter than the e-folding distance of power growth (~ 10 cm). The ring-down data at saturation are much less well defined, and we therefore make no claim on the validity of optical guiding at saturation based on those data. Apart from the spatial ring-down data, there is independent experimental evidence for refractive optical guiding in the Columbia experiment based upon observations of the FEL sidebands. The latter is described in detail in a companion paper,²² and will not be repeated here, except for the remark that the diagnostic for the guiding involves only the spectrum of the FEL radiation and is therefore entirely nonperturbing. In this paper, we amplify on our earlier work,²¹ and correct a flaw, pointed out by Fruchtman,²³ in our numerical work⁹ which neglected the effect of TM modes. (Fortunately, this effect does not alter qualitatively our earlier interpretation and conclusions.²¹) Our present numerical results, obtained by expanding the optically guided waves in a complete set of vacuum waveguide modes, is shown to be in agreement with Fruchtman's analysis in the exponential gain regime.

We now give a plan of this paper. In Sec. II, we describe the experimental setup. In Sec. II we formulate

TABLE I. Free-electron laser parameters.

Undulator period (helical)	1.7 cm
Undulator length	60 cm
Electron-beam energy	800 kV
Electron-beam pulse length	150 nsec
Beam current density	1–2 kA/cm ²
Electron-beam diameter	4 mm
Drift-tube (waveguide) diameter	18 mm
Effective “wiggler parameter” ($eB_w/k_w mc^2$)	0.2–0.4
FEL wavelength	1.9 mm

the nonlinear FEL equations required to study optical guiding in a waveguide environment by representing the optical wave in a complete set of TE and TM modes. These equations are used to simulate numerically the Columbia University experiment. In Sec. IV, we describe Fruchtmann's linear fluid theory applied to the Columbia University experiment, and demonstrate agreement of this calculation with the numerical results from the formulation described in Sec. III. In Sec. V we present experimental results together with simulation results both in the exponential gain regime and at saturation. We conclude in Sec. VI with a summary and a discussion of the implications of our results.

II. EXPERIMENTAL SETUP

A schematic of the experimental apparatus is shown in Fig. 1 and a set of typical parameters which characterized the FEL performance and geometry is given in Table I. The diode, accelerator, and electron-beam diagnostics have been described elsewhere.²⁴ Because of the 2-mm wavelength, the FEL operates as a traveling-wave amplifier of noise which is present at its input. This results in a statistical variation of the output power, requir-

ing the averaging of many shots taken under nearly identical accelerator conditions. To preserve the axisymmetry of the beam termination in the large waveguide, the beam strikes a polyethylene “witness plate” which permits approximately 80% of the incident radiation to pass through to the detector. This radiation is no longer optically guided, but its pattern of downstream interference is uniquely determined by the boundary condition at the beam termination. Figure 1 shows the setup where the spatial pattern of power in the waveguide following the termination of the electron beam is examined using a small “waveguide probe.” This probe consists of a dielectric needle horn inserted into a 2-mm-diam cylindrical waveguide which transports the radiation to a Schottky-barrier detector which is sensitive to short-wavelength radiation transmitted through a mesh filter. The waveguide probe is sensitive to radiation in a narrow forward-directed lobe of half-width 10°. The electromagnetic (EM) fields induce a wave on the dielectric element, which itself couples radiation into the miniature waveguide. The design is such that radial resolution (~ 1 mm) is purchased at the expense of axial resolution (~ 1 cm). On the other hand, we also will report measurements of the total power output of the FEL, in which case the waveguide probe is removed from the pipe and the detector is placed downstream well beyond the vacuum window of the FEL. The FEL does not oscillate because of the polyethylene plug and the absence of a high reflectivity surface at the end of the FEL. The position of the plug can be varied along the axis of the undulator. The experiment uses a constant magnetic field (1 T) for guiding and focussing of the electron beam; this magnetic field has almost no effect on the FEL other than to enhance the quiver motion of the electrons that is driven by the helical undulator “pump” field. The undulator is designed with an adiabatic entry and exit zone of a slowly varying pump field B_1 . The “effective” pump strength parameter is defined as $a_w = |\gamma v_1/c|$, where v_1 is the actual electron quiver velocity due to the undulator.

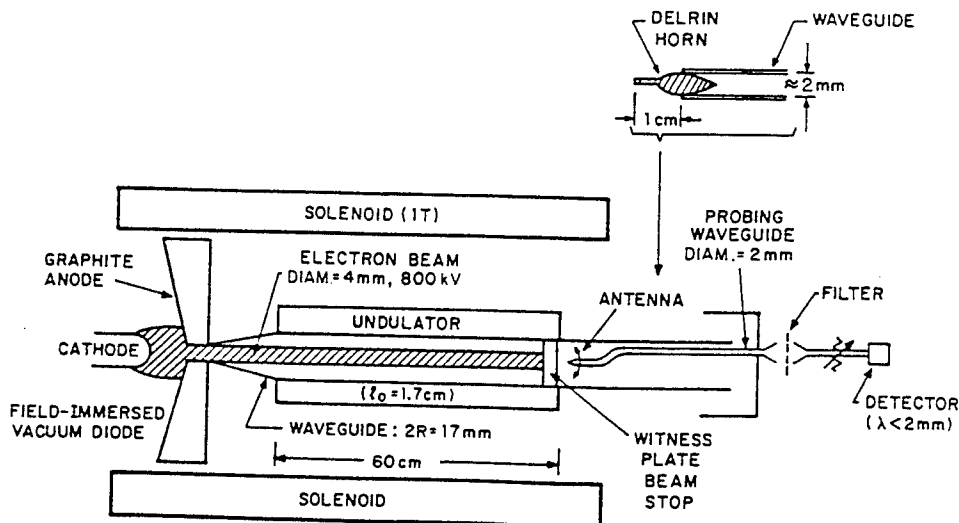


FIG. 1. Schematic of the experimental apparatus.

III. FORMULATION OF NONLINEAR EQUATIONS IN A WAVEGUIDE

The linear regime and the dispersion equation for a FEL in a waveguide has been studied exhaustively by numerous authors.^{25,26} Our goal here is to develop a set of nonlinear equations for an overmoded waveguide which can be used to follow the time-evolution of the electrons and the radiation field from noise to saturation. From Maxwell's equations,

$$\nabla \times \mathbf{E} = -\frac{1}{c} \frac{\partial \mathbf{B}}{\partial t}, \quad (1)$$

$$\nabla \times \mathbf{B} = \frac{4\pi}{c} \mathbf{J} + \frac{1}{c} \frac{\partial \mathbf{E}}{\partial t}, \quad (2)$$

$$\nabla \cdot \mathbf{E} = 4\pi \rho, \quad (3)$$

$$\nabla \cdot \mathbf{B} = 0, \quad (4)$$

where \mathbf{E} is the electric field, \mathbf{B} the magnetic field, ρ the charge density, and \mathbf{J} the current density, we get the wave equations,

$$\nabla^2 \mathbf{E} - \frac{1}{c^2} \frac{\partial^2 \mathbf{E}}{\partial t^2} = 4\pi \nabla \rho + \frac{4\pi}{c^2} \frac{\partial \mathbf{J}}{\partial t}, \quad (5)$$

$$\nabla^2 \mathbf{B} - \frac{1}{c^2} \frac{\partial^2 \mathbf{B}}{\partial t^2} = -\frac{4\pi}{c} \nabla \times \mathbf{J}. \quad (6)$$

For a cylindrical waveguide with its axis in the z direction which is also the direction of wave propagation, it is sufficient to determine E_z and B_z from which the other components of \mathbf{E} and \mathbf{B} can be calculated. We therefore consider the z components of Eqs. (5) and (6), given by

$$\left[\nabla^2 - \frac{1}{c^2} \frac{\partial^2}{\partial t^2} \right] E_z = \frac{4\pi}{c} \nabla_{\perp} \cdot \mathbf{J}_{\perp}, \quad (7)$$

and

$$\left[\nabla^2 - \frac{1}{c^2} \frac{\partial^2}{\partial t^2} \right] B_z = -\frac{4\pi}{c} (\nabla \times \mathbf{J})_z, \quad (8)$$

where \mathbf{J}_{\perp} is the transverse current produced by electron motion. The FEL has a circularly polarized undulator, specified by a vector potential,

$$\begin{aligned} \mathbf{A}_w = & -\frac{mc^2}{e} a_w [x \cos(\int_0^z k_w(z') dz') \\ & + y \sin(\int_0^z k_w(z') dz')] , \end{aligned} \quad (9)$$

where m and $-e$ are the rest mass and charge of an electron, respectively, a_w is the normalized vector potential, and $k_w = 2\pi/\lambda_w$ is the wave number of the undulator. We take a_w and k_w to be given functions of z , neglecting transverse variations of the undulator field since the electron-beam radius is much smaller than the undulator period. The equations of motion for the electron are given by

$$\begin{aligned} \frac{d\gamma_j}{dz} = & \frac{-k_s a_w a_s}{\gamma_j} \sin \psi_j \\ & + \frac{2\omega_p^2}{k_s c^2} (\langle \cos \psi \rangle \sin \psi_j - \langle \sin \psi \rangle \cos \psi_j), \end{aligned} \quad (10)$$

$$\begin{aligned} \frac{d\psi_j}{dz} = & k_w + k_s - k_s \left[1 - \frac{1 + a_w^2 - 2a_s a_w \cos \psi_j}{\gamma_j^2} \right]^{-1/2} \\ & + \frac{\partial \phi}{\partial z}. \end{aligned} \quad (11)$$

Here z is used as the independent variable, γ_j is the relativistic mass factor of the j th electron; $\psi_j = \int_0^z (k_s + k_w) dz' - \omega t + \phi$ is the phase of the j th electron with respect to the radiation field; ϕ is the phase shift of the radiation field; $k_s = \omega/c$ is the wave number of the signal wave and ω is the frequency; a_s is the normalized vector potential for the signal wave; n_0 is the electron density, assumed to be uniform at $z=0$, and $\omega_p = (4\pi n_0 e^2/m)^{1/2}$ is the plasma frequency of the beam. The angular brackets indicate an ensemble average over all electrons.

We expand E_z and B_z in a complete set of vacuum TE and TM waveguide modes,

$$\begin{aligned} E_z = & \frac{mc^2}{e} \sum_{l,m} a_{lm}(z) J_l(\nu_{lm} r) \exp(il\theta) \\ & \times \exp[i(k_{lm} z - \omega t)], \end{aligned} \quad (12)$$

$$\begin{aligned} B_z = & -\frac{imc^2}{e} \sum_{l,m} \frac{k_{lm}}{k_s} c_{lm}(z) J_l(K_{lm} r) \exp(il\theta) \\ & \times \exp[i(k_{lm} z - \omega t)], \end{aligned} \quad (13)$$

where J_l is the Bessel function of order l and k_{lm} , K_{lm} , q_{lm} and ν_{lm} are determined by the boundary conditions $(d/dr)[J_l(K_{lm} r)]|_{r=R} = 0$, $J_l(\nu_{lm} R) = 0$. Here R is the radius of the waveguide, and $K_{lm}^2 + k_{lm}^2 = \nu_{lm}^2 + q_{lm}^2 = \omega^2/c^2$. We assume that the amplitudes $a_{lm}(z)$ and $c_{lm}(z)$ are slowly varying functions of z and neglect terms containing their second derivatives. From Eqs. (7) and (8), we get

$$\begin{aligned} \sum_{l,m} 2iq_{lm} \frac{da_{lm}}{dz} J_l(\nu_{lm} r) \exp[i(l\theta + q_{lm} z)] \\ = \frac{\omega_p^2 a_w}{c^2} \exp[i(\theta + k_s z)] \left[\frac{\partial}{\partial r} A - A \delta(r - r_b) \right], \end{aligned} \quad (14)$$

and

$$\begin{aligned} \sum_{l,m} 2i \frac{k_{lm}}{k_s} \frac{dc_{lm}}{dz} J_l(K_{lm} r) \exp[i(l\theta + k_{lm} z)] \\ = \frac{\omega_p^2 a_w}{c^2} \exp[i(\theta + k_s z)] \left[\frac{\partial}{\partial r} A - A \delta(r - r_b) \right], \end{aligned} \quad (15)$$

where r_b is the radius of the electron beam and $A = \langle \exp[-i(\psi_j - \phi)] / \gamma_j \rangle$. We now assume that the quantity A is independent θ and neglect any poloidal

asymmetry of the beam, which implies that the only surviving terms in Eq. (14) and (15) are those with $l=1$. We let $a_{lm}(z)=a_m(z)\delta_{l,1}$ and $c_{lm}(z)=c_m(z)\delta_{l,1}$ and drop all subscripts l . We finally obtain

$$\frac{da_m}{dz} = \frac{ia_w\omega_p^2}{c^2} \frac{v_m}{q_m} \frac{\exp[i(k_s - q_m)z]}{R^2 J_1'^2(v_m R)} \int_0^{r_b} dr r J_0(v_m r) A, \quad (16)$$

and

$$\begin{aligned} \frac{dc_m}{dz} &= \frac{ia_w\omega_p^2}{c^2} \frac{k_s K_m}{k_m^2} \frac{\exp[i(k_s - k_m)z]}{(R^2 - K_m^2) J_1^2(K_m R)} \\ &\times \int_0^{r_b} dr r J_0(K_m R) A. \end{aligned} \quad (17)$$

The final step required to complete the FEL equations is to relate the quantities a_s and ϕ in Eq. (10) and (11) with the waveguide modes. This is done by using the relations $\mathbf{B} = \nabla \times \mathbf{A}$ and $\mathbf{E} = -(1/c)(\partial \mathbf{A}/\partial t)$. The vector potential associated with the signal is taken in the left-circularly-polarized form,

$$\begin{aligned} \mathbf{A}_s &= \frac{mc^2}{e} a_s(r, t) [\hat{x} \cos(k_s z - \omega t + \phi) \\ &\quad - \hat{y} \sin(k_s z - \omega t + \phi)]. \end{aligned} \quad (18)$$

We then find that

$$\begin{aligned} u(r, t) &\equiv a_s e^{i\phi} \\ &= \frac{1}{2k_s} \sum_m \left[c_m \frac{k_m}{K_m} J_0(K_m r) e^{i(k_m - k_s)z} \right. \\ &\quad \left. + a_m \frac{q_m}{v_m} J_0(v_m r) e^{i(q_m - k_s)z} \right]. \end{aligned} \quad (19)$$

Equations (10), (11), (16), (17), and (19), which comprise a complete set, are integrated numerically to describe two-dimensional (2D) dynamics in a waveguide, both in the exponential gain regime and at saturation. As stated in Sec. II, the experiment uses a constant axial field for guiding and focusing the electron beam, which has almost no effect on the FEL other than to enhance the quiver motion of the electrons that is driven by the helical undulator field. This motion is included in the numerical calculation of the quiver velocity $(v_1/c)_{\text{rms}}$ in the undulator.

The results of the numerical simulation will be presented with the experimental results in Sec. IV. In the next section, we describe an analytical eigenmode calculation, which is valid in the exponential gain regime and provides an independent benchmark for the numerical simulation.

IV. LINEAR EIGENMODE ANALYSIS

The transverse profile of the electromagnetic wave propagating self-similarly in a FEL can be obtained by a linear analysis of the cold-fluid equations for electrons coupled with the self-consistent Maxwell's equations. In this analysis, it is possible to solve for the actual eigen-

modes (and eigenvalues) of the system without the use of vacuum modes or of other systems of orthogonal functions. The analysis clarifies the roles of the FEL interaction and boundary conditions in the coupling of TE and TM sets of modes, and provides an independent check for the predictions of the 2D computer code. The details of the formalism, with and without a waveguide, are described elsewhere.²³ Here we briefly review the analysis in the presence of a waveguide. The starting point of the analysis is the cold-fluid equations for the electrons, given by the continuity equation,

$$\frac{1}{c} \frac{\partial}{\partial t} (h\gamma) + \nabla \cdot (h\mathbf{P}) = 0, \quad (20)$$

and the momentum equation,

$$\frac{\gamma}{c} \frac{\partial \mathbf{P}}{\partial t} + \mathbf{P} \cdot \nabla \mathbf{P} = -(\gamma \mathbf{E}' + \mathbf{P} \times \mathbf{B}'); \quad (21)$$

here $\mathbf{P} \equiv \gamma \mathbf{v}/c$, \mathbf{v} is the electron velocity, $\mathbf{E}' = (e/mc^2)\mathbf{E}$, $\mathbf{B}' = (e/mc^2)\mathbf{B}$, $\gamma^2 = 1 + \mathbf{P} \cdot \mathbf{P}$, and $h \equiv \omega_p^2/c^2 \gamma$ is the normalized fluid density. For simplicity, we consider an untapered helical wiggler with the magnetic field,

$$\mathbf{B}_w = B_w (\hat{r} \cos \Phi - \hat{\theta} \sin \Phi), \quad (22)$$

where (r, θ, z) represents the standard cylindrical coordinate system, and $\Phi = \theta - k_w z$. We assume that the beam is thin, i.e., $k_w r_b \ll 1$, and that the equilibrium flow is given by

$$\mathbf{P} = -a_w (\hat{r} \cos \Phi - \hat{\theta} \sin \Phi) + (\gamma^2 - 1 - a_w^2)^{1/2} \hat{z}. \quad (23)$$

We linearize Eqs. (20) and (21), assuming the $P_\perp \ll P_z$, and that the perturbed quantities vary much more rapidly along the axis than along the transverse directions. Any perturbed quantity δg is represented as

$$\delta g(r, \Phi, z, t) = \sum_{n=-\infty}^{+\infty} \delta g^{(n)}(r) \exp[i(n\Phi + qz - \omega t)], \quad (24)$$

where

$$\frac{\partial}{\partial z} = \frac{\partial}{\partial z} - k_w \frac{\partial}{\partial \Phi}, \quad (25a)$$

$$\frac{\partial}{\partial \theta} = \frac{\partial}{\partial \Phi}, \quad (25b)$$

and we define

$$k_z = q - lk_w. \quad (25c)$$

We now limit ourselves to the case in which one helical harmonic, say $n=l$, is dominant. In this case $\delta \mathbf{E}_1^{(l)}$ and $\delta \mathbf{B}_1^{(l)}$ are dominant, and are coupled to $\delta h^{(l-1)}$, $\delta P_z^{(l-1)}$, and $\delta E_z^{(l-1)}$. The continuity equation for $\delta h^{(l-1)}$ becomes

$$\begin{aligned} [-\gamma\omega/c + (k_z + k_w)P_z] \delta h^{(l-1)} \\ \simeq h[P_z\omega/(\gamma c) - (k_z + k_w)] \delta P_z^{(l-1)}. \end{aligned} \quad (26)$$

The momentum equation for $\delta P_z^{(l-1)}$ becomes

$$i[-\gamma\omega/c + (k_z + k_w)P_z]\delta P_z^{(l-1)} = -\gamma\delta E_z^{(l-1)} + (ck_z/\omega)a_w\delta E_+^{(l)}, \quad (27)$$

where

$$\delta E'_\pm \equiv \frac{\delta E'_r \mp i\delta E'_\theta}{2}. \quad (28)$$

We now turn to Maxwell's equations (1)–(4) in which

$$\rho' \equiv 4\pi\rho = -h\gamma \quad (29)$$

and

$$\mathbf{J}' \equiv \frac{4\pi}{c}\mathbf{J} = -h\mathbf{P}. \quad (30)$$

After linearization, Eq. (3) gives

$$i(k_z + k_w)\delta E_z^{(l-1)} = -\gamma\delta h^{(l-1)} - \frac{hP_z}{\gamma}\delta P_z^{(l-1)}. \quad (31)$$

Equations (26), (27), and (31) are algebraic equations for $\delta h^{(l-1)}$, $\delta P_z^{(l-1)}$, and $\delta E_z^{(l-1)}$. The l th harmonic of the perturbed transverse current is obtained from the relation

$$i\delta J_r^{(l)} = \delta J_\theta^{(l)} \approx -Q\delta E_+^{(l)}. \quad (32)$$

where

$$Q \equiv \frac{ha_w^2(k_z + k_w - \omega P_z/\gamma c)}{2\{[(k_z + k_w)P_z - \gamma\omega/c]^2 - h(1 + a_w^2)\}}. \quad (33)$$

Thus, the expressions for $\delta J_1^{(l)}$ are as if the system is one dimensional. The transverse dependence, however, appears in $\delta\rho^{(l)}$ and $\delta J_z^{(l)}$. From the l th harmonic of Eq. (20), and the longitudinal component of Eq. (21), it can be shown that²³

$$\delta\rho^{(l)} \approx -\frac{\gamma}{k_z P_z - \gamma\omega/c} \left[\frac{\partial}{\partial r} - \frac{l-1}{r} \right] (Q\delta E_+^{(l)}), \quad (34)$$

and

$$\delta J_z^{(l)} \approx -\frac{P_z}{k_z P_z - \gamma\omega/c} \left[\frac{\partial}{\partial r} - \frac{(l-1)}{r} \right] (Q\delta E_+^{(l)}). \quad (35)$$

From the transverse components of Eq. (5), we obtain

$$\frac{1}{r} \frac{\partial}{\partial r} \left[r \frac{\partial \delta E_+^{(l)}}{\partial r} \right] + \left[\frac{\omega^2}{c^2} - k_z^2 - \frac{(l-1)^2}{r^2} - \frac{\omega}{c} Q \right] \delta E_+^{(l)} = 0, \quad (36)$$

and

$$\frac{1}{r} \frac{\partial}{\partial r} \left[r \frac{\partial \delta E_-^{(l)}}{\partial r} \right] + \left[\frac{\omega^2}{c^2} - k_z^2 - \frac{(l+1)^2}{r^2} \right] \delta E_-^{(l)} = 0. \quad (37)$$

After further simplification, Eqs. (36) and (37) reduce to

$$\left[\frac{\partial^2}{\partial r^2} + \frac{1}{r} \frac{\partial}{\partial r} - \frac{l^2}{r^2} + \frac{\omega^2}{c^2} - k_z^2 \right] (\delta B_z^{(l)} + i\delta E_z^{(l)}) = 0 \quad (38)$$

and

$$\left[\frac{\partial^2}{\partial r^2} + \frac{1}{r} \frac{\partial}{\partial r} - \frac{l^2}{r^2} + \frac{\omega^2}{c^2} - k_z^2 - \frac{\omega}{c} Q \right] \times (\delta B_z^{(l)} - i\delta E_z^{(l)}) = 0, \quad (39)$$

which are coupled by virtue of the boundary conditions,

$$\delta E_z' = 0, \quad \frac{\partial}{\partial r} \delta B_z' = 0, \quad (40)$$

at $r=R$. In the vacuum limit $Q=0$, Eq. (38) and (39) reduce to the standard decoupled equation for $\delta B_z'$ and $\delta E_z'$ describing TE and TM modes. Using the conditions (40) and the jump conditions at $r=r_b^{23}$, we obtain the dispersion equation (for $Q \neq 0$),

$$[\pi k_1 R J_l(k_1 R) \dot{Y}_l(k_1 r_b) - 1][s \dot{J}_{l-1}(s r_b) J_{l-1}(k_1 r_b) - k_1 \dot{J}_{l-1}(k_1 r_b) J_{l-1}(s r_b)] - \pi k_1 R J_l(k_1 R) \dot{J}_l(k_1 R) [s \dot{J}_{l-1}(s r_b) Y_{l-1}(k_1 r_b) - k_1 \dot{Y}_{l-1}(k_1 r_b) J_{l-1}(s r_b)] = 0, \quad (41)$$

where the overdot in Eq. (37) denotes a derivative, and

$$k_\perp^2 \equiv \omega^2/c^2 - k_z^2, \quad (42a)$$

$$s^2 \equiv k_\perp^2 - (\omega/c)Q. \quad (42b)$$

Here ω is given approximately by the formula

$$\omega = 2k_w c \gamma^2 / (1 + a_w^2), \quad (43)$$

well-known from one-dimensional theory. Equation (41) can then be solved numerically to determine the eigenvalue.

We now compare the results of this analysis with predictions from the 2D computer code described in Sec. II. We take the electron-beam current to be 2 kA/cm², $r_b = 0.2$ cm, $R = 0.9$ cm, $\gamma = 2.5$, and $a_w = 0.3$. Equation

(41) then gives, for $l=1$ and $\omega/c = 32.9$ cm⁻¹, the eigenvalue for the most unstable mode to be $k_z = 32.8 - i0.052$ cm⁻¹. For the same set of parameters the 2D code gives $\omega/c \approx 33.0$ cm⁻¹ and a growth rate of 0.056 cm⁻¹, which is in good agreement with the imaginary part of k_z quoted earlier. It is interesting to note that if the TM modes in the 2D code are artificially "switched off" by setting $c_m = 0$, the growth rate is reduced slightly to 0.052 cm⁻¹. Thus, for typical operating parameters of the Columbia University FEL, the neglect of TM-mode coupling does not have a large effect on the growth rate of the FEL eigenmode in the exponential gain regime. The effect of TM-mode coupling is more pronounced during spatial "ring-down" which we will describe in the next section.

Figure 2(a) shows $\delta E = |\delta E|$ (with arbitrary normaliza-

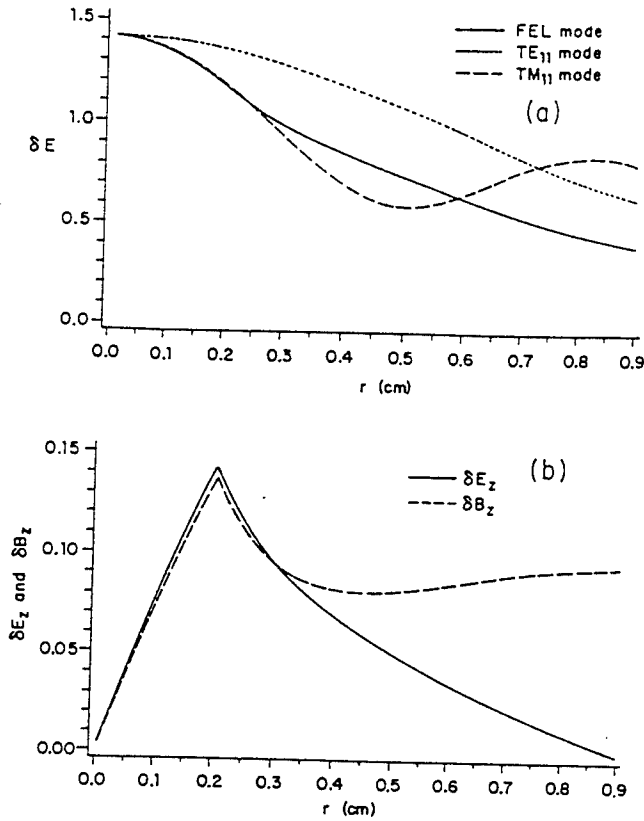


FIG. 2. (a) δE of the FEL eigenmode is compared with δE for the TE_{11} and TM_{11} vacuum modes. The FEL mode has a mixed character. (b) $|\delta E_z|$ and $|\delta B_z|$ of the FEL mode.

tion) of the FEL eigenmode as a function of r . The result of the 2D waveguide code is essentially identical with this curve. For comparison, we also show the radial profiles of δE for the TE_{11} and TM_{11} vacuum modes. Figure 2(b) shows the longitudinal wave components δE_z and δB_z of the FEL mode. We note that they are of comparable magnitude, signifying the mixed character of the eigenmode.

V. EXPERIMENTAL RESULTS AND COMPARISON WITH NUMERICAL SIMULATION

A. Linear regime of exponential growth

The experiment is first operated in the regime of exponential growth. Given the noise level of the input and the length of the undulator, we find that the interaction remains in the linear regime over most of the undulator for $a_w \leq 0.3$. Figure 3(a) shows the wave profile that results from the numerical computation of power growth and guiding along the electron beam in the overmoded waveguide for $a_w = 0.3$, with other parameters as they are in Table I. We start the simulation with zero initial radiation field and noise generated by the random distribution of electrons in phase. The wave profile shows the expected features of exponential growth and profile narrowing (which enhances the filling factor) as the wave moves down the undulator. When the electron beam is ter-

minated by the polyethylene beam stop, the optically guided power is released from the beam and radiates in the empty drift-tube waveguide, which contains the probe. The FEL eigenmode breaks up into many vacuum eigenmodes that display a characteristic spatial interference ("ring-down"). Our experiment measures the spatial profile of the ring-down. The computed ring-down (viewed from a downstream point) is shown in Fig. 3(b).

The measurements previously reported²¹ are now presented in Fig. 4, together with the prediction of theory (indicated by solid lines). The plots from theory now contain the TM as well as the TE set of modes, whereas in Ref. 21 only TE modes were retained. The computed distribution of power taken at $r=0$ along the axis [Fig. 4(a)] shows major differences with respect to the result presented earlier [Fig. 4(a), Ref. 21], yet the fit of the data to theory is neither better nor worse than the earlier fit. Perhaps this can be anticipated in a highly overmoded system such as ours, in which the "sloshing" characteristic of the interference pattern can be reproduced approxi-

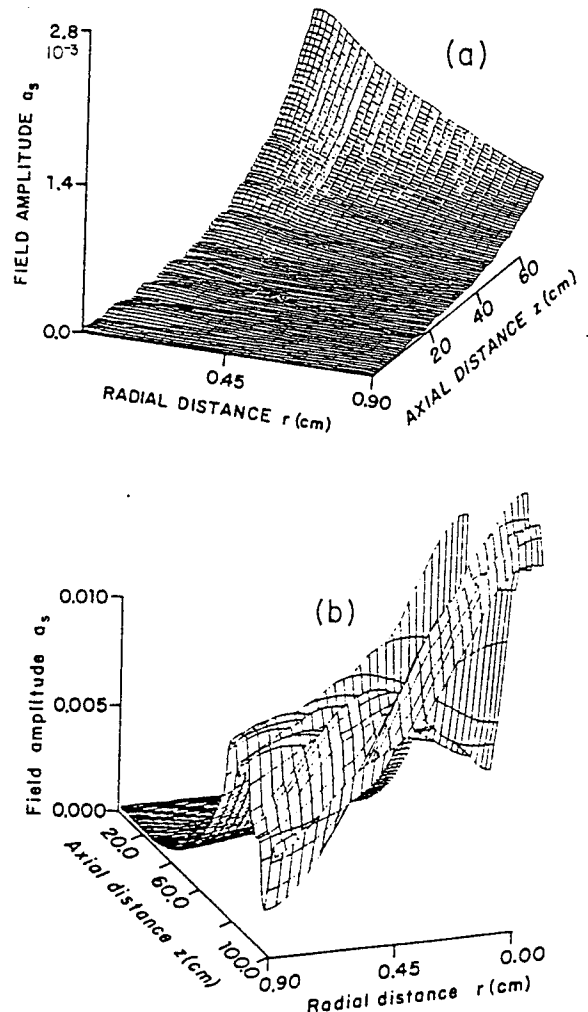


FIG. 3. (a) Wave profile in the exponential gain regime for $a_w = 0.3$, with other parameters given in Table I. (b) Computed ring-down pattern for the parameters of (a) when the electron beam is terminated at $z = 50$ cm.

mately even if a truncated set of modes are considered. Figures 4(b) and 4(c), taken at the axial power minimum and maximum, respectively, show essentially no change in the calculated radial distribution of power when compared with the corresponding curves in Ref. 21. The numerical study shows the field profile at $z=20$ cm is nearly the same as that at $z=0$. (The experimental data are the same as in Ref. 21.) By moving the beam stop and repeating the measurements, we have verified that the profile remains self-similar. The data for the radial

profile [Figs. 4(b) and 4(c)] display the features expected from theory.

The theory predicts that optical guiding is weak for $a_w \leq 0.2$. It is interesting to compare Fig. 4(a), obtained by taking $a_w=0.3$, with Fig. 5, which shows the power on axis for $a_w=0.2$. The axial variation in the latter case falls within the error bars of the data, which suggests that the "sloshing" is much less pronounced than that observed in the well-guided case.

It is useful to contrast our experiment with a similar

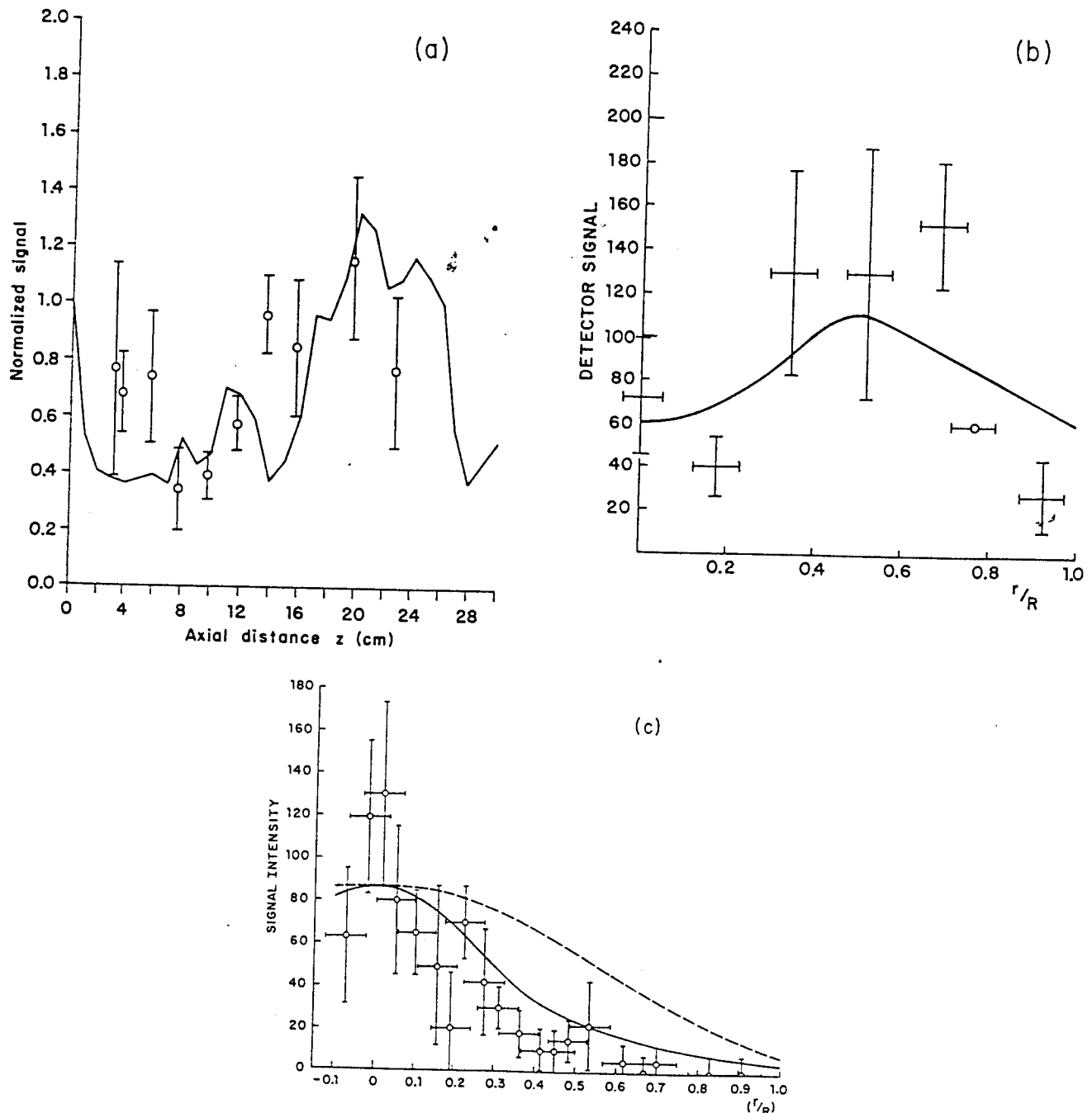


FIG. 4. (a) Experimental data (points) compared with theory (solid lines) from Fig. 3; the experimental data are the detector signal in millivolts, while the theory scale is arbitrary intensity units. This figure shows the dependence of intensity along the z axis behind the termination point ($z=50$ cm) of the electron beam. (b) Radial dependence of the intensity at $z=58$ cm. (c) Radial dependence of the intensity at $z=65$ cm. Dashed line, TE₁₁ mode only; solid line, theory curve at axial maximum.

one by Masud *et al.*^{26,27} using the same apparatus. A much smaller diameter (6.4 mm) waveguide was used; however, the wavelength, beam diameter, and current were nearly the same. One expects that optical guiding would be comparatively unimportant in this case. It was found that the observed growth rate agreed well with the theory given in Ref. 25 which predicts TE_{11} to be the only dominant mode in the linear regime. This could occur only if optical guiding were not important. We now compute the FEL eigenmode in accordance with the analysis in Sec. III for this case. To be specific, we take $r_b = 0.2$ cm, $R = 0.32$ cm, $\gamma = 2.5$, $a_w = 0.3$, and the current density to be 1 kA/cm². Equation (41) then predicts $\omega/c = 28.85$ cm⁻¹ and an amplitude growth rate ≈ 0.091 cm⁻¹ for the most unstable mode. In Fig. 6(a), we plot $|\delta B_z|$ and $|\delta E_z|$ for the FEL mode in this case for comparison with the guided case described by Fig. 2(b). Whereas $|\delta B_z|$ and $|\delta E_z|$ are comparable in Fig. 2(b), $|\delta E_z|$ is less than 10% of $|\delta B_z|$ in Fig. 6(a). Hence, the presence of TM modes is minimal in the composition of the FEL eigenmode in the small waveguide. As shown in Fig. 6(b), the FEL eigenmode is almost identical to the TE_{11} mode, and we confirm that optical guiding is indeed insignificant.

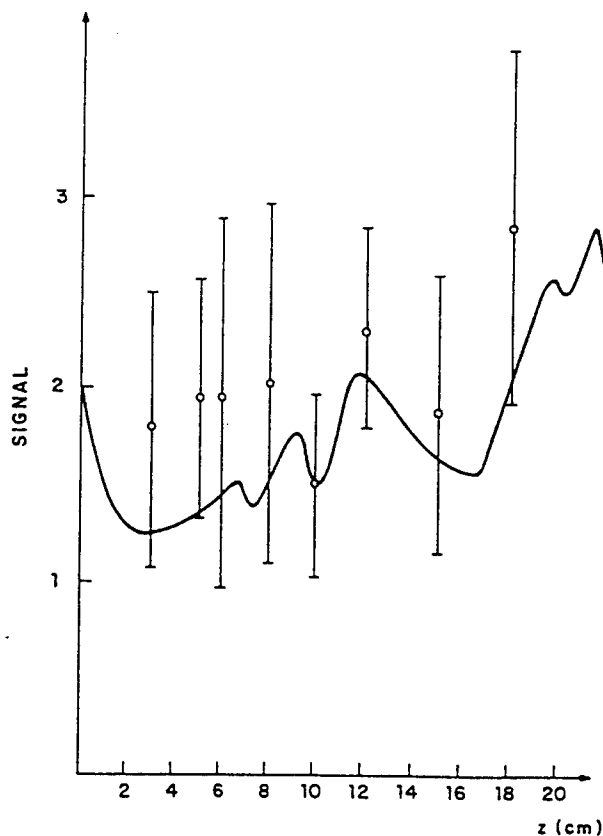


FIG. 5. Dependence of intensity along the z axis behind the termination point ($z = 50$ cm) of the electron beam for the case of weak guiding ($a_w = 0.2$). The axial variation falls within the error bars of the data, which suggests that the "sloshing" is much less pronounced than in the guided case [Fig. 4(a)].

Since refractive guiding occurs in our experiment due to the interference of many modes, we can "switch off" the guiding effect in the computer code by decoupling artificially the waveguide modes (that is, each mode is made to interact with the electrons independently). Since this "switch" is not experimentally realizable, it is necessary to validate it by actual comparison with experimental data for a weakly guided case. This has been done in the companion paper,²² and will not be repeated here. We compare in Fig. 7 the results of calculations for the dependence of the power growth rate upon the undulator field, with and without optical guiding. Without guiding, the growth rate increases linearly with the magnitude of the undulator field, as expected in the Raman limit. With guiding, the growth rate increases faster, particularly at higher pump field. The reason for this is that optical guiding improves the filling factor (f), which in turn enters the expression for the growth rate in 1D theory as $f^{1/2}$. Measurements of the growth rate, however, also indicated in Fig. 7, are not sufficiently accurate to fit unambiguously either curve. Thus, although the experimentally observed growth rate roughly validates the theory, the weak f dependence is experimentally difficult to verify. Nevertheless, the additional gain from optical guiding, when integrated over the length of the undulator, results

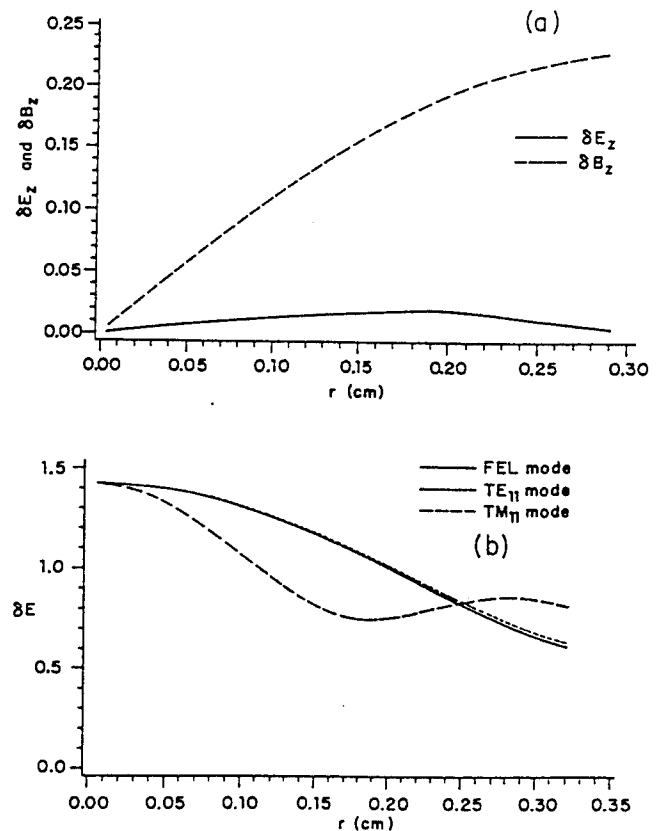


FIG. 6. (a) $|\delta E_z|$ and $|\delta B_z|$ of the FEL mode for the experiment with a smaller waveguide of radius 0.32 cm. $|\delta E_z|$ is less than 10% of $|\delta B_z|$, the FEL mode is dominantly TE_{11} , and optical guiding is insignificant. (b) δE of the FEL mode for the parameters of (a) compared with the vacuum TE_{11} and TM_{11} modes. The FEL mode is almost identical to the TE_{11} mode.

in an appreciable improvement in overall signal gain. Figure 7 shows that the most rapidly growing signal (from noise) in our experiment corresponds to the optically guided mode.

B. Saturation regime

As explained in Sec. I, refractive guiding, since it does not rely on the presence of intrinsic gain, can occur at saturation. In Ref. 22, the presence of guiding at saturation is shown to enhance somewhat the shifts of the sidebands (with respect to the carrier) as well as their growth rates, though the effect of guiding at saturation is found to be weaker than that in the exponential gain regime. Here we report on alternate experimental attempts to observe refractive guiding at saturation.

The theory predicts that when the pump field is increased to $a_w \approx 0.4$, the amplified wave will saturate approximately two-thirds of the way down the undulator. To insure saturation on all shots, we use an undulator with a slight (and unoptimized) taper (11%) beginning half way along its total length of 70 cm; the power grows by roughly a factor of 2 along this tapered region.

Typical experimental data for the spatial ring-down following a beam stop are shown in Fig. 8. In Fig. 8, we note that the axial ring-down shows a much weaker "sloshing" behavior than that in Fig. 4(a). We give here a possible explanation as to why it may be difficult to have a conclusive demonstration of refractive guiding in the presence of a waveguide. As the signal passes into saturation, some power is lost from the optically confined, guided profile and moves out to the wall; this is illustrated by a numerical solution (Fig. 9) in which the signal saturates at $z = 50$ cm. From there, it "sloshes" to and fro in the waveguide, interfering with the electron-radiation interaction occurring near the axis. The waves reflected from the wall are generally out of phase with

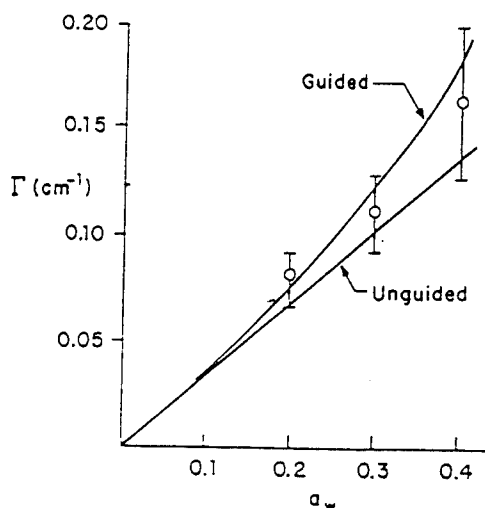


FIG. 7. Experimental data (points) of the power growth rate Γ as a function of a_w compared with theory (solid lines). The "guided" curve is calculated with modes coupled, the "unguided" curve with modes decoupled.

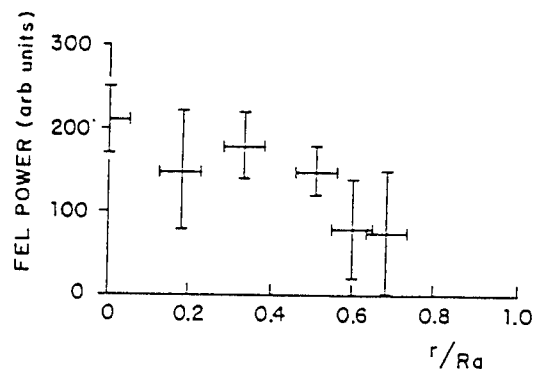
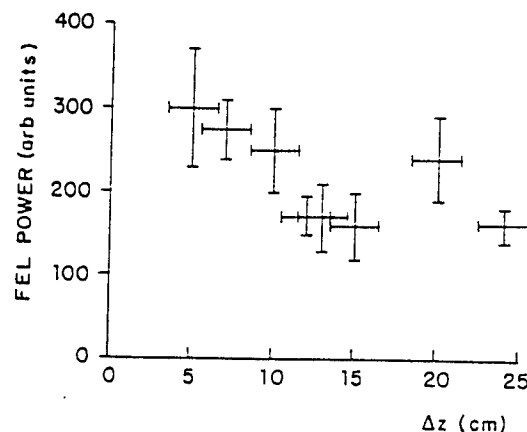


FIG. 8. Dependence of the intensity along the z axis measured from the termination point ($z = 50$ cm, $\Delta z = 0$) of the electron beam (top frame) and the radial distribution of intensity at $\Delta z = 20$ cm (bottom frame) at saturation.

respect to the ponderomotive wave, and can interfere destructively with the latter, causing a local detraping of the electrons from the ponderomotive bucket. In particular, we find that if an artificial phase shift is introduced at some point into the ponderomotive wave, an expansion of the downstream optical beam results. (Furthermore, the power released from the beam upstream also interferes

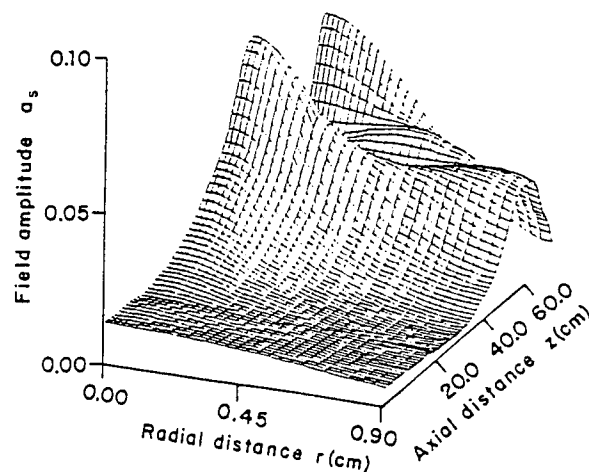


FIG. 9. Wave profile in a waveguide from start-up to saturation for $a_w = 0.3$, with other parameters given in Table I.

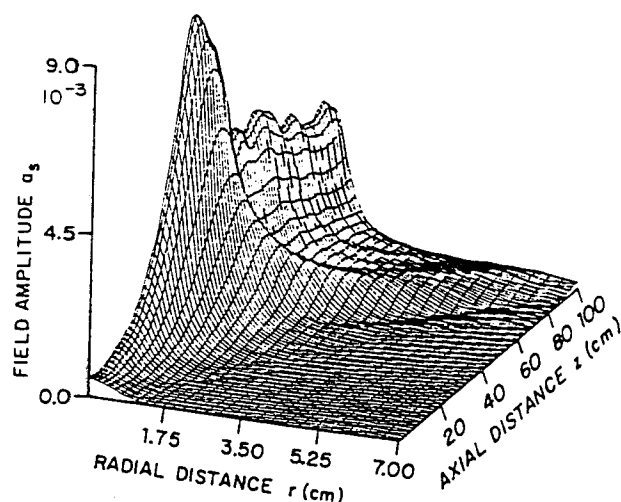


FIG. 10. Wave profile in empty space from start-up to saturation. The wave profile remains approximately self-similar at saturation.

with the radiation of the remaining guided power in the ring-down zone, resulting in a less well-defined spatial interference pattern for the experiment to detect.) On the other hand, if the experiment were done in empty space, Fig. 10 shows that though some power is lost from the beam as saturation occurs, it does not return to interfere with the FEL interaction. The profile downstream does remain approximately self-similar as it propagates, as reported by Scharlemann *et al.*⁴ using shorter wavelengths. This leads us to conclude that our failure to observe optical guiding following saturation may be an artifact of the boundary conditions imposed by the waveguide geometry, and that a short-wavelength FEL experiment operating without a waveguide may find a remnant optical guiding occurring under saturation or slow growth conditions.

VI. CONCLUSION

In this and a companion paper,²² we have attempted to validate the concept of refractive optical guiding by comparing theoretical (numerical) predictions with experimental observations in the Columbia University FEL. In the presence of a waveguide, the theory of optical guiding has certain interesting features, and we have presented in this paper two complementary methods—numerical and analytical—for the theoretical study of guiding in the exponential gain regime. We show that the two methods agree well in their predictions, and give us confidence in extending our numerical studies to the nonlinear regime.

As in Ref. 21, we believe we have presented firm, if indirect, evidence of the occurrence of optical guiding strongly influenced by refractive guiding effects in the regime of exponential gain. Refractive guiding is a subtle effect, and our approach has been to accumulate a detailed corpus of theory and experimental data, each of which adds incremental evidence in support of the concept. In the saturation regime, the experimental results presented in this paper are not conclusive, and the numerical studies suggest that the reason for this has to do with the experimental conditions, together with a weakening of the guiding effect expected from theory. (Observations of the sideband shift in the saturation regime, presented in Ref. 22, also indicate a weakening of the guiding effect.) We have given plausible arguments as to why some of the loss of guiding we observe at saturation may be attributed, somewhat paradoxically, to the presence of a waveguide. Based on these physical arguments, it is tempting to speculate that it may be possible to have a more convincing demonstration of refractive guiding in the saturation regime in a short-wavelength FEL experimental facility.

ACKNOWLEDGMENTS

This research is supported by the U. S. Office of Naval Research, Grant No. N0014-79C-0769 and the National Science Foundation, Grant No. ECS-87-13710. A. F. acknowledges the support of the Koret Foundation.

*Permanent address: Physics Department, Weizmann Institute of Science, 76100 Rehovot, Israel.

¹N. M. Kroll, P. L. Morton, and M. N. Rosenbluth, *IEEE J. Quantum Electron.* QE-17, 1436 (1981).

²P. Sprangle and C. M. Tang, *Appl. Phys. Lett.* 39, 677 (1981); *AIAA* 19, 1164 (1981).

³G. T. Moore, *Opt. Commun.* 52, 46 (1984).

⁴E. T. Scharlemann, A. M. Sessler, and J. M. Wurtele, *Phys. Rev. Lett.* 54, 1925 (1985).

⁵G. T. Moore, *Opt. Commun.* 54, 121 (1985); *Nucl. Instrum. Methods Phys. Res. A* 250, 381 (1986).

⁶M. Xie and D. A. G. Deacon, *Nucl. Instrum. Methods Phys. Res. A* 250, 426 (1985).

⁷P. Luchini, *Nucl. Instrum. Methods Phys. Res. A* 250, 413 (1985); 259, 150 (1986).

⁸K. J. Kim, *Phys. Rev. Lett.* 57, 1871 (1986).

⁹S. Y. Cai, A. Bhattacharjee, and T. C. Marshall, *IEEE J. Quantum Electron.* QE-23, 1651 (1987).

¹⁰P. Sprangle, A. Ting, and C. M. Tang, *Phys. Rev. Lett.* 59, 202 (1987); *Phys. Rev. A* 36, 2773 (1987).

¹¹S. Krinsky and L. H. Yu, *Phys. Rev. A* 35, 3406 (1987).

¹²T. M. Antonsen, Jr. and B. Levush, *Nucl. Instrum. Methods Phys. Res. A* 272, 472 (1988).

¹³A. Fruchtman, *Phys. Rev. A* 37, 2989 (1988).

¹⁴See, for instance, E. T. Scharlemann, *Proc. SPIE* 738, 129 (1987).

¹⁵J. M. Slater and D. D. Lowenthal, *J. Appl. Phys.* 52, 44 (1981).

¹⁶D. Prosnitz, A. Szoke, and V. K. Neil, *Phys. Rev. A* 24, 1436 (1981).

¹⁷R. W. Warren and B. D. McVey, *Nucl. Instrum. Methods Phys. Res. A* 259, 154 (1987).

- ¹⁸J. E. LaSala, D. A. G. Deacon, and J. M. J. Madey, Phys. Rev. Lett. 59, 2047 (1987).
- ¹⁹F. Hartemann, K. Xu, G. Bekefi, J. S. Wurtele, and J. Fajans, Phys. Rev. Lett. 59, 1177 (1987).
- ²⁰E. Jerby and A. Gover, Phys. Rev. Lett. 63, 864 (1989).
- ²¹A. Bhattacharjee, S. Y. Cai, S. P. Chang, J. W. Dodd, and T. C. Marshall, Phys. Rev. Lett. 60, 1254 (1988).
- ²²S. Y. Cai, A. Bhattacharjee, S. P. Chang, J. W. Dodd, and T. C. Marshall, Phys. Rev. A 40, 3127 (1989).
- ²³A. Fruchtman (unpublished).
- ²⁴S. C. Chen and T. C. Marshall, IEEE J. Quantum Electron. QE-21, 924 (1985).
- ²⁵H. P. Freund and A. K. Ganguly, Phys. Rev. A 28, 3438 (1983).
- ²⁶J. Masud, Ph.D. thesis, Columbia University, 1986, and references therein.
- ²⁷J. Masud, T. C. Marshall, S. P. Schlesinger, and F. G. Yee, IEEE J. Quantum Electron QE-23, 1594 (1987).

Effects of optical guiding on sideband instabilities in a free-electron laser

S. Y. Cai, A. Bhattacharjee, S. P. Chang, J. W. Dodd, and T. C. Marshall

Department of Applied Physics, Columbia University, New York, New York 10027

(Received 16 March 1989)

The effects of optical guiding on sideband instabilities in a Raman free-electron laser (FEL) are studied numerically and experimentally. An axisymmetric two-dimensional (2D) computer code that includes the effects of space charge and diffraction in an overmoded waveguide is developed to simulate sideband growth in the Columbia University FEL, which generates radiation of millimeter wavelength. It is found in both the simulation and the experiment that the effect of refractive optical guiding, which slows down the radiation group velocity, shifts the sidebands away from the signal carrier. We also find numerically that refractive optical guiding enhances the filling factor of the electron beam and perturbs the electron distribution, and thereby increases the sideband growth rate. We show that the sideband growth rate can be depressed by tuning the FEL so that the real part of the effective index of refraction associated with the electron beam decreases. The effect of wiggler tapering on the sideband growth is also studied with the 2D code. A significant reduction in the sideband growth rate in an efficiency-enhanced wiggler has been demonstrated and is qualitatively consistent with experimental measurements.

I. INTRODUCTION

Free-electron lasers (FEL's) use intense, relativistic electron beams and magnetostatic wigglers to generate tunable, high-power radiation. The power and efficiency, however, are limited by the fact that as the electrons lose energy to the radiation, the resonant condition required for the energy exchange is lost. Improved efficiency is made possible by employing the variable parameter wiggler,¹ in which the wiggler period or strength is adjusted so that the resonant condition is satisfied even after saturation. However, the growth of parasitic sideband oscillations at saturation poses a major problem for FEL performance. The sideband instabilities are caused by the Raman scattering of the signal radiation from the synchrotron oscillations executed by the electrons which are trapped in the ponderomotive potential well. The growth of sidebands leads to the detrapping of electrons from the ponderomotive buckets,² so that further energy extraction from the detrapped electrons is impossible.

In order to control the sideband growth in FEL oscillators, gratings may be used as part of the resonator to physically separate the different frequency components of the radiation field so that only the carrier reenters on the FEL axis. Other than a sophisticated optical system, this method requires a sufficiently large separation between the sidebands and the carrier in the spectrum. One of the conclusions of the present paper is that optical guiding can enhance the separation between the carrier and sidebands, and thus make the task of sideband control somewhat easier.

Experiments³ have demonstrated that a slight change in the radiation group velocity can cause a shift of sideband frequencies. The sideband frequency ω_r is related to the group velocity v_g by the formula³

$$\frac{\Delta\omega}{\omega} = \left| \frac{1 - v_{\parallel}/c}{1 - v_{\parallel}/v_g} \right| \frac{N_{\text{synch}}}{N}, \quad (1)$$

where ω is the carrier frequency, v_{\parallel} the axial velocity of electrons, c the speed of light in vacuum, N_{synch} the number of synchrotron periods in the wiggler, and N the number of wiggler periods. It is clear from Eq. (1) that a slight reduction of v_g will shift sidebands away from the carrier. When $v_{\parallel} \simeq v_g$, suppression of sideband instabilities is expected.⁴

Recent studies in FEL's indicate that the presence of optical guiding^{1,5-7} can, under certain conditions, slow down the radiation group velocity. A preliminary one-dimensional (1D) calculation by Johnston *et al.*⁸ for an untapered FEL amplifier operating in the exponential gain regime suggests that the condition $v_{\parallel} \simeq v_g$ can be met in the presence of strong refractive optical guiding. However, Ref. 8 correctly emphasizes that the analytical results in the exponential gain regime are not strictly valid at saturation where sideband growth is significant. One of the conclusions of our numerical and experimental studies in an untapered FEL is that space-charge and saturation effects weaken significantly the beneficial effects of optical guiding on sidebands anticipated by linear theory. In fact, the condition $v_{\parallel} \simeq v_g$ is not satisfied in normal regimes for FEL experiments except in the strong-diffraction limit. A preliminary report of these studies has been presented recently,⁹ and is qualitatively consistent with an independent analytical study by Antonsen and Laval.¹⁰

As stated earlier in this paper, the control of sideband instabilities in tapered FEL oscillators is a subject of considerable theoretical and experimental interest.¹¹ We have carried out numerical simulations and experiments in the millimeter-wavelength Raman FEL at Columbia

University, which uses an overmoded waveguide, and a simple, linearly tapered undulator. The experimental results, which show a reduction of sideband growth in a tapered FEL oscillator, are corroborated by the numerical simulations. Furthermore, our simulations indicate that the electron distribution is sensitive to the presence of optical guiding. Hence, quantitative analytical estimates of sideband growth which use simple models for the electron distribution, are likely to be inaccurate.

We now give a plan of the paper. In Sec. II we describe the dynamical equations used and the computational model. In Sec. III, we describe the results of numerical simulations and, where applicable, compare them with the results of recent studies. In Sec. IV we report spectroscopic studies of the sideband spectra in the Raman FEL in the presence of optical guiding, and we conclude with a summary in Sec. V.

II. DYNAMICAL EQUATIONS AND COMPUTATIONAL MODEL

A very effective method frequently employed in FEL studies is numerical simulation. Recent numerical studies of FEL sidebands have mainly taken two approaches. One method¹² solves the FEL equations in a "window" that travels down the wiggler with the speed of light and assumes that electrons slip to the back of the window; in the other method,¹³ one solves the time- and space-dependent FEL equations and treats the sidebands as the time modulation on the radiation amplitude. The former model is computationally efficient but the treatment of slippage is somewhat artificial, especially when the group velocity of the radiation is not predetermined. Therefore, we will follow the latter method of simulation.

We consider a Raman FEL having a circularly polarized undulator, specified by a vector potential in a coordinate system in which the \hat{z} axis lies along the axis of the undulator,

$$\mathbf{A}_w = -\frac{mc^2}{e} a_w \left[\hat{x} \cos \left[\int_0^z k_w dz' \right] + \hat{y} \sin \left[\int_0^z k_w dz' \right] \right], \quad (2)$$

where m and $-e$ are the rest mass and charge of an electron, respectively, a_w is the normalized vector potential, and $k_w = 2\pi/\lambda_w$ is the wave number of the undulator. Here we have assumed that k_w and a_w can be functions of z and the electron beam radius is taken to be much smaller compared with the undulator period so that the transverse variation of the undulator field can be neglected. The electron motion in such an undulator in the presence of signal radiation is governed by the equations

$$\begin{aligned} \frac{d\gamma_j}{dz} &= -\frac{k_s a_w a_s}{\gamma_j} \sin \Psi_j \\ &+ \frac{2\omega_p^2}{k_s c^2} (\langle \cos \Psi \rangle \sin \Psi_j - \langle \sin \Psi \rangle \cos \Psi_j), \end{aligned} \quad (3)$$

$$\begin{aligned} \frac{d\Psi_j}{dz} &= k_w + k_s - k_s \left/ \left[1 - \frac{1 + a_w^2 - 2a_s a_w \cos \Psi_j}{\gamma_j^2} \right] \right|^{1/2} \\ &+ \frac{\partial \phi}{\partial z}. \end{aligned} \quad (4)$$

Here z has been used as the independent variable, γ_j is the j th electron's relativistic mass factor, $\Psi_j = \int_0^z (k_s + k_w) dz' - \omega t_j + \phi(\mathbf{r}, t_j)$ is the j th electron's phase with respect to the signal wave, t_j is the time this electron reaches z , ϕ is the phase shift of the signal wave and determines refractive optical guiding, $k_s = \omega/c$ is the wave number of the signal and a_s its normalized vector potential amplitude, $\omega_p = (4\pi n e^2/m)^{1/2}$ is the plasma frequency associated with the electron beam, and the angular brackets indicate ensemble average. The second term on the right-hand side of Eq. (3) describes the effect of space charge.

The wave equation for the signal driven by the electron current can be derived from Maxwell's equations and is given by

$$\left[\nabla^2 - \frac{1}{c^2} \frac{\partial^2}{\partial t^2} \right] \mathbf{E} = \frac{4\pi}{c} \frac{\partial \mathbf{J}}{\partial t} + \frac{4\pi}{i\omega} \nabla(\nabla \cdot \mathbf{J}) \quad (5)$$

and

$$\left[\nabla^2 - \frac{1}{c^2} \frac{\partial^2}{\partial t^2} \right] \mathbf{B} = -\frac{4\pi}{c} \nabla \times \mathbf{J}, \quad (6)$$

where the transverse components of the current density can be written in terms of the electron parameters,

$$\frac{4\pi}{c} \langle \mathbf{J}_1 e^{-i(k_s z - \omega t)} \rangle = \frac{mc^2}{e} \frac{\omega_p^2 a_w}{c^2} (\hat{x} + i\hat{y}) \left\langle \frac{e^{-i(\Psi - \phi)}}{\gamma} \right\rangle. \quad (7)$$

The Columbia University FEL, which operates at millimeter wavelength, uses an overmoded waveguide to retain the radiation and yet allows optical guiding to occur.¹⁴ Accordingly, we expand Eqs. (5) and (6) in a set of vacuum TE and TM waveguide modes,

$$E_z = \frac{mc^2}{e} \left[\sum_m a_m(z, t) J_1(\nu_m r) e^{i\theta} e^{i(q_m z - \omega t)} \right], \quad (8)$$

$$B_z = -i \frac{mc^2}{e} \left[\sum_m \frac{k_m}{k_s} c_m(z, t) J_1(\kappa_m r) e^{i\theta} e^{i(k_m z - \omega t)} \right], \quad (9)$$

where J_1 is the first-order Bessel function, k_m , κ_m , q_m , and ν_m are determined by the boundary conditions

$$\left. \frac{d}{dr} J_1(\kappa_m r) \right|_{r=R} = J_1(\nu_m R) = 0$$

and

$$k_m^2 + \kappa_m^2 = q_m^2 + \nu_m^2 = \omega^2/c^2,$$

R is the radius of the waveguide, and a_m, c_m are the slowly varying mode amplitudes. For simplicity, we have assumed that the term in angular brackets on the right-hand side of Eq. (7) is independent of θ , so that only

modes with the dependence $\exp(i\theta)$ are driven by the helical current.

Substituting Eqs. (8) and (9) in Eqs. (5) and (6), respectively, and using Eq. (7) and the orthogonality property of the Bessel functions, we obtain the equations for the coefficients of the waveguide modes,

$$\left[\frac{1}{c} \frac{\partial}{\partial t} + \frac{q_m c}{\omega} \frac{\partial}{\partial z} \right] a_m = i \frac{\omega_p^2 a_w v_m \exp[i(k_s - q_m)z]}{c \omega R^2 [J_1'(v_m R)]^2} F(v_m), \quad (10)$$

$$\left[\frac{1}{c} \frac{\partial}{\partial t} + \frac{k_m c}{\omega} \frac{\partial}{\partial z} \right] c_m = i \frac{\omega_p^2 a_w k_s \kappa_m \exp[i(k_s - k_m)z]}{c^2 k_m^2 (R^2 - 1/\kappa_m^2) [J_1(\kappa_m R)]^2} \times F(\kappa_m), \quad (11)$$

where

$$F(x) \equiv \int_0^{r_b} \left\langle \frac{e^{-i(\Psi - \phi)}}{\gamma} \right\rangle J_0(xr) r dr, \quad (12)$$

and we have assumed a step distribution for the radial electron density

$$n(r) = \begin{cases} n_0, & r_b \geq r \geq 0 \\ 0, & r > r_b. \end{cases} \quad (13)$$

If the electron distribution has an explicit radial dependence, the plasma frequency ω_p in Eqs. (10) and (11) should be included in the integrand of Eq. (12). Also, the second-order derivatives of a_m and c_m in Eqs. (10) and (11) have been neglected.

The final step required to complete the FEL equations is to relate the quantity a_s and ϕ in Eqs. (3) and (4) with the waveguide modes. This is done by using the definition of vector potential, $\nabla \times \mathbf{A} = \mathbf{B}$, and $\mathbf{E} = -(1/$

$c)(\partial \mathbf{A}/\partial t)$. The vector potential associated with the signal is taken in the left-circularly polarized form (the right-circularly polarized component does not couple with the FEL but is included in the calculations of total radiation power and local signal electric field.) We take

$$\mathbf{A}_s = \frac{mc^2}{e} a_s(r, t) [\hat{x} \cos(k_s z - \omega t + \phi) - \hat{y} \sin(k_s z - \omega t + \phi)] \quad (14)$$

and find that

$$u(r, t) \equiv a_s e^{i\phi} = \frac{1}{2k_s} \sum_m \left[c_m \frac{k_m}{\kappa_m} J_0(\kappa_m r) e^{i(k_m - k_s)z} + a_m \frac{q_m}{v_m} J_0(v_m r) e^{i(q_m - k_s)z} \right]. \quad (15)$$

Then, Eqs. (3), (4), (10), (11), and (15) comprise a complete set of equations which can be solved numerically.

Before moving on to the numerical simulations, we simplify the equations further by making the variable transformations¹³

$$X \equiv a \left[t - \frac{\omega}{k_1 c^2} z \right], \quad Y \equiv a \left[\frac{z}{V} - t \right], \quad (16)$$

where

$$a \equiv c / \left[L_w \left[\frac{c}{V} - \frac{\omega}{ck_1} \right] \right],$$

L_w is the undulator length, and V is the average electron axial velocity. In terms of the new independent variables, Eqs. (3), (4), (10), and (11) take the following form:

$$\frac{\partial \gamma_j(X, Y)}{\partial X} = -L_w \frac{k_s a_s a_w}{\gamma_j} \sin \Psi_j + \frac{2\omega_p^2 L_w}{k_s c^2} (\langle \cos \Psi \rangle \sin \Psi_j - \langle \sin \Psi \rangle \cos \Psi_j), \quad (17)$$

$$\frac{\partial \Psi_j(X, Y)}{\partial X} = L_w \left[k_w + k_s - k_s / \left(1 - \frac{1 + a_w^2 - 2a_w a_s \cos \Psi_j}{\gamma_j^2} \right)^{1/2} + \frac{\partial \phi}{\partial X} \right], \quad (18)$$

$$\left[\frac{\partial}{\partial Y} + \frac{1 - q_m/k_1}{q_m c^2/\omega V - 1} \frac{\partial}{\partial X} \right] a_m = \frac{ic}{a} \frac{\omega_p^2 a_w v_m \exp[i(k_s - q_m)z]}{c \omega R^2 [J_1'(v_m R)]^2 (q_m c^2/\omega V - 1)} F(v_m), \quad (19)$$

$$\left[\frac{\partial}{\partial Y} + \frac{1 - k_m/k_1}{k_m c^2/\omega V - 1} \frac{\partial}{\partial X} \right] c_m = \frac{ic}{a} \frac{\omega_p^2 a_w k_s \kappa_m \exp[i(k_s - k_m)z]}{c^2 k_m^2 (R^2 - 1/\kappa_m^2) [J_1(\kappa_m R)]^2 (k_m c^2/\omega V - 1)} F(\kappa_m). \quad (20)$$

We note that for the TE_{11} mode for which $k_m = k_1$, the term containing the X derivative in Eq. (20) drops out. Thus, the variables chosen are such that electrons move along lines of constant Y , and the TE_{11} mode is propagated along lines of constant X . The other modes are integrated along their characteristic curves in the X - Y plane. These curves are straight lines with different slopes for different modes; hence the lines starting from the same initial point will terminate at different points at

a later time. Higher-order interpolations are thus necessary to calculate the field u if any of the characteristic lines do not fall at the grid point where u is needed for computing the electron motion. The domain of integration is indicated by the cross-hatched region in Fig. 1.

To avoid the problem of infinite time limits when solving the equations, a periodic-boundary condition is imposed in time, with the period $T = 2\pi/\Delta\omega$, where $\Delta\omega = |\omega - \omega_r|$ and ω_r is the sideband frequency. This

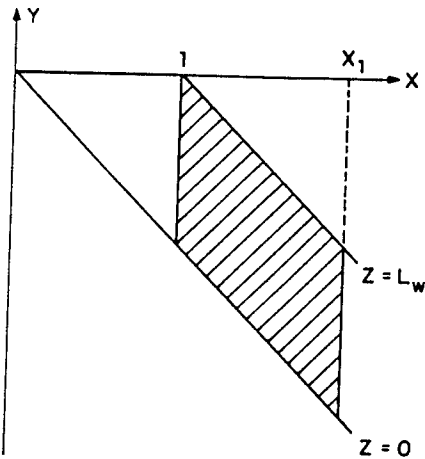


FIG. 1. Domain of integration in X and Y for Eqs. (17)–(20) indicated by the cross-hatched region. Here $X_1 = 2\pi a / \Delta\omega$.

treatment is essentially the same as that used in Ref. 12. By using this periodicity condition, however, we have only taken into account the discrete frequency components $\omega \pm k\Delta\omega$, where k is an integer, and the price for the economy in computer time is the loss of information of the other frequency components.

III. SIMULATION RESULTS

We first use our 1D code, which is described in our earlier paper,⁹ to calculate the group velocities of the signal radiation under various conditions and compare with values calculated from the 1D linear theory of Johnston *et al.*⁸ which does not include the effect of space charge. The parameters used are listed in Table I (the waveguide and transverse parameters are not used). The group velocity is computed by running two simulations with slightly different signal frequencies, ω_1 and ω_2 , around the maximum gain frequency, taking the slopes of the two ϕ - z curves and using the definition,

$$v_g = \frac{d\omega}{dk} \approx \frac{\delta\omega}{\delta\omega/c + \delta(d\phi/dz)} = \frac{c}{1 + c\delta(d\phi/dz)/\delta\omega}, \quad (21)$$

where $\delta\omega = \omega_1 - \omega_2$, $\delta(d\phi/dz) = (d\phi/dz)_1 - (d\phi/dz)_2$.

The calculated results are displayed in Table II. We

TABLE I. FEL Parameters.

Undulator period (helical)	1.7 cm
Undulator length	70 cm
Electron beam energy	800 kV
Electron beam current density	~ 2 kA/cm ²
Electron beam diameter	4 mm
Electron beam pulse length	150 nsec (20 passes)
Waveguide (drift tube) diameter	18 mm
Effective wiggler parameter a_w	0.2–0.4
FEL wavelength	2 mm
Synchrotron period	~ 20 cm
Power output	Several MW
Configuration	Oscillator

TABLE II. 1D group velocity calculation.

Condition	Group velocity v_g/c
Linger theory of Ref. 8	0.936
Simulation results:	
Linear regime without space charge	0.943
Linear regime with space charge	0.959
Saturated regime without space charge	0.955
Saturated regime with space charge	0.961

note that our 1D simulation result in the linear regime without the space-charge effect [that is, the second term on the right-hand side of Eq. (17) is dropped] agrees reasonably well with the analytical result of Ref. 8. But the inclusion of both space charge and saturation tend to increase the group velocity. A 2D simulation (including the waveguide and transverse parameters in Table I) gives an even larger group velocity of v_g/c , equal to 0.972. Since the space-charge and 2D effects are important, in general, and the sideband instabilities become the most prominent in the saturation regime, we conclude that the effect of optical guiding on sideband shifts is much weaker than anticipated in Ref. 8.

In our 2D simulations, we again use the parameters in Table I. The electron beam is assumed to be monoenergetic and uniformly distributed in Ψ from $-\pi$ to π . The carrier frequency and initial amplitude are chosen so that the system has the maximum gain in the linear regime and saturates at about the middle of the first pass along the undulator. The simulations show that the qualitative features of the radiation mode structure at the output does not depend sensitively on the input mode structure. In what follows, we use a TE_{11} mode as the input, and also include small TE_{11} sidebands at frequencies $\omega \pm \Delta\omega$. We remark that the inclusion of evanescent modes does not alter our results, and therefore we only include modes with real k_m and q_m in the computations.

The sideband growth rate spectrum is obtained by making a series of runs in which the sideband frequency is "tuned" by varying the time period T . In each run, the sideband amplitude is calculated by Fourier decomposition

$$a_r(r, \pm\Delta\omega) = \left| \frac{1}{T} \int_0^T dt u(r, t) e^{\pm i\Delta\omega t} \right|. \quad (22)$$

The sideband growth rate at each frequency is then obtained by averaging the sidebands over five passes.

One of the goals of this paper is to compare the structure of the sideband spectra with and without optical guiding. Since refractive guiding occurs essentially due to the interference of many modes in our experiments, we can "switch off" the guiding effect in the computer code by artificially decoupling all the waveguide modes (that is, each waveguide mode is made to interact with the electrons independently.) Experimentally, of course, this "switch" is not realizable. Hence, in order to validate our method, we compare the results of two simulations (of coupled and decoupled waveguide modes) with the pump field held fixed at the reduced value $a_w = 0.2$ for

which the guiding effect is expected to be weak. The group velocity at this low pump case is found to be almost equal to c , and the effect of optical guiding is negligible. Then, in this case, the results of simulations with coupled modes and decoupled modes should be very similar, and indeed they are, as shown in Fig. 2, which plots the sideband growth rate spectra from the 2D simulations. The solid curve corresponds to simulations with all modes coupled and the dotted curve to the simulations in which the optical guiding effect is switched off, and the two curves appear to be very close to each other. The reason that decoupling the waveguide modes in the simulations is an effective way to "switch off" optical guiding is because each waveguide mode has a different longitudinal wave number, and only the mode that satisfies the resonant condition is driven by the FEL mechanism directly; the comparable growth of the other modes, which is essential for the wave profile modification, must be due to the nonlinear coupling with that directly interactive mode via the electrons. Therefore, when the modes are decoupled, refractive optical guiding in this waveguide system will become impossible.

Figure 3 shows the sideband growth rate spectra from similar simulations with a higher pump field $a_w=0.3$. The shift in the sideband frequencies with respect to the carrier is clearly enhanced by the effect of refractive optical guiding. But what is surprising at first glance is that the sideband growth rate with optical guiding is also higher than that without optical guiding. The result also indicates that the effect of optical guiding on the sidebands is generally asymmetric—for the case presented here, the effect on the lower sideband is more pronounced than that on the upper sideband.

The qualitative features of the above results are further confirmed with simpler 1D simulations in which no waveguide is involved, waves are assumed to be plane waves, and the electron beam has infinite extent in the transverse dimensions (readers are referred to Ref. 8 for a full description of this 1D code). The results of these 1D

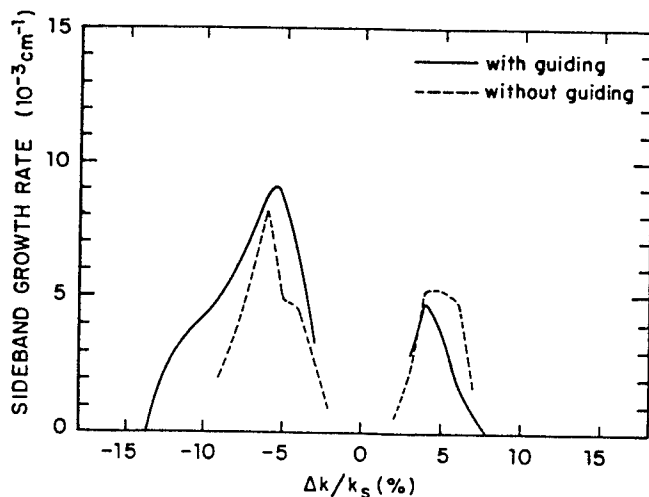


FIG. 2. Sideband growth rate spectra at saturation from 2D simulations with a low pump field of $a_w=0.2$ and a constant-period undulator.

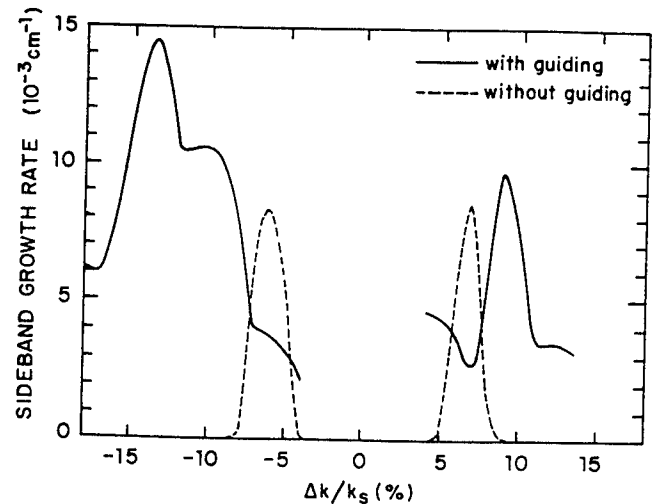


FIG. 3. Sideband growth rate spectra at saturation from 2D simulations with a higher pump field of $a_w=0.3$ and a constant-period undulator.

simulations are shown in Fig. 4. The dotted curve here is again that obtained with the optical guiding switched off. In this 1D case, the recipe for switching off the optical guiding is more straightforward, and involves replacing $\exp(-i\Psi_j)$ in Eqs. (7) and (12) by $(-i \sin \Psi_j)$. Such a replacement is equivalent to setting ϕ constant and yet conserves the total energy of the system. We note in Fig. 4 that when the refractive guiding is switched off, the upper and lower sidebands become exactly symmetric. This symmetry is entirely a mathematical artifact and can be understood through the following arguments: Since ϕ is taken to be a constant, when $\exp(-i\Psi_j)$ is replaced by $-i \sin \Psi_j$, the wave equation in the 1D limit becomes

$$\left[\frac{\partial}{\partial z} + \frac{1}{c} \frac{\partial}{\partial t} \right] a_s(z, t) = \frac{\omega_p^2 a_w}{2k_s c^2} \left\langle \frac{\sin \Psi}{\gamma} \right\rangle. \quad (23)$$

Denoting $a_s(z, t) = a_s^{(0)}(z) + a_s^{(+)}(z)e^{-i\Delta\omega t} + a_s^{(-)}(z)e^{i\Delta\omega t} + \dots$ (a sum of Fourier components), we can write Eq. (23) for the fundamental sideband amplitudes as

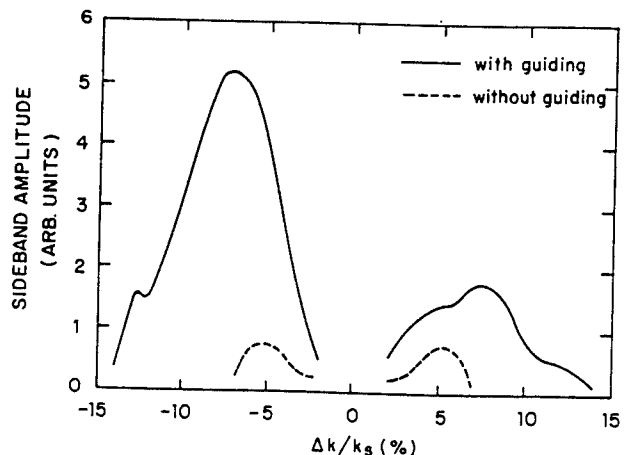


FIG. 4. Sideband amplitude spectra at saturation from 1D simulations with a constant-period undulator.

$$\frac{\partial}{\partial z} a_r^{(\pm)} \mp \frac{i\Delta\omega}{c} a_r^{(\pm)} = \frac{\omega_p^2 a_w}{2k_s c^2} \frac{1}{T} \int_0^T dt e^{\pm i\Delta\omega t} \left\langle \frac{\sin\Psi}{\gamma} \right\rangle, \quad (24)$$

the imaginary part of which is given by

$$a_r^{(\pm)} = -\frac{\omega_p^2 a_w}{4\pi k_s c} \int_0^T dt \sin(\Delta\omega t) \left\langle \frac{\sin\Psi}{\gamma} \right\rangle. \quad (25)$$

Thus, $a_r^{(+)} = a_r^{(-)}$.

The above results are also in qualitative agreement with a recent analytical theory due to Antonsen and Laval.¹⁰ In their paper, the sideband growth is calculated for different conditions of optical guiding. Inspection of their results shows that when the carrier amplitude (a_0 in their notation) is held fixed and the strength of optical guiding (described by their parameter ν) is varied, one obtains a larger sideband frequency offset and a higher sideband growth rate. A more quantitative comparison between their results and ours is difficult because our parameters do not lie in their calculated range; in any case, they assume, for analytical tractability, that the electrons are deeply trapped which is not strictly valid for our simulations.

Since sideband control is more important in FEL's with tapered wigglers, we now study the sideband growth in a tapered undulator with the 2D code. The simulations use the same parameters in Table I except now the undulator is tapered linearly in period starting at the middle of the undulator, with a rate of $d\lambda_w/dz = -0.0125$. With this tapering, the carrier power at the end of the undulator ($z = 70$ cm) is increased by approximately a factor of 2. Figure 5 plots the corresponding sideband growth rate spectrum, which shows a smaller sideband growth rate compared with that without tapering (Fig. 2). This result qualitatively agrees with the experiment of Yee, Marshall, and Schlesinger¹⁵ and recent simulations.¹⁶

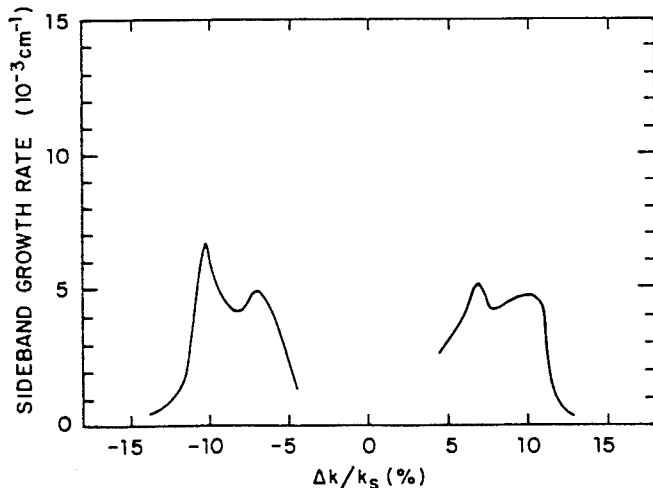


FIG. 5. Sideband growth rate spectrum at saturation from 2D simulations. The undulator is tapered with $d\lambda_w/dz = -0.0125$, starting from $z = 35$ cm.

We have seen in Fig. 3 that in an untapered FEL, while optical guiding enhanced the sideband shift, it also increases the growth rate of sidebands. In a tapered FEL, another interesting result is shown in Fig. 6, which plots the phase shift of the radiation in cases of (a) without tapering and (b) with tapering. It is evident that tapering has a somewhat deleterious effect on refractive guiding. This reduction in guiding does contribute in some small measure to the reduction in sideband growth with tapering.

It is well known that optical guiding effect increases the filling factor of the FEL optical power in the electron beam. A higher filling factor will generally give the signal radiation a higher probability to scatter from the electrons executing synchrotron oscillations and therefore the sidebands can grow faster. This is one reason why refractive optical guiding enhances the sideband growth rate. We remark here that the effect of optical guiding on the electron distribution is usually not considered in analytic treatments. It is easy to see, however, that while such treatments will correctly predict the enhanced sideband shifts due to guiding, they will not, in general, account for the differences in the growth rates of sidebands as the strength of the guiding varies. Thus, a straightforward extension of the analytical results due to Riopoulos and Tang¹⁷ in the presence of optical guiding (not included in Ref. 17) may suggest that the only required change in the theory is to reformulate their parameter δ_s , which is defined as

$$\delta_s = (\omega_r - \omega_s) - (k_r - k_s)v_{||}. \quad (26)$$

(In our notation, the subscript r denotes the sideband and s the signal carrier.) Then, instead of $\delta_s = (\omega_r - \omega_s)(1 - v_{||}/c)$ obtained in Ref. 17, one gets $\delta_s = (\omega_r - \omega_s)(1 - v_{||}/v_g)$. It may appear then that all that optical guiding does is to alter the shift $\Delta\omega$ by a multiplicative factor of $(1 - v_{||}/c)/(1 - v_{||}/v_g)$, as predicted by Eq. (1), but that the sideband growth rate would otherwise remain unchanged. This is clearly not consistent with the results

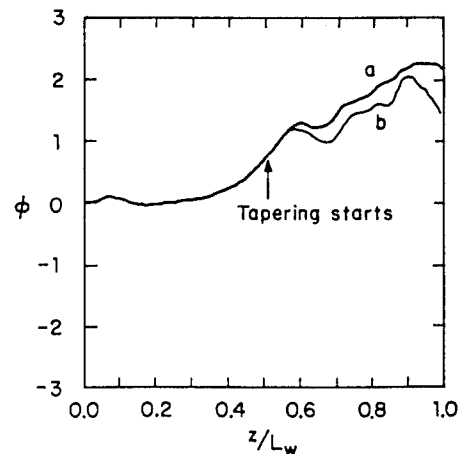


FIG. 6. The radiation phase shifts with (a) a constant-period undulator and (b) a tapered undulator. Data are taken on the axis of the system.

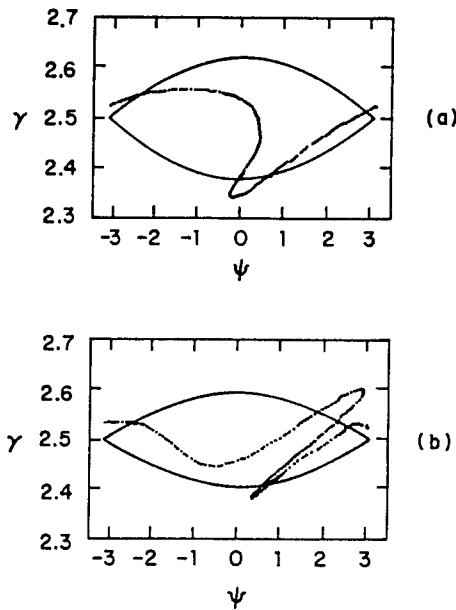


FIG. 7. Electron distributions in phase space from 2D simulations in the presence of optical guiding (a), and with optical guiding "switched off" (b). Data are taken at the beginning of saturation.

of our simulations. Hence optical guiding must affect the electron equilibrium distribution. To see this effect, we plot in Fig. 7 the electron distributions at the beginning of the saturated regime for (a) with optical guiding and (b) without optical guiding. The electron distributions shown are very different for the two cases. The effect of optical guiding on the electron distributions can be understood by examining the unperturbed Hamiltonian

$$H_0 = \frac{k_w}{\gamma_r} (\delta\gamma)^2 + \frac{\partial\phi}{\partial z} \delta\gamma - \frac{k_s a_w a_s}{\gamma_r} (\Psi \sin\Psi_r + \cos\Psi), \quad (27)$$

where $\partial\phi/\partial z$ describes refractive optical guiding and Ψ_r describes the tapering. We see that both optical guiding and tapering alter the zeroth-order Hamiltonian.

It is interesting to note, however, that the zeroth-order Hamiltonian and FEL filling factor depend only on $\partial\phi/\partial z$ which determines the effective index of refraction, and not on the group velocity of the radiation. This suggests that if we can keep the group velocity small while reducing the effective index of refraction of the electron beam, we will be able to reduce the sideband growth rate and still keep the sidebands away from the carrier. Since the linear index of refraction in the vicinity of the maximum gain point is nearly a linear function of the detuning parameter, we can actually reduce the effective index of refraction by choosing the appropriate detuning parameter while keeping the radiation group velocity, which depends only on the slope of the $\text{Re}(n)-\omega$ curve, unchanged.¹⁸ To demonstrate this effect, we perform another simulation in which the signal wave number is slightly tuned from 35.3 to 34.5 cm^{-1} . By doing this, the saturated signal power is almost unchanged and the averaged value of $\partial\phi/\partial z$ is slightly reduced. The resulting sideband growth rate spectrum plotted in Fig. 8 shows

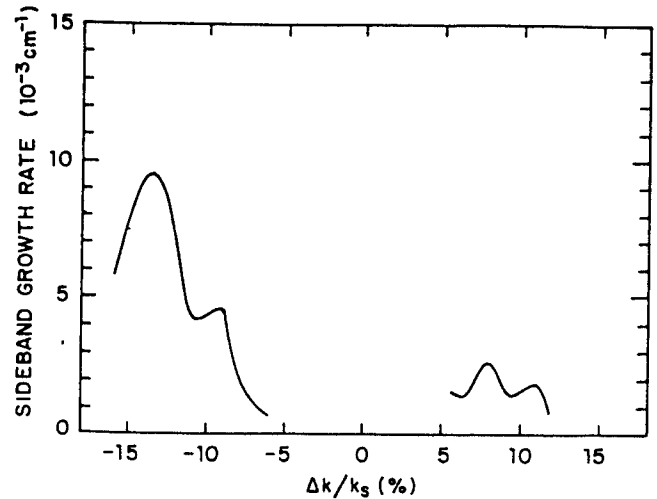


FIG. 8. Sideband growth rate spectrum in the saturated regime from 2D simulations with a constant-period undulator. The frequency of the carrier $k_s = 34.5 \text{ cm}^{-1}$ is tuned slightly away from the point of maximum linear gain.

that the sideband frequency shift is almost the same as that in Fig. 3, but the maximum sideband growth rate is substantially reduced.

IV. EXPERIMENT

Experimental studies of the effect of optical guiding on sideband instabilities are done in the Columbia University Raman FEL facility.¹⁹ As explained earlier, the artificial computational method used to switch off optical guiding described in the simulations is impossible to implement in the experiment. However, the optical guiding effect is weakened if the undulator pump field is reduced. The computer simulations in the last section show that when the pump amplitude is reduced from $a_w = 0.3$ to $a_w = 0.2$, the optical guiding effect will weaken considerably. Hence, by comparing experiments performed with these two pump amplitudes, we should be able to determine the effect of optical guiding on sideband growth. While doing this, however, precaution must be taken to ensure that measurements of the sidebands are performed at the same synchrotron frequency. Since an FEL with a different pump field will saturate at a different power level, and the synchrotron frequencies will therefore be different, our measurements are made in the nearly saturated linear regime where the signal power is still growing axially. A movable field deflector is used to deflect the electron beam to the metal drift tube at a location where the quantity $[a_w a_s / (1 + a_w^2)]^{1/2}$ remains approximately the same when a_w is changed. Data are accumulated on a shot-to-shot basis, and is then averaged after discarding shots for which the accelerator performance is not within tolerance. Refractive optical guiding is observed experimentally for $a_w = 0.3$, but when a_w is reduced to 0.2, the guiding effect cannot be detected within the limits of experimental error.¹⁴

Figure 9 shows the schematic setup of the FEL apparatus. An intense electron beam is generated with a 800-kV Marx generator and travels down a drift tube

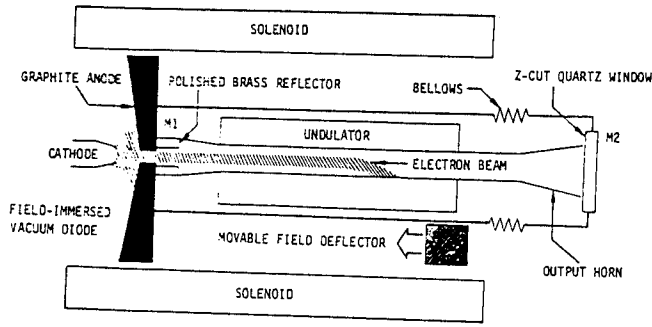


FIG. 9. The FEL oscillator. The electron beam length is varied by moving the iron field deflector. The quartz mirror is an étalon.

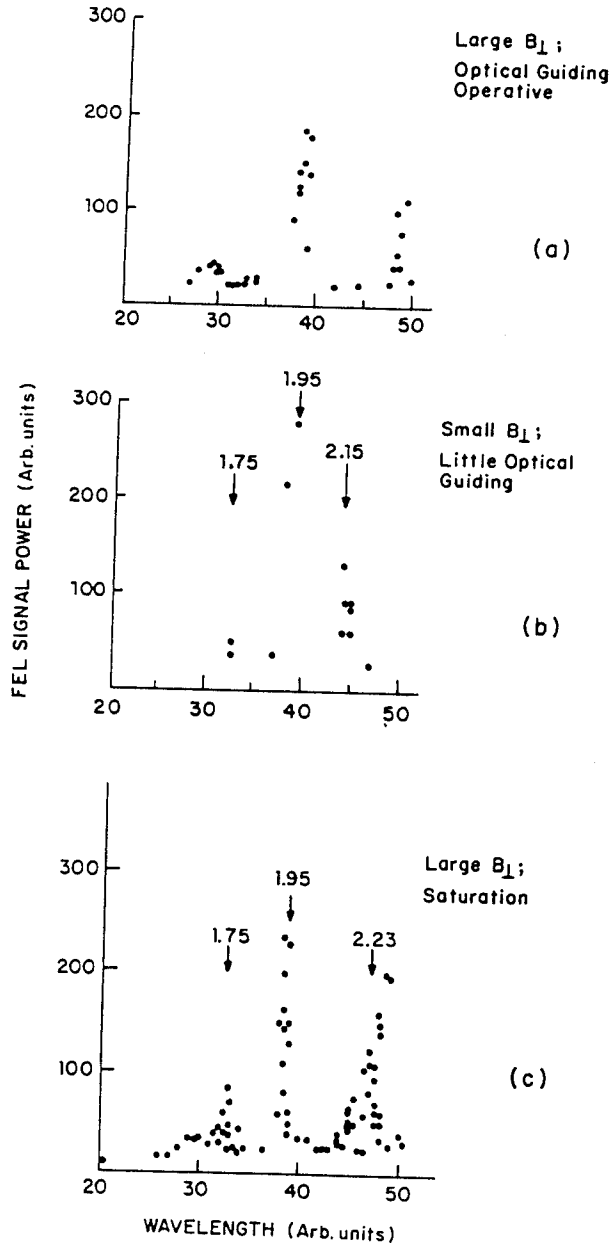


FIG. 10. Measured FEL spectra for an oscillator configuration in cases of (a) with a higher pump field and good optical guiding, (b) reduced pump field and poor optical guiding, and (c) same parameters as case (a) but the signal runs into saturation where optical guiding is weak.

which serves also as a waveguide for the radiation. The FEL is configured as an oscillator, which starts from noise, and has as an output mirror a quartz étalon. This étalon has a widely spaced distribution of resonant longitudinal modes.¹⁹ Only one such longitudinal mode falls within the unstable gain spectrum of the FEL, and the coherence of the radiation is thereby improved. A solenoid provides an axial magnetic guiding field of about 1 T for the electron beam. A correction of the effective pump field due to this guiding field is made according to the relation

$$(a_w)_{\text{eff}} = \gamma \left[\frac{v_{\parallel}}{c} \right]_{\text{rms}} \approx \frac{a_w \gamma k_w \beta c}{|\Omega_0 - \gamma k_w \beta c|}, \quad (28)$$

where $\Omega_0 = eB_0/mc$. The output signal is guided into a calibrated spectrometer (resolving power of about 100) consisting of a metal grating and a moveable detector for spectral analysis. The signal amplitude in the spectrometer can be recorded as the oscillator achieves strong output on the first radiation pass, avoiding saturation which occurs on subsequent passes.

The measured spectra are plotted in Fig. 10. An increase by a factor of 1.8 is observed in the sideband frequency offset in the larger pump-field case [Fig. 10(a)] than that in the lower pump-field case [Fig. 10(b)]. This result agrees with our simulations given in Sec. III. It is worth noting that the conditions for [Fig. 10(a)] are also those for a previously reported demonstration of optical guiding.¹⁴ Thus, the present studies provide additional evidence for guiding using spectroscopy as a nonperturbing diagnostic. The sideband growth rates in Fig. 10(a) and 10(b) are not compared because the two spectra are measured at different carrier amplitudes. Figure 10(c) is a spectrum measured well into the saturation regime with $a_w = 0.3$. In this case, the sidebands have moved back closer to the carrier compared with that in Fig. 10(a). This result, which is due to the fact that the optical guiding effect is weaker in the saturation regime than in the linear regime, is in qualitative agreement with the numerical results discussed in Sec. III. In fact, experimentally, it has not been possible to demonstrate conclusively the existence of optical guiding at saturation using the techniques described in Ref. 14.

The results above are obtained using a constant-period undulator. It is found that sideband power is appreciably reduced using a tapered undulator; for detail, the reader is referred to Ref. 15.

V. CONCLUSION

We have studied numerically and experimentally the effects of refractive guiding and wiggler tapering on the sideband instabilities. The results indicate that refractive optical guiding can shift the sideband frequencies away from the carrier. With the Columbia University FEL, a shift by a factor of about 2 in the sideband frequency offset is observed due to the presence of refractive optical guiding. Our numerical simulations also predict that in addition to the sideband frequency shift, optical guiding also enhances the sideband growth rate when the condi-

tion $v_{\parallel} \approx v_g$ is not satisfied. We believe that this increase in the sideband growth is mainly due to two reasons. First, optical guiding increases the filling factor of the beam, which in turn enhances the photon scattering from the oscillating electrons and produces more photons at the sideband frequencies. Second, the presence of optical guiding has a strong effect on the electron distribution in the ponderomotive potential wells. As predicted by analytic calculations,^{2,17} the sideband growth is very sensitive to the details of the electron distribution functions. By tuning the "detuning parameter" slightly away from the maximum gain point, we, however, are able to

demonstrate numerically a reduction in the sideband growth rate while simultaneously maintaining sideband separation from the carrier. Our results also show that undulator tapering which increases the FEL efficiency can, under certain conditions, reduce the sideband growth as well.

ACKNOWLEDGMENTS

This research is supported by the Office of Naval Research, Grant No. N0019-79C-0769 and the National Science Foundation, Grant No. ECS-87-13710.

-
- ¹N. M. Kroll, P. L. Morton, and M. N. Rosenbluth, IEEE J. Quantum Electron. QE-17, 1436 (1981); A. T. Lin and J. M. Dawson, Phys. Rev. Lett. 42, 1670 (1979); P. Sprangle, C.-M. Tang, and W. M. Manheimer, *ibid.* 43, 1932 (1979).
- ²N. M. Kroll and M. N. Rosenbluth, in *Physics and Quantum Electronics* (Addison-Wesley, Reading, MA, 1980), Vol. 7, p. 147.
- ³J. Masud, T. C. Marshall, S. P. Schlesinger, F. G. Yee, W. M. Fawley, E. T. Scharlemann, S. S. Yu, A. M. Sessler, and E. J. Sternbach, Phys. Rev. Lett. 58, 763 (1987).
- ⁴S. S. Yu, W. M. Sharp, W. M. Fawley, E. T. Scharlemann, A. M. Sessler, and E. T. Sternbach, Nucl. Instrum. Methods Phys. Res. A259, 219 (1987).
- ⁵P. Sprangle and C. M. Tang, Appl. Phys. Lett. 39, 677 (1981).
- ⁶G. T. Moore, Opt. Commun. 52, 46 (1984).
- ⁷E. T. Scharlemann, A. M. Sessler, and J. S. Wurtele, Phys. Rev. Lett. 54, 1925 (1985).
- ⁸S. Johnston, A. M. Sessler, Y.-J. Chen, W. M. Fawley, and E. T. Scharlemann (unpublished).
- ⁹A. Bhattacharjee, S. Y. Cai, S. P. Chang, J. W. Dodd, and T. C. Marshall, in Proceedings of the Tenth International Free-Electron Laser Conference, Jerusalem, 1988 [Nucl. Instrum. Methods Phys. Res. A (to be published)].
- ¹⁰T. M. Antonsen and G. Laval (unpublished).
- ¹¹For an excellent review, see D. C. Quimby, Proc. SPIE 738, 103 (1987) and references therein.
- ¹²W. B. Colson and R. A. Freedman, Opt. Commun. 46, 37 (1983).
- ¹³M. N. Rosenbluth, H. V. Wong, and B. N. Moore, Proc. SPIE 453, 25 (1984).
- ¹⁴A. Bhattacharjee, S. Y. Cai, S. P. Chang, J. W. Dodd, and T. C. Marshall, Phys. Rev. Lett. 60, 1254 (1988).
- ¹⁵F. G. Yee, T. C. Marshall, and S. P. Schlesinger, IEEE Trans. Plasma Sci. 16, 162 (1988).
- ¹⁶B. Hafizi, A. Ting, P. Sprangle, and C. M. Tang, Phys. Rev. A 38, 197 (1988).
- ¹⁷S. Riyopoulos and C. M. Tang, Phys. Fluids 31, 1708 (1988).
- ¹⁸S. Y. Cai, A. Bhattacharjee, and T. C. Marshall, IEEE J. Quantum Electron. QE-23, 1651 (1987).
- ¹⁹J. Masud, T. C. Marshall, S. P. Schlesinger, and F. G. Yee, IEEE J. Quantum Electron. QE-23, 1594 (1987).

**SIDEBAND INSTABILITIES AND OPTICAL GUIDING IN A FREE ELECTRON LASER:
EXPERIMENT AND THEORY**

A. BHATTACHARJEE, S.Y. CAI, S.P. CHANG, J.W. DODD and T.C. MARSHALL

Department of Applied Physics, Columbia University, New York, New York 10027, USA

Experimental and theoretical studies of the effects of tapering and optical guiding on sideband instabilities are reported. The experiments are performed in the Columbia Raman FEL (≈ 2 mm). Experiment shows sizeable reductions in sideband amplitudes in an efficiency-enhanced undulator. In the presence of optical guiding in a constant-period undulator, the sideband shift is larger compared with the case when optical guiding does not occur.

The sideband instability [1] in a free electron laser, driven by the synchrotron motion of the electrons trapped in the ponderomotive potential well, has been regarded as a hazard to FEL efficiency-enhancement schemes such as the variable parameter undulator [2]. The hazard is that uncontrolled growth of the sideband may detrap electrons from the ponderomotive bucket and undermine the efficiency of energy extraction. Strong sidebands have indeed been observed in experiments [3–5].

One of the purposes of the present paper is to describe recent experimental results from the Columbia FEL (≈ 2 mm) with a tapered undulator which shows that the sideband amplitude is much lower than with a comparable constant-parameter undulator [6]. Both experiment and numerical simulation indicate that this reduction in sideband amplitude can be accomplished without compromising the standard prescription for efficiency enhancement.

Another purpose of this paper is to report preliminary experimental and theoretical results of the effects of optical guiding on sidebands. The concept of optical guiding has been validated in several experiments [7–10]. Since optical guiding occurs due to modifications in the refractive index of the electron beam which in turn determines the group velocity of the radiation, it is natural to expect that optical guiding should control the slippage between the electron and optical pulses, and hence, the sideband shift.

We begin with a discussion of sideband instabilities in a tapered wiggler. The operating parameters of the Columbia Raman FEL are given in table 1, and the experimental configuration is shown in fig. 1. The experiment demonstrated enhancement in efficiency from 4% (“untapered”) to 12% (“tapered”) – details are given in ref. [6]. In fig. 2 we compare the spectra of the radiated power for the untapered and tapered undulators. Fig. 2a is the spectrum showing the carrier (2.5

mm) and the long-wavelength sideband (2.6 mm) in an untapered undulator. Fig. 2b shows the corresponding spectrum for a tapered undulator – the sideband amplitude is down by 50% compared with that in the constant-period undulator. Fig. 3 shows the power growth along the tapered section of the undulator ($l_w = 1.45$ cm for $z \leq 40$ cm). A 1-D simulation predicts an increase of power by approximately a factor of two [11]. The observations indicate that the enhancement in the efficiency of a tapered undulator is approximately in accordance with the prediction of 1-D, single-mode theory. Furthermore, tapering has the salutary effect of reducing the sideband amplitude. In these experiments, optical guiding does not occur. Numerical simulations of the Columbia FEL using a 2-D code with waveguide boundary conditions reproduce qualitative features of the sideband behavior [6]. (Similar numerical results for a short wavelength FEL have also been reported recently by Hafizi et al. [12].)

Table 1
FEL experimental parameters

Accelerator voltage	800 kV (figs. 5–7) 700 kV (figs. 2 and 3)
Electron beam current density	1 kA/cm ²
Electron beam radius	2 mm
Waveguide (drift tube) radius	9 mm (figs. 5–7) 3 mm (figs. 2 and 3)
Undulator period	1.7 cm (figs. 5–7) 1.45 cm (figs. 2 and 3)
Normalized vector potential of undulator field $\gamma v_z / c$	$a_w \sim 0.3$
FEL carrier wavelength	1.8–2.0 mm (figs. 5–7) 2.5 mm (figs. 2 and 3)
FEL power	100 kW to MWs
Resonator length	≈ 1 m

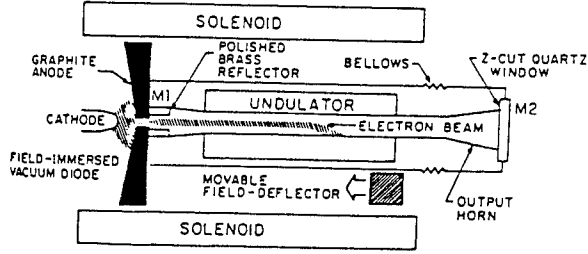


Fig. 1. The FEL oscillator. The electron beam length is varied by moving the iron-field deflector. The quartz mirror is an etalon.

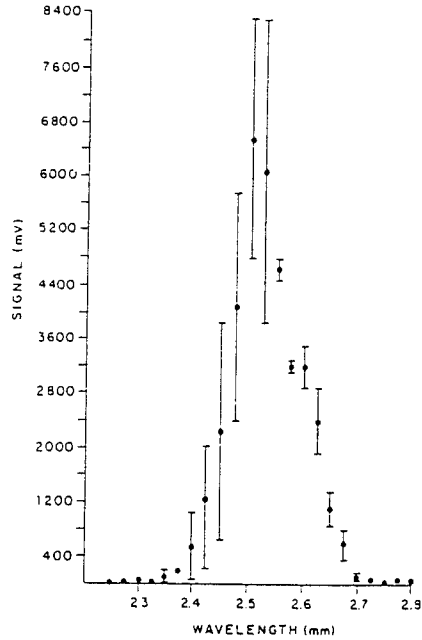
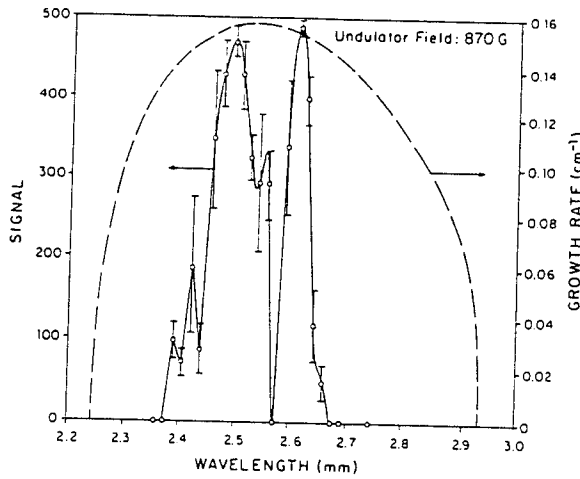


Fig. 2. Spectrum showing carrier (2.5 mm) and long-wavelength sideband (2.6 mm) emitted from an FEL in an untapered undulator (a) and a tapered undulator (b). The sideband amplitude in (b) is smaller by 50% compared with (a) [6].

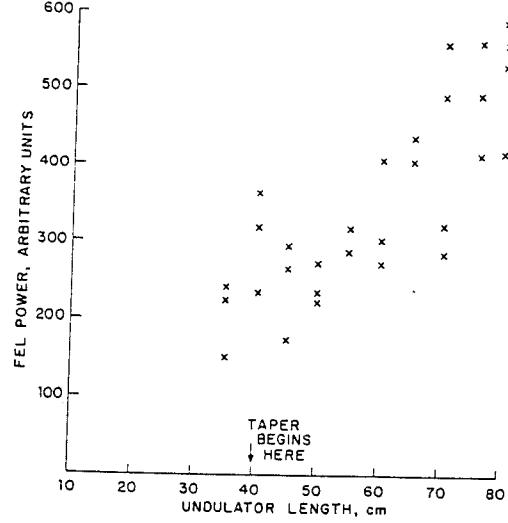


Fig. 3. Power growth along the tapered portion of the undulator.

We now describe the effect of optical guiding on sidebands. The equations of motion of the electrons are

$$\frac{d\gamma_j}{dz} = -\frac{k_s a_w a_s}{\gamma_j} \sin \psi_j + \frac{2\omega_p^2}{\omega_s c} [\langle \cos \psi \rangle \sin \psi_j - \langle \sin \psi \rangle \cos \psi_j], \quad (1)$$

$$\frac{d\psi_j}{dz} = k_w + k_s - k_s \frac{1}{\sqrt{1 - (1 + a_w^2 - 2a_w a_s \cos \psi_j)/\gamma_j^2}} + \frac{\partial \phi}{\partial z}, \quad (2)$$

where $\gamma_j mc^2$ is the energy of the j th electron of rest mass m , ψ_j is the phase of the j th electron with respect to the signal of frequency $\omega_s = k_s c$ and wave number k_s , $k_w = 2\pi/l_w$ is the wave number of the wiggler, a_w and a_s are respectively the normalized vector potentials of the helical wiggler and signal, $\omega_p^2 = 4\pi n e^2/m$ is the plasma frequency of the electron beam, and ϕ is the phase shift of the radiation field. The second term on the right-hand-side of eq. (1) describes the effect of space charge.

The 1-D wave equation for the radiation amplitude, assuming it is slowly varying, is

$$\left(\frac{\partial}{\partial z} + \frac{1}{c} \frac{\partial}{\partial t} \right) u(z, t) = \frac{i\omega_p^2 a_w}{k_s c^2} \left\langle \frac{\exp[-i(\psi - \phi)]}{\gamma} \right\rangle, \quad (3)$$

where $u = a_s \exp(i\phi)$. The calculation can be simplified

by integrating along the characteristics of eq. (3), which motivates the following variable transformations [13]:

$$\begin{aligned} x &= \frac{c}{L_w(c/v-1)}(t-z/c), \\ y &= \frac{c}{L_w(c/v-1)}(z/v-t). \end{aligned} \quad (4)$$

Here L_w is the length of the wiggler. Then eqs. (1)–(3) transform to

$$\begin{aligned} \frac{\partial \gamma_j}{\partial x} &= -\frac{L_w k_s a_s a_w}{\gamma_j} \sin \psi_j \\ &+ \frac{2L_w \omega_p^2}{\omega_s c^2} [\langle \cos \psi \rangle \sin \psi_j - \langle \sin \psi \rangle \cos \psi_j], \end{aligned} \quad (5)$$

$$\begin{aligned} \frac{\partial \psi_j}{\partial x} &= L_w \left(k_w + k_s - k_s \right. \\ &\quad \left. / \sqrt{1 - (1 + a_w^2 - 2a_w a_s \cos \psi_j) / \gamma_j^2} \right) + \frac{\partial \phi}{\partial x}, \end{aligned} \quad (6)$$

$$\frac{\partial u}{\partial y} = \frac{i L_w \omega_p^2 a_w}{k_s c^2} \left\langle \frac{\exp(-i(\psi - \phi))}{\gamma} \right\rangle. \quad (7)$$

We impose a periodic boundary condition in time. The period is taken to be $\tau = 2\pi/\Delta\omega$, where $\Delta\omega \equiv \omega_r - \omega_s$ and ω_r is the sideband frequency. Eqs. (5)–(7) are then solved in the cross-hatched domain indicated in fig. 4.

Refractive optical guiding, which occurs because the refractive index n obeys the condition $\text{Re}(n) > 1$, is of primary interest in this paper. Refractive guiding can be artificially reduced to zero in free space by replacing $\langle \exp(-i\psi)/\gamma \rangle$ with $-i\langle \sin \psi/\gamma \rangle$. In what follows, we compare the results of the 1-D simulation with and without optical guiding, and study the effects of space charge. The numerical results are compared with the well-known formula [5],

$$\frac{\Delta\omega}{\omega_s} = \frac{1 - v_{\parallel}/c}{1 - v_g/c} \frac{N_{\text{synch}}}{N}, \quad (8)$$

where v_g is the group velocity of the radiation and

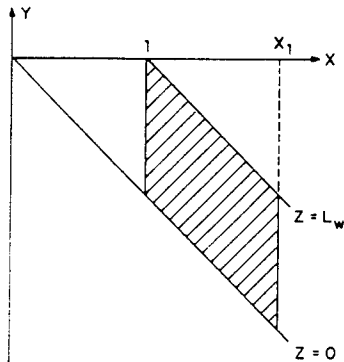


Fig. 4. Domain of integration in x and y for eqs. (5)–(7) indicated by the cross-hatched region.

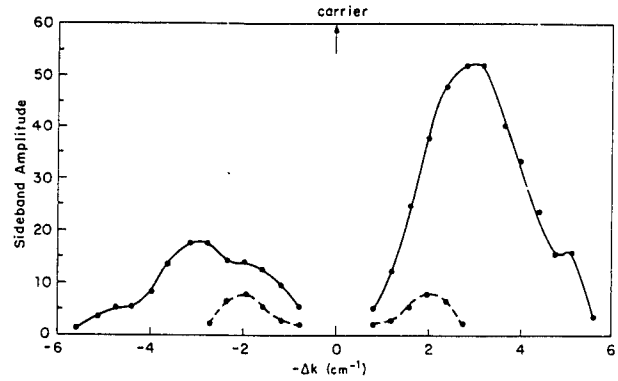


Fig. 5. Numerical simulation of sidebands with (solid lines) and without optical guiding (dotted lines).

N_{synch} is the number of periods of the synchrotron oscillations within an undulator which has N periods.

The experiment is done in a highly overmoded waveguide, where optical guiding is set up by the nonlinear coupling of higher order propagating waveguide modes via the FEL interaction [10]. Before we present experimental results, we discuss results from numerical simulations. In fig. 5 we compare the sideband shift for the parameters listed in table 1 (appropriate to the larger drift tube) with and without optical guiding, and zero space charge. The effect of guiding clearly enhances the sideband shift, but also increases the sideband amplitude. It is interesting to note that in this case the lower and upper sidebands are exactly symmetric about the carrier when guiding is turned off.

A preliminary calculation by Johnston et al. [15] in the linear regime predicts $v_g/c = 0.936$ for the parameters of fig. 5. Our numerical results without space charge in this regime is $v_g/c = 0.943$, which is in reasonable agreement with his theory. If the effect of space charge is included, we obtain $v_g/c = 0.959$ in the linear regime. In the saturation regime, we get $v_g/c = 0.955$ without space charge, and $v_g/c = 0.961$ with space charge. Formula (8) then clearly indicates that the sideband shift enhancement due to guiding is generally degraded by the effects of space charge and at saturation.

We now present sideband spectroscopy studies of the Columbia Raman FEL. The spectrum is obtained by a grating spectrometer with a resolving power ~ 100 . Data is accumulated on a shot-by-shot basis, and then is averaged after discarding shots when the accelerator performance is not within tolerance. The FEL is configured as an oscillator, the output mirror generally being a quartz etalon. This etalon has a widely-spaced distribution of longitudinal modes, unlike the FEL resonator where the cavity modes are closely spaced. The etalon mirror therefore favors oscillation on just one longitudinal mode of the combined system, and this results in improved coherence. The idea is to choose the

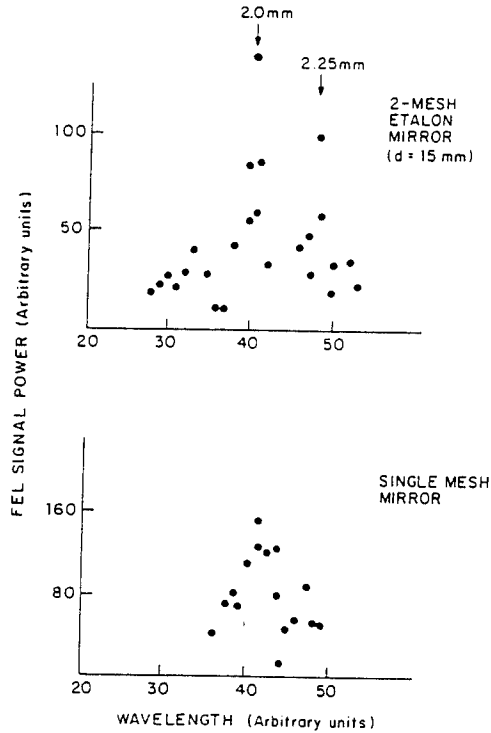


Fig. 6. FEL spectra for an oscillator configuration using a single-mesh mirror reflector (b) and a two-mesh etalon (a). The long-wavelength sideband is at 2.25 mm.

etalon spacing so that just one longitudinal mode of the etalon falls within the unstable gain-spectrum of the FEL.

A demonstration of the narrowing of the FEL "carrier" is shown in fig. 6. In fig. 6b, the output mirror is a simple wire mesh, whereas in fig. 6a the output mirror is an etalon made up of two wire meshes separated by 15 mm spacing. The spectral width of the carrier in fig. 6a is $\sim 1.5\%$, whereas in fig. 6b the carrier is much wider – at least 3% or more. A complicating feature is the sideband; the long wavelength sideband in fig. 6 is prominent. We will return to this shortly. In addition to the linewidth narrowing, the etalon can also "pull" the carrier wavelength of the FEL if the etalon spacing is appreciably changed. We have been able to change the carrier wavelength by $\sim 5\%$ using this technique.

In the sideband studies which follow, not only the magnetic field of the undulator, but also the length of the electron beam in the undulator can be changed. This can be done by using a movable piece of iron inside the guiding-field solenoid; the electron beam is deflected to the wall of the drift tube by the iron. The FEL will oscillate over a wide range of electron beam-length, the "start-time" of the oscillator increasing as the beam length is shortened. It is quite possible to operate the system so that, starting from noise, at a high value of undulator field the signal saturates before reaching the

end of the undulator. The sideband can be observed either when the FEL signal reaches a saturated condition (which is where one might naturally expect to find it), or relatively "late" in the regime of exponential growth. This occurs in this experiment because the growth rate of the sideband is comparable to the carrier. When we report data on the sideband in the linear regime of growth, we have shortened the beam length so that saturation does not occur on a single pass, and we observe the signal strength on the first pass of the radiation along the system. The experimental studies use the FEL as an oscillator with a quartz etalon mirror, and couple the output power into the spectrometer where both the carrier and sidebands are observed. (In previous optical guiding studies [10], a broadband filter was used so that the guiding signal data included carrier and sidebands.)

Three sideband spectra are shown in fig. 7. In figs. 7a and 7b we show spectra obtained near the end of the exponential growth phase, comparing a case where the undulator field is large and optical guiding is occurring

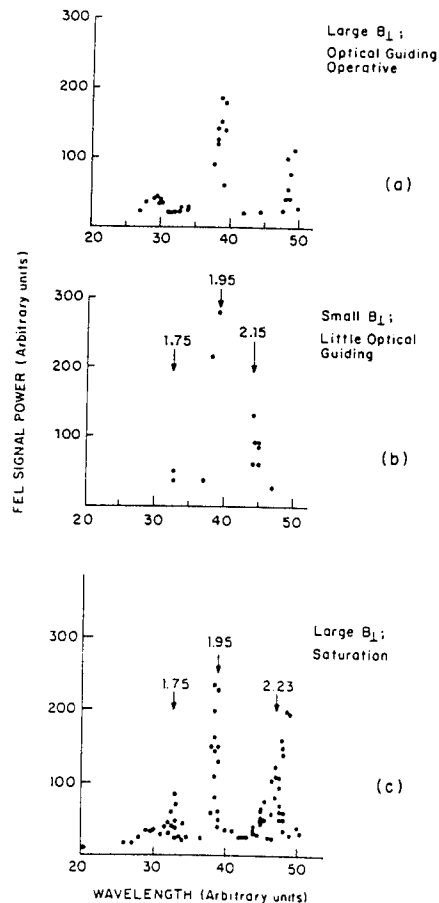


Fig. 7. Effect of optical guiding on the sideband wavelength. (a) Case of good optical guiding [10]; (b) optical guiding poor, reduced B_{\perp} ; (c) same as case (a) but the signal is run into saturation.

(this is the example of ref. [10]) with a case where the undulator field is weaker and optical guiding is marginal according to the theory and not found experimentally. Because the sideband shift depends on the synchrotron period, which itself depends on the product $(a_s a_w)^{1/2}$, we have allowed the signal in case (b) to grow to a larger amplitude than in case (a) so that we are comparing examples with nearly the same synchrotron period. This is done by reducing the length of the electron beam in the undulator for the case with larger pump field. An experimental estimate of the synchrotron period is in the range ~ 20 cm (this is obtained from a study of power variation along the electron beam following the point of saturation). The sideband shift from the carrier in fig 7b is seen to be consistent with this measurement; that is, $N_{\text{syn}}/N \sim 10\%$.

By comparing the two examples in figs. 7a and 7b, we find the optical guiding has resulted in an increase of the sideband displacement from the FEL carrier. We attribute this increase to the refractive effect of optical guiding upon the wave group velocity, as given by eq. (8). The experiment operates under conditions of refractive guiding dominating gain guiding. In fig. 7c, we show what happens to the spectrum of fig. 7a if the signal is allowed to grow well into the saturation regime. Then the sidebands have a tendency to shift closer to the carrier: the short wavelength sideband returns to the same location as fig. 7b, while the long wavelength sideband is shifted somewhere between the location of fig. 7a and fig. 7b. Again, the synchrotron period is nearly unchanged. The conclusion from fig. 7c is that as the signal goes into saturation, the additional sideband shift due to guiding is diminished. The results are in qualitative agreement with the numerical results discussed earlier.

Acknowledgement

We are grateful to Prof. S. Johnston for sharing his unpublished results with us. This research is supported

by the U.S. Office of Naval Research, Grant No. N0014-79C-0769, and the National Science Foundation, Grant No. ECS-87-13710.

Note added in proof: More details on the effects of optical guiding on sideband instabilities have been given in a recent article [16].

References

- [1] N.M. Kroll and M.N. Rosenbluth, in: *Physics and Quantum Electronics* (Addison-Wesley, Reading, MA, 1980) vol. 7, p. 147.
- [2] N.M. Kroll, P.L. Morton and M.N. Rosenbluth, in ref. [1], p. 81.
- [3] R.W. Warren, B.E. Newnam and J.C. Goldstein, *IEEE J. Quantum Electron.* 21 (1985) 882.
- [4] F.G. Yee, J. Masud, T.C. Marshall and S.P. Schlesinger, *Nucl. Instr. and Meth.* A259 (1987) 104.
- [5] J. Masud, T.C. Marshall, S.P. Schlesinger, F.G. Yee, W.M. Fawley, E.T. Scharlemann, S.S. Yu, A.M. Sessler and E.J. Sternbach, *Phys. Rev. Lett.* 58 (1987) 763.
- [6] F.G. Yee, T.C. Marshall and S.P. Schlesinger, *IEEE Trans. Plasma Sci.* 16 (1988) 162.
- [7] F. Hartemann, K. Xu, G. Bekefi, J.S. Wurtele and J. Fajans, *Phys. Rev. Lett.* 59 (1987) 1177.
- [8] R.W. Warren and B.D. McVey, *Nucl. Instr. and Meth.* A259 (1987) 154.
- [9] J.E. LeSala, D.A.G. Deacon and J.M.J. Madey, *Phys. Rev. Lett.* 59 (1987) 2047.
- [10] A. Bhattacharjee, S.Y. Cai, S.P. Chang, J.W. Dodd and T.C. Marshall, *Phys. Rev. Lett.* 60 (1988) 1254.
- [11] F.G. Yee and T.C. Marshall, *IEEE Trans. Plasma Sci.* 13 (1985) 480.
- [12] B. Hafizi, A. Ting, P. Sprangle and C.M. Tang, *Phys. Rev.* A38 (1988) 197.
- [13] M.N. Rosenbluth, H.V. Wong and B.N. Moore, private communication.
- [14] W.B. Colson, *Proc. SPIE* 453 (1984) 290.
- [15] S. Johnston, A.M. Sessler, Y.-J. Chen, W.M. Fawley and E.T. Scharlemann, private communication.
- [16] S.Y. Cai, A. Bhattacharjee, S.P. Chang, J.W. Dodd and T.C. Marshall, *Phys. Rev.* A40 (1989) 3127.

Statistical Properties of Wiggler and Bending-Magnet Radiation from the Brookhaven Vacuum-Ultraviolet Electron Storage Ring

Malvin C. Teich

*Columbia Radiation Laboratory, Departments of Electrical Engineering and Applied Physics,
Columbia University, New York, New York 10027*

Toshiya Tanabe and Thomas C. Marshall

Department of Applied Physics, Columbia University, New York, New York 10027

John Galayda^(a)

National Synchrotron Light Source, Brookhaven National Laboratory, Upton, New York 11973

(Received 17 September 1990)

The photoelectron counts of spontaneous light from the wiggler in the Brookhaven electron storage ring obey the negative-binomial distribution, in accord with the predictions of a multielectron, multimode theory. The bending-magnet light emerging from the Pyrex exit port of the storage ring obeys the Neyman type-A distribution.

PACS numbers: 42.55.Tb, 41.70.+t, 42.50.Bs

We have carried out a series of experiments on the photoelectron statistics associated with the radiation emitted from the vacuum-ultraviolet electron storage ring at the National Synchrotron Light Source at Brookhaven National Laboratory. The statistical properties of light emitted by electrons in a storage ring, and from free-electron lasers, are of interest inasmuch as sources such as these are being used in an increasingly broad range of applications.

There have been a number of theoretical investigations of the photon-number statistics of the radiation emitted from an electron beam as it propagates through a wiggler, i.e., the spontaneous emission from a free-electron laser.¹⁻⁵ A single electron gives rise to photons characterized by a Poisson photon-number distribution¹ $P(n)$, which has a variance given by

$$\text{Var}(n) = \langle n \rangle, \quad (1)$$

where $\langle n \rangle$ is the photon-number mean. However, the radiation from an electron beam is more properly described by a multielectron theory. Several researchers²⁻⁵ have shown that in this case

$$\text{Var}(n) = \langle n \rangle + \langle n \rangle^2 (1 - 1/N_e), \quad (2)$$

where $\langle n \rangle = N_e \langle a \rangle$, with N_e the (fixed) number of electrons in the bunch and $\langle a \rangle$ the mean number of photons spontaneously emitted by a single electron during a pass through the wiggler. This formula can be viewed⁶ as arising from a superposition of a fixed number N_e of independent, statistically identical coherent emissions, each of which contains a Poisson number of photons of mean $\langle a \rangle$. When $N_e \gg 1$, Eq. (2) reduces to the Bose-Einstein result associated with single-mode thermal light,⁶⁻⁸ i.e.,

$$\text{Var}(n) = \langle n \rangle + \langle n \rangle^2. \quad (3)$$

Although Eqs. (2) and (3) are obtained using a multielectron theory, they are not directly applicable to the light observed from a radiating electron beam because the polarization properties of the light, and the finite photodetector counting time, area, and quantum efficiency must be taken into account. These factors require a multimode, rather than a single-mode, description of thermal light.⁹ The detected photoelectrons are more properly described by the negative-binomial distribution,^{6,8-10} which has a variance given by

$$\text{Var}(m) = \langle m \rangle + \langle m \rangle^2 / M. \quad (4)$$

Here $\langle m \rangle = \eta \langle n \rangle$, where η is the optical-system quantum efficiency, and M is the number-of-modes (degrees-of-freedom) parameter, to be described subsequently. The description provided in Eq. (4) is, indeed, applicable for describing the light from many types of lasers operated below threshold. For $\eta = M = 1$, we recover the Bose-Einstein result of Eq. (3).

In our experiments, a single pulse of electrons with an approximate duration of 480 psec at a point on the exit window moves around the ring once each 170.2 nsec. This group of electrons produces a pulse of light as it passes through a linear wiggler placed in the storage ring, and it also generates bending-magnet (synchrotron) radiation as it passes through each of the bending magnets in the ring. The light is always produced from the same group of electrons since the current decay time (≈ 100 min) is much greater than the time of an experiment. The operating parameters of the wiggler and storage ring are provided in Table I.

The experimental arrangement for measuring the statistical properties of the wiggler light is schematically illustrated in Fig. 1. It makes use of an analog photoelectron-counting technique.¹¹ The radiation from the electrons as they pass through the wiggler takes the form

TABLE I. Wiggler (BNL designation U13-TOK) and storage-ring parameters used in our experiments. SQ represents the skew quadrupole parameter (SQ = 300 and 0 correspond to tightly focused and loosely focused electron beams, respectively).

Wiggler period, λ_0	10 cm
Number of wiggler periods, N	22.5
Peak wiggler magnetic field, B_0	0.61 T
Wiggler strength parameter, K ($K = eB_0\lambda_0/2\pi\sqrt{2}mc^2$)	4.0
Operating energy	≈ 650 MeV (wiggler light); ≈ 745 MeV (bending-magnet light)
Operating current	≈ 50 mA (wiggler light); ≈ 150 mA (bending-magnet light)
Horizontal damped emittance, ϵ_x	8.0×10^{-8} m rad (SQ = 300), 7.4×10^{-8} m rad (SQ = 0) (wiggler light); 1.5×10^{-7} m rad (bending-magnet light)
Vertical damped emittance, ϵ_y	2.0×10^{-8} m rad (SQ = 300), 2.6×10^{-8} m rad (SQ = 0) (wiggler light); $> 2.8 \times 10^{-10}$ m rad (bending-magnet light)
Source size, σ_h, σ_r	1.0 mm, 0.32 mm (SQ = 300), 0.96 mm, 0.36 mm (SQ = 0) (wiggler light); 0.5 mm, > 0.06 mm (bending-magnet light)

of brief pulses of light with a center wavelength of 532 nm (at the fundamental) and a full width at half maximum (FWHM) of ≈ 20 nm. These light pulses pass through the Pyrex exit port of the ring and are directed through an optical interference filter with a center wavelength of 532 nm and a FWHM of 3.2 nm. The operating energy of the ring was adjusted so that the fundamental wavelength of the wiggler light would precisely match the maximum-transmission wavelength of the interference filter. The light was focused by a 50-mm-focal-length glass lens onto a Si *p-i-n* photodiode detector with a quantum efficiency of 0.78.

The photodiode output is passed through a pair of cascaded video amplifiers, each with an input impedance of 50 Ω , a voltage gain of 10, and a bandwidth of 500 MHz. These amplify the pulses by a factor of 100 and broaden their width from 480 psec to 5 nsec (see Fig. 1). The pulses are then fed into a gated-integrator-boxcar-averager module. This device high-pass filters the pulses to eliminate noise below 10 kHz, and provides an electronic gate with a 15-nsec width. It provides an output for every thousandth pulse, as selected by a cascade of three divide-by-ten counters which are triggered by the

ring clock. The time between the selected pulses of light is therefore 170 μ sec, which is sufficiently slow for the electronics to register them. The selected pulses are then integrated and amplified (in this same processor) to produce a sequence of voltages, following each pulse, that is proportional to its integrated current, i.e., to its charge. A 10- μ sec-width sample of each of these voltages is obtained by using a digital-delay-pulse generator synchronized to the pulses, in conjunction with an integrated-circuit switch. This sequence of voltage samples, after suitable normalization, represents the numbers of photoelectrons per pulse. They are fed to a multichannel analyzer (2048 bins) which sorts them into a histogram that represents the photoelectron-counting distribution $P(m)$. The typical time to collect a distribution is ≈ 5 sec, during which a total of ≈ 30000 samples are collected (in some experiments only 15000 samples were registered).

The system noise was determined by feeding a sequence of identical deterministic electrical pulses (in place of the photodiode output) into the amplifier and then measuring the variance at the output of the multichannel analyzer as a function of the pulse level. The resultant noise-count variance was found to be approximately constant at $\approx 3 \times 10^8$ for count means above 5×10^6 ; however, it decreased with decreasing count mean below this value.

The experimental photoelectron-counting distribution $P(m)$ is shown in Fig. 2(a) for the wiggler light. The mean photoelectron number for this particular distribution was adjusted to be $\approx 9.8 \times 10^6$ by means of the neutral-density filter placed in front of the lens. The experimental distribution is nicely fitted by a negative-binomial theoretical distribution convolved with a zero-mean Gaussian distribution (with variance of 3×10^8) representing the system noise. The experimentally determined number of modes is $M \approx 54000$.

In another set of experiments, the wiggler was effectively removed (by increasing the gap between the magnets) and the photoelectron-counting distribution of the

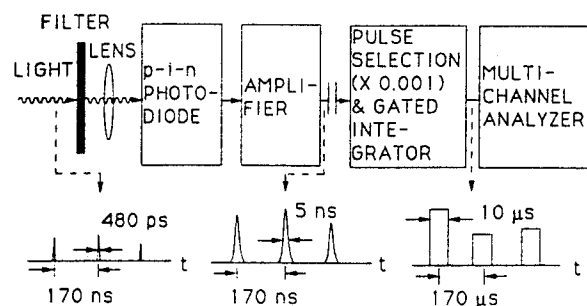


FIG. 1. Block diagram of the experimental arrangement used for the analog measurement of the photoelectron-counting distribution of wiggler light. The apparatus is operated in a slightly different configuration for obtaining the distribution of bending-magnet light (see text).

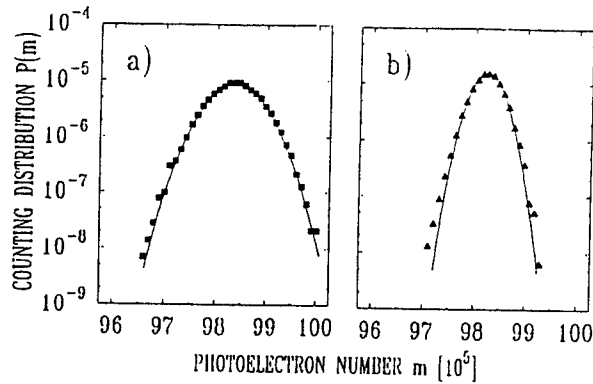


FIG. 2. (a) Squares represent the photoelectron-counting distribution $P(m)$ vs the photoelectron number m for wiggler light from a tightly focused electron beam. The data are well fitted by a negative-binomial distribution convolved with a Gaussian representing the system noise (solid curve). (b) Triangles represent $P(m)$ vs m for bending-magnet light. The data are well fitted by the Neyman type-A distribution convolved with the same Gaussian (solid curve).

bending-magnet light emerging from the Pyrex exit port of the storage ring was measured. The experimental arrangement is similar to that shown in Fig. 1 with the following exceptions (see Table I): The interference filter was removed to increase the photon flux entering the system; the operating energy of the ring was set at the normal value since it was not necessary to adjust the center wavelength of the light to the interference-filter maximum; the operating current was increased since the heating limitations imposed by the wiggler were not present; and the electron-beam emittance and source sizes were somewhat different.

The bending-magnet light in the ring is broadband with photon energies that stretch into the x-ray region. As a consequence of the short coherence time of this light, we would expect that the detected photons, if they were able to be measured directly, would obey the negative-binomial distribution with a value of M sufficiently large that the Poisson distribution would provide a good approximation.

The experimental photoelectron-counting distribution for the bending-magnet light is shown in Fig. 2(b). The mean photoelectron number was adjusted to be $\approx 9.8 \times 10^6$, the same as for the wiggler light shown in Fig. 2(a). The distribution associated with this light does not obey the Poisson distribution. Instead, it turns out to be well fitted by a Neyman type-A (NTA) distribution¹²⁻¹⁴ convolved with the same zero-mean Gaussian noise distribution used for Fig. 2(a). The NTA distribution, which has a variance given by^{6,10,14}

$$\text{Var}(m) = (1 + \eta\langle a \rangle)\langle m \rangle, \quad (5)$$

provides a good approximation for describing the statistics of luminescence light with an arbitrary spectrum.^{13,14} Here $\langle m \rangle = \eta\langle n \rangle$, where η is the optical-sys-

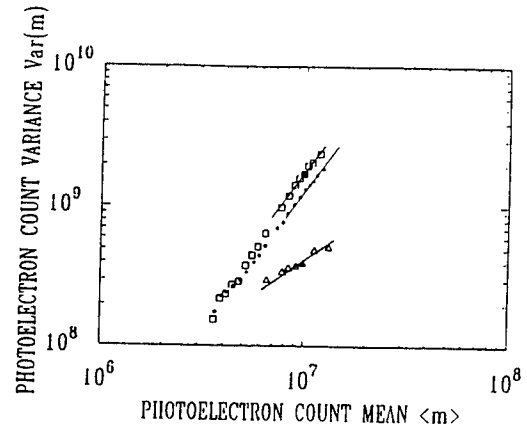


FIG. 3. Photoelectron-count variance vs count mean for wiggler light from a tightly focused electron beam (squares), a loosely focused electron beam (dots), and for bending-magnet light (triangles). The noise variance has been subtracted from the data as plotted. The count variance increases with the square of the mean for wiggler light, and directly in proportion to the mean for bending-magnet light. The solid square and triangle are the data points corresponding to the full counting distributions presented in Figs. 2(a) and 2(b), respectively.

tem quantum efficiency, and, in the context of luminescence, $\langle n \rangle$ is the secondary photon-number mean and $\langle a \rangle$ is the mean number of secondary photons per primary Poisson event.¹² It is determined from the data in Fig. 2 that $\eta\langle a \rangle \approx 45$.

We have experimentally verified that the wiggler light and bending-magnet light obey different functional forms for the variance, as given in Eqs. (4) and (5), respectively. The results are illustrated in Fig. 3 for wiggler light with a tightly focused electron beam (squares), a loosely focused electron beam (dots), and for bending-magnet light (triangles). The maximum photoelectron count mean ($\approx 10^7$) was governed by the storage-ring current specified in Table I. Lower count means $\langle m \rangle$ were obtained by the use of the variable neutral-density filter in front of the lens and, to a lesser degree, by the loss of electrons during the duration of an experimental run. It is clear from Fig. 3 that the variance of the wiggler light does indeed vary as $\langle m \rangle^2$, as expected from Eq. (4) since $\langle m \rangle \gg M$, and the variance of the bending-magnet light varies as $\langle m \rangle$ in accordance with Eq. (5).

Using Eq. (4), the number of modes M was determined from the experimental wiggler-light curves in Fig. 3 to be ≈ 54000 and 78000 for the tightly focused and loosely focused electron beams, respectively. It is difficult to precisely estimate the expected number of modes M without knowing the spatiotemporal correlation properties of the light. Nevertheless, M was estimated to be a product of three factors, associated with time, area, and polarization. We assumed that $M \approx M_T M_A M_P \approx (T/\tau_c)(A/A_c)[2/(1+P)]$, with T the counting time,

τ_c the coherence time of the light, A the photodiode active area, A_c the coherence area of the light, and P the degree of polarization. This expression is appropriate for cross spectrally pure light⁸ when the first two factors are substantially greater than unity. These factors are roughly estimated to be $M_T \approx 2450$, using $\tau_c \approx 0.2$ psec as determined by the Gaussian passband of the interference filter; $M_A \approx 27.2$ and ≈ 30.5 , for the tightly focused and loosely focused beams, respectively (assuming that M_A , which depends on the emittance, can be reasonably represented as the calculated ratio of the total photon flux to the coherent photon flux¹⁵); and the measured degree of polarization $P=0.87$. The theoretically expected results for M are therefore ≈ 71000 and ≈ 80000 for the tightly focused and loosely focused electron beams, respectively, which are not in unreasonable agreement with the measured values given the large uncertainties involved. In other series of experiments, conducted using either longer pulse widths, unfocused wiggler light, or rectangular slits (in the horizontal or vertical direction), we obtained values of M that varied in the expected manner.

Using Eq. (5), it was determined that $\eta\langle\alpha\rangle \approx 40$ for the collection of triangular data points in Fig. 3 [the specific data point used for Fig. 2(b) had a value $\eta\langle\alpha\rangle \approx 45$]. One possible reason that the bending-magnet light emerging from the Pyrex exit port of the storage ring might obey the NTA distribution is as follows. A high-energy photon, when striking an optical material, can give rise to many visible photons through photoluminescence, as occurs in a scintillation crystal.¹³ If the photon-number statistics of a pulse of synchrotron light inside the ring were Poisson, as expected, and the number of visible luminescence photons α created per energetic synchrotron photon were also Poisson, the resulting photoelectron statistics would be describable by the NTA distribution.¹³ The light emitted by a mechanism such as this would be diffuse, in accord with our observations. The photoluminescence explanation fails in one respect, however. From Eq. (5) it is seen that the quantum efficiency η multiplies the mean number of secondary photons per primary event $\langle\alpha\rangle$. The slope of the curve fitting the triangles in Fig. 3 should therefore vary as different neutral-density filters change the value of η , which it does not appear to do. The explanation of why the NTA distribution fits the bending-magnet light so well therefore requires further investigation.

With respect to the spontaneous wiggler light, we con-

clude that the applicability of the multimode thermal model is supported by the fit of the negative-binomial theoretical photoelectron-counting distribution to the data, by the observed quadratic dependence of the count variance on the count mean, and by the reasonable agreement of the theoretical estimates of the number of modes M with our observations. It is, perhaps, worthy of mention that the dependence of the variance on the mean was also quadratic for third-harmonic wiggler light at 532 nm, obtained by operating the ring at ≈ 375 MeV. It will be useful to conduct further studies to verify that other measures of the photoelectron point process^{6,8} are consistent with the multimode thermal model for wiggler light.

We are grateful to C. Pellegrini for valuable discussions and suggestions. This work was supported by the Joint Services Electronics Program through the Columbia Radiation Laboratory, by Brookhaven National Laboratory, and by the Office of Naval Research.

^(a)Present address: Argonne National Laboratory, Argonne, IL 60439.

¹R. Bonifacio, *Opt. Commun.* **32**, 440 (1980).

²W. Becker and J. K. McIver, *Phys. Rev. A* **27**, 1030 (1983).

³W. Becker and J. K. McIver, *Phys. Rev. A* **28**, 1838 (1983).

⁴A. T. Georges, in *Free-Electron Generators of Coherent Radiation*, edited by C. A. Brau, S. F. Jacobs, and M. O. Scully [Proc. SPIE Int. Soc. Opt. Eng. **453**, 297 (1984)].

⁵J. Gea-Banacloche, *Phys. Rev. A* **31**, 1607 (1985).

⁶M. C. Teich and B. E. A. Saleh, in *Progress in Optics*, edited by E. Wolf (North-Holland, Amsterdam, 1988), Vol. 26, pp. 1-104, Eqs. (2.22), (2.23), and (2.56).

⁷S. Benson and J. M. J. Madey, *Nucl. Instrum. Methods Phys. Res., Sect. A* **237**, 55 (1985).

⁸B. Saleh, *Photoelectron Statistics* (Springer-Verlag, New York, 1978).

⁹G. Bédard, J. C. Chang, and L. Mandel, *Phys. Rev.* **160**, 1496 (1967).

¹⁰M. C. Teich and B. E. A. Saleh, *Opt. Lett.* **7**, 365 (1982).

¹¹P.-L. Liu, L. E. Fencil, J.-S. Ko, I. P. Kaminow, T. P. Lee, and C. A. Burrus, *IEEE J. Quantum Electron.* **19**, 1348 (1983).

¹²M. C. Teich, *Appl. Opt.* **20**, 2457 (1981).

¹³B. E. A. Saleh, J. T. Tadolacci, and M. C. Teich, *IEEE J. Quantum Electron.* **17**, 2341 (1981).

¹⁴M. C. Teich and B. E. A. Saleh, *J. Mod. Opt.* **34**, 1169 (1987).

¹⁵K.-J. Kim, *Nucl. Instrum. Methods Phys. Res., Sect. A* **246**, 71 (1986).

Linear theory of superradiance in a free-electron laser

S. Y. Cai, J. Cao, and A. Bhattacharjee

Department of Applied Physics, Columbia University, New York, New York 10027

(Received 6 November 1989; revised manuscript received 11 May 1990)

This study is motivated by the analytical solutions of superradiance in a high-gain free-electron laser obtained by Bonifacio, Maroli, and Piovella, using the technique of Laplace transforms [Opt. Commun. **68**, 369 (1988)]. An error in these analytical solutions is remedied by a correct treatment of the boundary conditions on the electron beam, and the earlier theory is extended to allow for both electron shot noise and an optical pulse in the initial state. It is shown that, when the optical pulse is shorter than the electron pulse, superradiant behavior can also occur at the leading edge of the optical pulse.

I. INTRODUCTION

In a free-electron laser (FEL), a relativistic electron beam passes through the transverse periodic magnetic field of an undulator (or wiggler), transferring energy to a copropagating electromagnetic wave. For the device to generate coherent radiation, it is necessary to satisfy a resonance condition which requires the electrons to slip one wavelength behind the radiation as the electrons pass over one undulator period. When this resonance condition is satisfied, the electron beam, after traveling a distance z , lags behind the optical beam by a slippage distance given by

$$S = (\lambda_s / \lambda_w) z, \quad (1)$$

where λ_s and λ_w are, respectively, the wavelength of the radiation and the undulator. A standard approximation, frequently made in theoretical analyses, is to take the slippage distance S to be much smaller than the input electron pulse length L_B (or optical pulse length L). In this "long-pulse" approximation, one can follow electrons within one period of the ponderomotive potential well and assume that electrons in adjacent wells satisfy a periodic boundary condition. This approximation is clearly violated if $S \geq L_B$; even if $S < L_B$, the periodic boundary condition does not hold at the edge of the electron pulse.

Recently, Bonifacio, Maroli, and Piovella¹ have presented some interesting analytical solutions in the linear regime taking into account the effect of slippage. Two distinct regimes are identified in Ref. 1. In one regime, referred to hereafter as the steady-state regime, the effect of slippage can be neglected, and the intensity scales as $n_e^{4/3}$, where n_e is the electron density. In the other regime, the effect of slippage is crucial, and the peak intensity scales as n_e^2 . This latter regime is shown to be significant when the slippage distance S is comparable with or larger than the electron pulse length. By analogy with laser physics,² Bonifacio and Casagrande have termed this regime the "superradiant" regime,^{1,3} though it has been noted in Ref. 4 that perhaps the term "superfluorescence" is more appropriate. The oc-

currence of superradiance has been confirmed by recent numerical simulations.^{4,5}

Analytical solutions describing superradiant behavior have been obtained in Ref. 1 by using Laplace transforms. Particular solutions have been given for the start-up of a high-gain FEL from initial conditions of zero optical field and electron shot noise. While these solutions predict correctly the existence of the superradiant regime for $S \leq L_B$, we show that the analysis given in Ref. 1 is not quite correct for $S > L_B$, which is precisely when superradiance is expected to be a dominant effect. In particular, we show that the evolution of the radiation field is qualitatively distinct in the two cases $S = L_B$ and $S > L_B$, a distinction that has not been made in the analytical treatment of Ref. 1. Thereafter, we give general solutions for the evolution of the radiation field in the presence of a finite optical pulse of length L at input. A new result that follows is the occurrence of superradiance at the leading edge of the optical pulse when $L < L_B$. (A preliminary account of these results was presented recently.⁶)

II. DYNAMICAL EQUATIONS

We begin our analysis with the one-dimensional FEL equations^{7,8}

$$\frac{d\gamma_j}{dz} = -\frac{k_s a_s a_w}{\gamma_j} \sin(\psi_j + \phi), \quad (2a)$$

$$\frac{d\psi_j}{dz} = k_w \left[1 - \frac{\gamma_r^2}{\gamma_j^2} \right] + \frac{k_s a_s a_w \cos(\psi_j + \phi)}{\gamma_j^2}, \quad (2b)$$

and

$$\left[\frac{\partial}{\partial z} + \frac{1}{c} \frac{\partial}{\partial t} \right] u = \frac{ia_w \omega_p^2}{2k_s c^2} \left\langle \frac{\exp(-i\psi)}{\gamma} \right\rangle, \quad (2c)$$

where z is the direction of propagation of the electron and optical beams and also coincides with the undulator axis; $\psi_j + \phi$ is the relative phase of the electron (of rest mass m) with respect to the radiation field, and $\psi_j mc^2$ is its energy; $\mathbf{A} = \mathbf{A}_w + \mathbf{A}_s$, $a_w = eA_w/mc^2$, $a_s = eA_s/mc^2$; $k_w, k_s = \omega/c$ are the wave numbers of the undulator and

radiation fields, respectively; ω is the radiation frequency; $u = a_s \exp(i\phi)$ is the complex amplitude of the radiation field; and γ_r is the resonant electron energy factor, defined by the relation

$$\gamma_r^2 = \frac{k_s(1 + a_w^2)}{2k_w} \quad (3)$$

The symbol $\langle \rangle$ denotes an ensemble average over electrons.

We introduce the following variable definitions:

$$\Gamma_j = (\gamma_j - \gamma_0) / \gamma_0, \quad (4a)$$

$$\delta = k_w(1 - \gamma_r^2 / \gamma_0^2), \quad (4b)$$

$$\Psi_j = \psi_j - \delta z, \quad (4c)$$

$$A = u \exp(i\delta z). \quad (4d)$$

Here γ_0 is the initial energy of the electron beam, taken to be monoenergetic. By linearizing Eqs. (2) around the equilibrium, $\Gamma_{j0} = 0$, $\langle \exp(-i\Psi_0) \rangle = 0$, $A_0 = 0$, and introducing collective variables $x = -\langle i\delta\Psi \exp(-i\Psi_0) \rangle$ and $y = \langle \Gamma \exp(-i\Psi_0) \rangle$, where $\delta\Psi_j = \Psi_j - \Psi_{j0}$, Γ_j and A are small quantities, we obtain the system of equations

$$\frac{dx}{dz} = -ihy - ifA, \quad (5a)$$

$$\frac{dy}{dz} = ifA, \quad (5b)$$

$$\left[\frac{\partial}{\partial z} + \frac{1}{c} \frac{\partial}{\partial t} \right] A = i\delta A + ig(x - y), \quad (5c)$$

where $f \equiv k_s a_w / (2\gamma_0^2)$, $g \equiv \omega_p^2 a_w / (2k_s c^2 \gamma_0)$, and $h \equiv 2k_w \gamma_r^2 / \gamma_0^2$. Note that in Eq. (5c) the parameter g depends on the density of the electron beam and is zero outside the beam. Inspection of the analogous equation in Ref. 1 [Eq. (4c)] shows that the explicit dependence of the radiation equation on the electron density is obscured by the dimensionless variables used. Since the phenomenon of superradiance occurs at the edges of an electron beam, it is important to track this density dependence explicitly in order that the boundary conditions on the beam can be imposed correctly.

We assume that the electrons are continuously distributed along the interaction region inside the pulse so that the electron beam can be treated as a fluid, each element of which moves at the average speed $\beta_{||} = V_{||} / c$. Hence the Lagrangian derivative along z in Eqs. (5a) and (5b) can be replaced by the Eulerian derivative, that is,

$$\frac{d}{dz} = \frac{\partial}{\partial z} + \frac{1}{\beta_{||} c} \frac{\partial}{\partial t}. \quad (6)$$

It is convenient to transform to the coordinates,

$$\xi = z, \quad (7)$$

$$\tau = \frac{z - \beta_{||} ct}{1 - \beta_{||}}, \quad (8)$$

where τ measures the position in the electron-beam frame. We choose the origin $z=0$ to coincide with the

beginning of the undulator. Equations (5) can then be solved by Laplace transforms. For a function $F(\xi, \tau)$, the Laplace transform is defined by

$$\bar{F}(p, \tau) = \int_0^\infty d\xi \exp(-p\xi) F(\xi, \tau). \quad (9)$$

Equations (5) then yield the ordinary differential equation

$$\frac{d\bar{A}}{d\tau} + \left[p - i\delta - \frac{2fg}{p} - \frac{ifgh}{p^2} \right] \bar{A} = A_0 + ig \frac{x_0 - y_0}{p} + \frac{ghy_0}{p^2}, \quad (10)$$

where $A_0 \equiv A(z=0, \tau)$, $x_0 \equiv x(z=0, \tau)$, and $y_0 \equiv y(z=0, \tau)$ represent initial conditions at $z=0$. For simplicity we will take $y_0=0$, and assume that the initial electron and optical pulses to be rectangular and of lengths L_B and L , respectively, with their trailing edges aligned at $z=0$ when $\tau=0$. Note that the slippage is then given by $\tau = \xi$.

III. ANALYTICAL SOLUTIONS FOR ZERO INITIAL RADIATION FIELD

In order to compare the results of our analysis with that of Ref. 1, we first consider the simple case $A_0=0$. Then Eq. (10) can be integrated in τ to give

$$\bar{A}(p, \tau) = \begin{cases} \frac{igx_0}{p\lambda(p)} \{1 - \exp[-\lambda(p)\tau]\}, & 0 \leq \tau \leq L'_B \\ \frac{igx_0}{p\lambda(p)} \exp[-(p-i\delta)(\tau-L'_B)] \\ \quad \times \{1 - \exp[-\lambda(p)L'_B]\}, & L'_B < \tau \end{cases} \quad (11)$$

where $\lambda(p) \equiv p - i\delta - 2fg/p - ifgh/p^2$ and $L'_B \equiv L_B / (1 - \beta_{||})$. In obtaining Eq. (11), we have imposed the condition that \bar{A} is continuous at $\tau = L'_B$.

The inverse Laplace transform of $\bar{A}(p, \tau)$ is given by the standard formula

$$A(\xi, \tau) = \frac{1}{2\pi i} \int_{c_0 - i\infty}^{c_0 + i\infty} \exp(p\xi) \bar{A}(p, \tau) dp, \quad (12)$$

where c_0 is chosen large enough so that all singularities of the integrand lie to the left of the straight line along which the integral is taken. From Eq. (11), we then obtain the following solutions for $A(\xi, \tau)$: for $0 \leq \tau \leq L'_B$ and $\xi > \tau$

$$A = \text{Res} \left[-\frac{igx_0}{p\lambda(p)} \exp[p\xi - \lambda(p)\tau] \right] \Big|_{p=0}, \quad (13)$$

where $\text{Res}(\cdot) \Big|_{p=0}$ denotes the Cauchy residue at $p=0$. For $\xi \leq \tau \leq L'_B$

$$A = \sum_{l=1}^3 \frac{igx_0 p_l}{(p_l - p_m)(p_l - p_n)} \exp(p_l \xi), \quad l \neq m \neq n \quad (14)$$

where p_l ($l=1,2,3$) are the three roots of the cubic equation $p^2 \lambda(p) = 0$. For $\xi > \tau > L'_B$

$$A = \text{Res} \left[-\frac{igx_0}{p\lambda(p)} \exp[-(p-i\delta)(\tau-L'_B)] - \lambda(p)L'_B + p\xi \right] \Big|_{p=0}. \quad (15)$$

For $\tau > \xi > \tau - L'_B$ and $\tau > L'_B$

$$A = \sum_{l=1}^3 \frac{igx_0 p_l}{(p_l - p_m)(p_l - p_n)} \exp[p_l \xi - (p_l - i\delta)(\tau - L'_B)], \quad l \neq m \neq n. \quad (16)$$

Finally, for $\tau > \xi + L'_B$

$$A = 0. \quad (17)$$

Note that solutions (13) and (14) are similar to those obtained by Bonifacio *et al.*¹ Solution (13) is the superradiant solution.

On the basis of the solutions given above, we can depict schematically the optical amplitude $|A|$ as a function of τ at a fixed value of ξ . Figure 1(a) describes the case

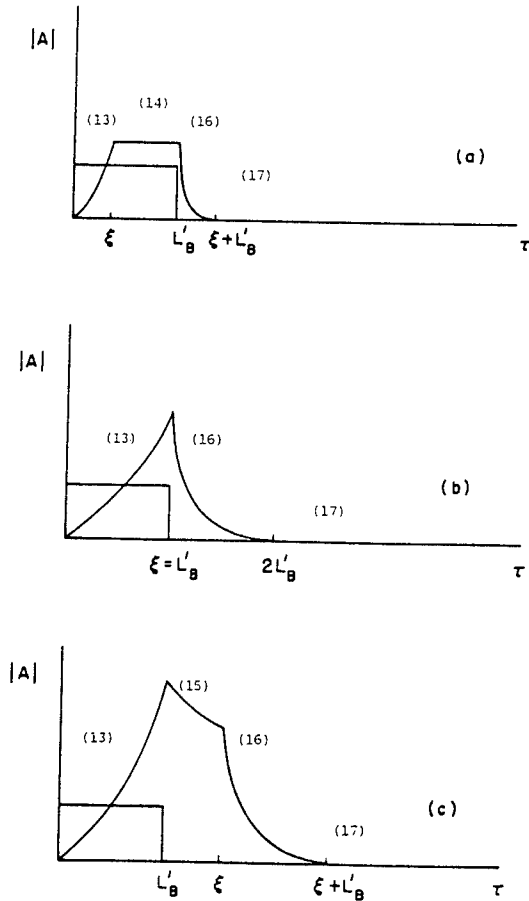


FIG. 1. Schematic plots of the optical amplitude as a function of τ , in the case of zero initial optical field. The amplitude is viewed at three positions in the undulator: (a) $S < L_B$ (or $\xi < L'_B$), (b) $S = L_B$ (or $\xi = L'_B$), and (c) $S > L_B$ (or $\xi > L'_B$). The rectangles stand for the electron pulse and the number in parentheses above each sector of a curve is the equation number in the text that describes that sector.

$S < L_B$ (or $\xi < L'_B$), which corresponds to the long-pulse limit. There are three regions: the exponentially growing region ($\xi + L'_B > \tau > L'_B$), the steady-state region ($L'_B > \tau > \xi$), and the superradiant region ($\xi > \tau > 0$). Figure 1(b) describes the special case $S = L_B$, in which case the steady-state region disappears. Figures 1(a) and 1(b) are similar to that given in Ref. 1.

Figure 1(c) describes the case $S > L_B$ (or $\xi > L'_B$), which corresponds to a short electron pulse. In this case our results are significantly different from the results of Ref. 1, in which no distinction is made between the cases $S = L_B$ and $S > L_B$. Contrasting Figs. 1(a) and 1(b), we note that for $S > L_B$ a new region appears for τ in the range $L'_B < \tau < \xi$. The solution for this region is given by Eq. (15), and is of the superradiant type. The physical mechanism for the occurrence of this region is as follows. As the radiation pulse interacts with and eventually passes over the leading edge of the electron pulse, the superradiance within the electron pulse grows and eventually slips out of the leading edge of the electron pulse. However, once the radiation slips out of the electron pulse, it can no longer grow, and merely oscillates with the phase $\exp(i\delta\tau)$, with an amplitude that depends on $(\xi - \tau)$.

IV. ANALYTICAL SOLUTIONS WITH NONZERO RADIATION FIELD

We now study the case when $A_0 \neq 0$. For specificity, we assume that the electron and optical pulses are rectangular, as is shown in Fig. 2. In general $L_B \neq L$, and we allow for both possibilities, $L_B > L$ or $L_B < L$. We define $L' \equiv L/(1 - \beta_{||})$.

We first look at the case $L > L_B$. In this case, the solution to Eq. (10) is

$$\tilde{A} = \begin{cases} \frac{A_0 + igx_0/p}{\lambda(p)} \{1 - \exp[-\lambda(p)\tau]\}, & 0 \leq \tau \leq L'_B \\ \frac{A_0 + igx_0/p}{\lambda(p)} \exp[-(p-i\delta)(\tau-L'_B)] \\ \times \{1 - \exp[-\lambda(p)L'_B]\} \\ + \frac{A_0}{p-i\delta} \{1 - \exp[-(p-i\delta)(\tau-L'_B)]\}, & L'_B < \tau \leq L' \end{cases} \quad (18)$$

$$\begin{cases} \frac{A_0 + igx_0/p}{\lambda(p)} \exp[-(p-i\delta)(\tau-L'_B)] \\ \times \{1 - \exp[-\lambda(p)L'_B]\} \\ + \frac{A_0}{p-i\delta} \{1 - \exp[-(p-i\delta)(L'-L'_B)]\} \\ \times \exp[-(p-i\delta)(\tau-L')], & L' < \tau. \end{cases}$$

The inverse Laplace transform gives the following solutions: for $0 \leq \tau \leq \min(L'_B, \xi)$

$$A = \text{Res} \left[-\frac{A_0 + igx_0/p}{\lambda(p)} \exp[-\lambda(p)\tau + p\xi] \right] \Big|_{p=0}, \quad (19)$$

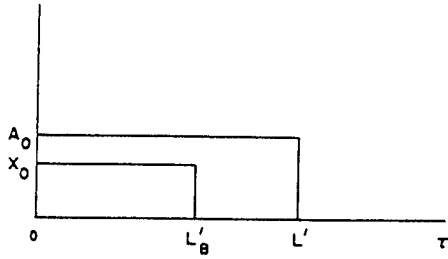


FIG. 2. Initial electron shot noise and optical input pulse. Here the electron pulse length L'_B can be either greater or smaller than the optical pulse length L' .

which is again the superradiant solution. For $\xi \leq \tau < L'_B$

$$A = \sum_{l=1}^3 \frac{(p_l A_0 + i g x_0) p_l}{(p_l - p_m)(p_l - p_n)} \exp(p_l \xi), \quad l \neq m \neq n \quad (20)$$

which is the steady-state solution. For $L'_B \leq \tau < \xi$

$$A = \text{Res} \left[-\frac{A_0 + i g x_0 / p}{\lambda(p)} \times \exp[p \xi - \lambda(p) L'_B] - (p - i \delta)(\tau - L'_B) \right] \Big|_{p=0}, \quad (21)$$

which is the superradiance that has slipped out of the leading edge of the electron pulse. For $\max(\xi, L'_B) \leq \tau < \xi + L'_B$

$$A = \exp[i \delta(\tau - L'_B)] \sum_{l=1}^3 \frac{(p_l A_0 + i g x_0) p_l}{(p_l - p_m)(p_l - p_n)} \times \exp[p_l(\xi - \tau + L'_B)], \quad l \neq m \neq n. \quad (22)$$

For $\xi + L'_B \leq \tau < \xi + L'$

$$A = A_0 \exp(i \delta \xi), \quad (23)$$

which is the part of the initial optical pulse that does not interact with the electron pulse, so that $u = A \exp(-i \delta z) = A_0$ remains constant. Finally, for $\xi + L' < \tau$

$$A = 0. \quad (A24)$$

The solutions (19)–(24) are schematically drawn in Fig. 3. Figure 3(a) describes the case $\xi < L'_B$, Fig. 3(b) the case $\xi = L'_B$, and in Fig. 3(c) the case $\xi > L'_B$. Note that these solutions reduce to the special case discussed in Sec. III if we set $A_0 = 0$.

We now show that the radiation growing at the trailing edge has indeed the scaling properties of superradiance. To see this, we look at the first term in (19), which we write as

$$A_1 = \text{Res} \left[-\frac{A_0}{\lambda(p)} \exp[-\lambda(p) \tau + p \xi] \right] \Big|_{p=0}. \quad (25)$$

To make the problem simpler, we assume that the FEL is

perfectly tuned, so that $\delta = 0$, and we neglect the small term $2fg/p$ in $\lambda(p)$. Then A_1 becomes

$$A_1 = \text{Res} \left[-\frac{A_0 p^2}{p^3 - i f g h} \times \exp \left[p(\xi - \tau) + \frac{i f g h}{p^2} \tau \right] \right] \Big|_{p=0} \\ = \frac{A_0}{i f g h} \sum_{l=0}^{\infty} \sum_{n=0}^{\infty} \sum_{m=0}^{\infty} \left[\frac{1}{i f g h} \right]^l \frac{(\xi - \tau)^n (i f g h)^m}{n! m!}, \quad (26)$$

where $3l + n - 2m = -3$. In the short-pulse limit, $f g h \tau \ll 1$, and at $\tau = \xi$, only $N=0$ terms contribute. Therefore the leading term in (26) is the term with $n=0$, $m=3$, and $l=1$. Then

$$A_1 \sim \frac{A_0}{i f g h} \frac{1}{i f g h} \frac{(i f g h \tau)^3}{6} = \frac{i A_0}{6} f g h \tau^2 \sim n_e, \quad (27)$$

which implies that the radiation intensity scales as n_e^2 .

We now consider the complementary case $L < L_B$. This case describes what happens in an FEL oscillator in

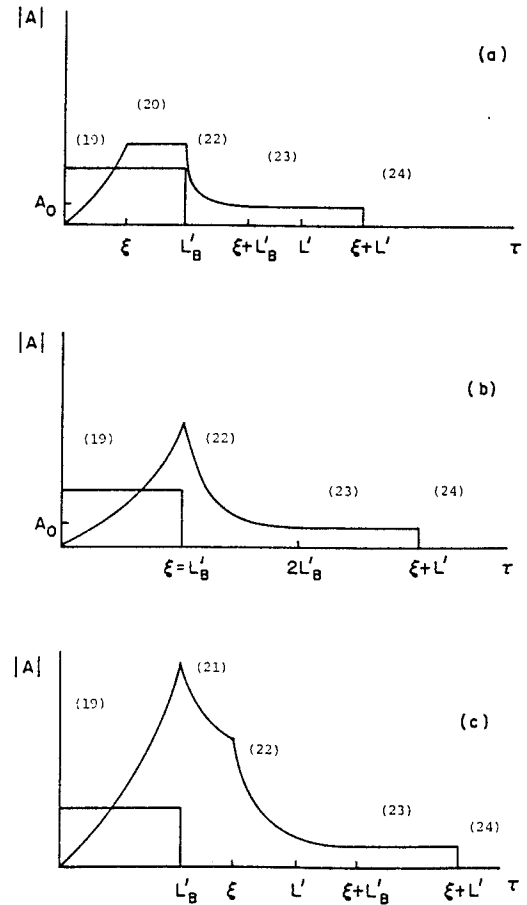


FIG. 3. Schematic plots of the optical field amplitude as a function of τ , in the case of a nonzero initial optical pulse and $L > L_B$ (or $L' > L'_B$). The amplitude is viewed at three positions in the undulator: (a) $S < L_B$ (or $\xi < L'_B$), (b) $S = L_B$ (or $\xi = L'_B$), and (c) $S > L_B$ (or $\xi > L'_B$).

which the optical pulse is shorter than the electron pulse and their trailing edges are aligned at the entry of the undulator. In this case, the solution to Eq. (10) is

$$\bar{A} = \begin{cases} \frac{A_0 + igx_0/p}{\lambda(p)} \{1 - \exp[-\lambda(p)\tau]\}, & 0 \leq \tau \leq L' \\ \frac{A_0 + igx_0/p}{\lambda(p)} \{ \exp[-\lambda(p)(\tau - L')] - \exp[-\lambda(p)\tau] \} \\ + \frac{igx_0/p}{\lambda(p)} \{1 - \exp[-\lambda(p)(\tau - L')]\}, & L' < \tau \leq L'_B \quad (28) \\ \left[\frac{A_0 + igx_0/p}{\lambda(p)} \{ \exp[-\lambda(p)(L'_B - L')] - \exp[-\lambda(p)L'_B] \} \right. \\ \left. + \frac{igx_0/p}{\lambda(p)} \{1 - \exp[-\lambda(p)(L'_B - L')]\} \right] \\ \times \exp[-(p - i\delta)(\tau - L'_B)], & L'_B \leq \tau. \end{cases}$$

The inverse Laplace transformation of (28) gives the following results: for $0 \leq \tau < \min(\xi, L')$

$$A = \text{Res} \left[-\frac{A_0 + igx_0/p}{\lambda(p)} \exp[-\lambda(p)\tau + p\xi] \right] \Bigg|_{p=0}, \quad (29)$$

which is the same as Eq. (19) and is the superradiant solution. For $\xi \leq \tau < L'$

$$A = \text{Res} \left[\frac{A_0}{\lambda(p)} \{ \exp[-\lambda(p)(L'_B - L')] - \exp[-\lambda(p)L'_B] \} - \frac{igx_0}{p\lambda(p)} \exp[-\lambda(p)(L'_B - L')] \exp[-(p - i\delta)(\tau - L'_B) + p\xi] \right] \Bigg|_{p=0}. \quad (34)$$

For $\max(\xi, L'_B) \leq \tau < \xi + L'$ and $\xi > L'_B - L'$

$$A = \sum_{l=1}^3 \frac{(p_l A_0 + igx_0)p_l}{(p_l - p_m)(p_l - p_n)} \exp[-(p_l - i\delta)(\tau - L'_B) + p_l \xi] + \text{Res} \left[\frac{A_0}{\lambda(p)} \exp[-\lambda(p)(L'_B - L') - (p - i\delta)(\tau - L'_B) + p\xi] \right] \Bigg|_{p=0}, \quad (35)$$

which is again a combination of the steady-state and superradiant solutions. For $\max(\xi + L', L'_B) \leq \tau < \xi + L'_B$

$$A = \sum_{l=1}^3 \frac{igx_0 p_l}{(p_l - p_m)(p_l - p_n)} \times \exp[-(p_l - i\delta)(\tau - L'_B) + p_l \xi]. \quad (36)$$

For $\xi + L'_B < \tau$

$$A = 0. \quad (37)$$

$$A = \sum_{l=1}^3 \frac{(A_0 + igx_0/p_l)p_l^2}{(p_l - p_m)(p_l - p_n)} \exp(p_l \xi), \quad l \neq m \neq n, \quad (30)$$

which is the same as (20) and is the steady-state solution. For $L' \leq \tau < \min(\xi, L'_B)$ and $L' < \xi$

$$A = \text{Res} \left[\frac{A_0 + igx_0/p}{\lambda(p)} \{ \exp[-\lambda(p)(\tau - L')] - \exp[-\lambda(p)\tau] \} \exp(p\xi) - \frac{igx_0}{p\lambda(p)} \exp[-\lambda(p)(\xi - L')] + p\xi \right] \Bigg|_{p=0}. \quad (31)$$

For $\max(\xi, L') \leq \tau < \min(\xi + L', L'_B)$ and $\xi < L'_B$

$$A = \text{Res} \left[\frac{A_0}{\lambda(p)} \exp[-\lambda(p)(\tau - L') + p\xi] \right] \Bigg|_{p=0} + \sum_{l=1}^3 \frac{(p_l A_0 + igx_0)p_l}{(p_l - p_m)(p_l - p_n)} \exp(p_l \xi), \quad l \neq m \neq n \quad (32)$$

which is a new solution. The first term in (32) is of the same form as Eq. (25), describing superradiance growing from A_0 . Therefore (32) is a combination of the superradiant and steady-state solutions. For $\xi + L' \leq \tau < \xi + L'_B$ and $\xi < L'_B - L'$

$$A = \sum_{l=1}^3 \frac{igx_0 p_l}{(p_l - p_m)(p_l - p_n)} \exp(p_l \xi), \quad l \neq m \neq n \quad (33)$$

is another steady-state solution. For $L'_B \leq \tau < \xi$

Solutions (29)–(37) for the amplitude of the optical pulse are represented schematically in Figs. 4–6. In Fig. 4, we plot the case $S < L$ (or $\xi < L'$), which describes a long electron pulse. When the slippage is small so that $S + L < L_B$ (or $\xi + L' < L'_B$), there are, as shown in Fig. 4(a), two regions of steady-state behavior separated by a region that contains a combination of steady-state and superradiant behavior. However, as shown in Fig. 4(b), when the slippage increases so that $S + L > L_B$, the steady-state behavior in the leading edge disappears. Fig-

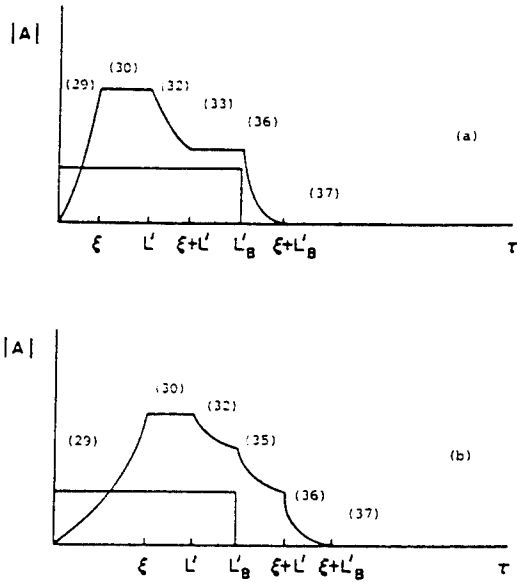


FIG. 4. Schematic plots of the optical field amplitude as a function of τ , in the case $x_0=0$, $A_0=0$, and $L < L_B$. The amplitude is viewed at positions $S < L$ (or $\xi < L'$) and for (a) $S + L < L_B$ (or $\xi + L' < L'_B$), (b) $S + L > L_B$.

ure 5 shows similar plots except that now $L < S < L_B$ (or $L' < \xi < L'_B$), and therefore a superradiant region replaces the steady-state region at the trailing edge. Figure 6 shows the case $L_B < S$ (or $L'_B < \xi$), which corresponds to the short-pulse limit.

Note an interesting new feature in each of the Figs. (4)–(6): there exists a region that is a combination of the steady-state and superradiant solutions occurring at the leading edge of the optical pulse. The physical explanation for the occurrence of this “semi-superradiant” region is as follows. In this region, the steady-state part of the radiation field is generated by the standard FEL mechanism from the noise sources A_0 and x_0 . However,

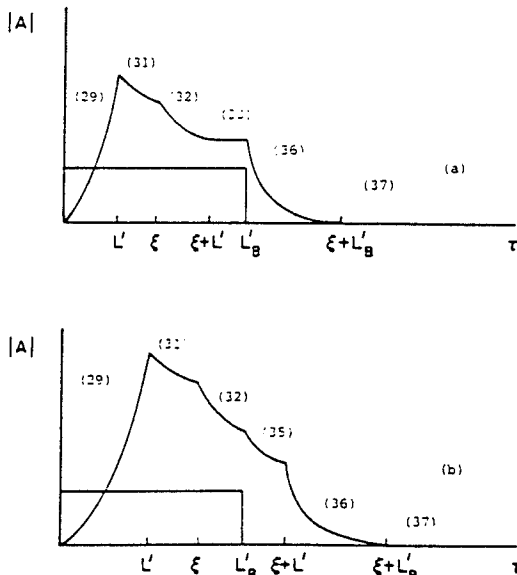


FIG. 5. Schematic plots of the optical field amplitude at positions $L < S < L_B$ (or $L' < \xi < L'_B$) as a function of τ , in the case $x_0=0$, $A_0=0$, and $L < L_B$. (a) is for $S + L < L_B$ (or $\xi + L' < L'_B$) and (b) is for $S + L > L_B$ (or $\xi + L' > L'_B$).

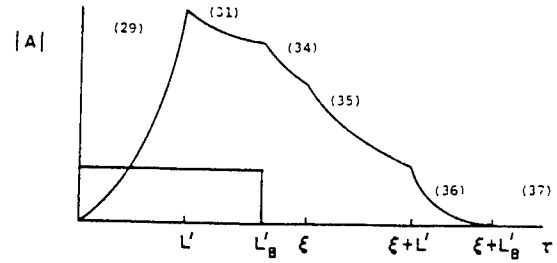


FIG. 6. Schematic plot of the optical field amplitude at positions $S > L_B$ as a function of τ when $x_0=0$, $A_0=0$, and $L < L_B$.

as the electrons in front of the initial optical pulse slip into the pulse, they experience rapidly varying external fields and emit spontaneous radiation which contributes to superradiance, the magnitude of which depends on A_0 . However, after this region slips over the entire electron pulse, the growth of the superradiant component is stopped, with the consequence that the radiation amplitude in the leading edge is usually smaller than that at the trailing edge.

V. SUMMARY

In this paper, we have given a linear theory of superradiance for a free-electron laser in the high-gain Compton regime. One of the aims of this paper has been to describe the leading as well as the trailing edges of the optical pulse, and to fix correctly the boundary conditions at the edges of the electron pulse. We caution that computational methods that do not correctly incorporate these boundary conditions may produce spurious behavior in the radiation field dynamics.

When the FEL evolves from the initial conditions of zero initial optical field, which is the case considered in Ref. 1, we show that the evolution of the radiation pulse proceeds in qualitatively different ways in the three cases $S < L_B$, $S = L_B$, and $S > L_B$. We then extend the calculation of Ref. 1 to allow for the presence of an initial optical pulse of length L , which may be greater or smaller than L_B . Whereas superradiance is a persistent feature of the radiation field at the trailing edge of the electron beam, we find that it can also occur at the leading edge of the optical pulse when $L < L_B$.

The one-dimensional linear theory presented here is a first step, but leaves several interesting questions unanswered. The nonlinear evolution of superradiance is a subject of considerable interest. Though superradiance and sidebands differ in their growth rates, numerical simulations seem to suggest that they are essentially indistinguishable in their nonlinear states. This feature deserves closer scrutiny. We also note that the optical “spikes” seen in numerical simulations are sufficiently singular that the “slowly varying” approximation routinely used for the radiation field in a high-gain FEL is open to question.

ACKNOWLEDGMENTS

This work is supported by the U.S. Office of Naval Research, Grant No. N0014-79C-0769 and the National Science Foundation, Grant Nos. ECS-87-13710 and ECS-89-12581.

- ¹R. Bonifacio, C. Maroli, and N. Piovella, *Opt. Commun.* **68**, 369 (1988).
- ²See, for instance, A. Yariv, *Quantum Electronics*, 3rd ed. (Wiley, New York, 1989), pp. 352–355.
- ³R. Bonifacio and F. Casagrande, *Nucl. Instrum. Methods A* **239**, 36 (1985).
- ⁴R. Bonifacio, B. W. J. McNeil, and P. Pierini, *Phys. Rev. A* **40**, 4467 (1989).
- ⁵W. M. Sharp, W. M. Fawley, S. S. Yu, A. M. Sessler, R. Bonifacio, and L. de Salvo Souza, *Nucl. Instrum. Methods A* **285**, 217 (1989).
- ⁶J. Cao and A. Bhattacharjee, *11th International Conference on Free Electron Lasers, 1989, Advance Program* (IEEE Lasers and Electro Optics Society, Naples, 1989), p. 11.
- ⁷N. M. Kroll, P. L. Morton, and M. N. Rosenbluth, *IEEE J. Quantum Electron.* **QE-17**, 1436 (1981).
- ⁸I. Gjaja and A. Bhattacharjee, *Opt. Commun.* **58**, 201 (1985); **62**, 39 (1987).

Ginzburg-Landau equation: A nonlinear model for the radiation field of a free-electron laser

S. Y. Cai and A. Bhattacharjee

Department of Applied Physics, Columbia University, New York, New York 10027

(Received 15 February 1990; revised manuscript received 31 January 1991)

It is shown that the nonlinear dynamics of the radiation field in a free-electron laser can be modeled by the Ginzburg-Landau equation. The refractive index of the electron beam in the nonlinear regime and the saturation intensity of the radiation field are obtained from WKB theory. Although the Ginzburg-Landau equation does not permit soliton solutions, it is shown that certain types of solitary-wave solutions have a strong resemblance to spikes observed in simulations and experiments.

Free-electron-laser (FEL) theory has been very successful in describing FEL operation in the linear regime, and various predictions of linear theory have been shown to be in good agreement with experiments.¹ However, in the regime of saturated growth, which is strongly influenced by nonlinear effects, FEL physics has been studied largely in connection with specific problems such as efficiency enhancement techniques² and trapped-particle phenomena. The latter includes the important sideband instability,³ which is a consequence of the synchrotron oscillation of the electrons trapped in potential wells of the electron bunches, together with the finite slippage of the optical wave with respect to the moving electrons. A basic understanding of these nonlinear effects has been developed through analytical studies in idealized models. While these analyses provide qualitative results and insights for specific problems, the burden of a general nonlinear description has rested on computer simulations, which have played a very important role both in the design of FEL's and the interpretation of experiments.

This paper is motivated in part by an interesting and somewhat less studied phenomenon called "spiking," which has been observed in computer simulations and more recently, in experiments carried out by the Warren, Goldstein, and Newnam,⁴ Dodd and Marshall,⁵ and Richman, Madey, and Szarmes.⁶ "Spikes" generally occur in the high-power, saturated-signal regime, and are narrow, high-intensity radiation pulses that are generated spontaneously. A qualitative physical mechanism has been outlined by Warren and co-workers, who attribute the generation of spikes to the growth of sidebands.⁴

In this paper, we propose a simple, yet fairly general, model for the nonlinear evolution of the radiation field in a FEL. This model enables us to understand the spatial and temporal structure of the radiation field in the nonlinear regime. Preliminary results of this work were presented elsewhere.⁷ We show that the radiation field obeys approximately the Ginzburg-Landau equation (GLE),

$$i \frac{\partial A}{\partial z'} - \frac{\alpha}{2} \frac{\partial^2 A}{\partial t'^2} + \lambda_0 A + \beta |A|^2 A = 0, \quad (1)$$

where A is the amplitude of the radiation field, $z' = z$ is

the distance along the undulator axis, $t' = t - z/v_g$ is the retarded time for a radiation pulse propagating with group velocity v_g , and α , β , and λ_0 are complex constants to be given later. The appearance of the GLE in a model of FEL nonlinear dynamics is less surprising than may appear at first glance. After all, there exists a useful analogy between an optical fiber and an electron beam,⁸ and in certain types of dielectric fibers, it is known that the radiation field obeys a nonlinear Schrödinger equation,⁹ which is nothing but a special case of the GLE. In order to strengthen further the analogy between an electron beam and a fiber, we derive an approximate expression for the refractive index of the electron beam in the nonlinear regime from a WKB theory. This is one of the important results of the present theory.

The GLE is a nonintegrable partial differential equation, and does not have soliton solutions. We are, therefore, led to the conclusion that it is not possible to generate optical solitons spontaneously from FEL dynamics. We note that solitons can still be created in principle, as they are in conventional lasers, by propagating the radiation output from a FEL through a dielectric fiber,¹⁰ but this is not the subject of the present paper.

Though the GLE does not admit soliton solutions, it has solitary-wave solutions,¹¹ which can be obtained by sophisticated variants of the Painlevé analysis.^{12,13} We show that a class of these solutions exhibits "spiking" behavior with characteristic widths that appear to be in fairly good agreement with experimental measurements⁴⁻⁶ and numerical solutions.

We begin our analysis with the well-known one-dimensional equations for a Compton FEL:^{2,14}

$$\frac{d\gamma_j}{dz} = - \frac{k_s a_s a_w}{\gamma_j} \sin(\psi_j + \phi), \quad (2a)$$

$$\frac{d\psi_j}{dz} = k_w \left[1 - \frac{\gamma_r^2}{\gamma_j^2} \right] + \frac{k_s a_w a_s}{\gamma_j^2} \cos(\psi_j + \phi), \quad (2b)$$

$$\frac{du}{dz} = i \frac{a_w \omega_p^2}{2k_s c^2} \left\langle \frac{\exp(-i\psi)}{\gamma} \right\rangle, \quad (2c)$$

where z is the direction of propagation of the electron and optical beams and also coincides with the undulator

axis, $\psi_j + \phi$ is the relative phase of the electron (of rest mass m) with respect to the radiation field, and $\gamma_j mc^2$ is its energy; the vector potential $\mathbf{A} = \mathbf{A}_w + \mathbf{A}_s$, $a_w = eA_w/mc^2$, $a_s = eA_s/mc^2$; k_w , $k_s = \omega/c$ are the wave numbers of the undulator and radiation fields, respectively; ω is the carrier frequency, $u = a_s \exp(i\phi)$ is the complex amplitude of the radiation field, and $\gamma_r = [k_s(1 + a_w^2)/2k_w]^{1/2}$ is the resonant energy. It has been shown in Ref. 15 that Eqs. (2) can be modeled by an approximate reduced set of equations that involve only the collective variables $x \equiv \langle \exp[-i(\psi_j - \psi_r)] \rangle$, $y \equiv \langle [(\gamma_j - \gamma_0)/\gamma_0] \exp[-i(\psi_j - \psi_r)] \rangle$, and $A \equiv u \exp(i\psi_r)$, where ψ_r is defined by the relation $d\psi_r/dz = k_w(1 - \gamma_r^2/\gamma_0^2)$, and γ_0 is the energy of the initially monoenergetic electron beam. In our notation, these reduced equations can be written as

$$\frac{dA}{dz} = i\delta A + igx, \quad (3a)$$

$$\frac{dx}{dz} = -ihy, \quad (3b)$$

$$\begin{aligned} \frac{dy}{dz} = & ifA - 2ihy_0(y - xy_0) \\ & + 2i\delta xy_0 - 2if(x^*A + A^*x)x, \end{aligned} \quad (3c)$$

where $\delta \equiv k_w(1 - \gamma_r^2/\gamma_0^2)$, $f \equiv k_s a_w/(2\gamma_0^2)$, $g \equiv \omega_p^2 a_w/(2k_s \gamma_0 c^2)$, $h \equiv k_s(1 + a_w^2)/\gamma_0^2$ are parameters, and $y_0 \equiv \langle (\gamma_j - \gamma_0)/\gamma_0 \rangle$. For a detailed derivation of Eqs. (3), the reader is referred to Ref. 15. We note that Eqs. (3) admit an energy conservation law, given explicitly by $y_0 + (f/g)(|A|^2 - |a_0|^2) = 0$, where $a_0 = A(z=0)$ is the initial amplitude of the radiation field and is usually small compared with A in the saturated regime.

Equations (3a) and (3b) can be rewritten, respectively, as $x = (\dot{A} - i\delta A)/(ig)$ and $y = i\dot{x}/h = (\dot{A} - i\delta A)/(gh)$, where the overdot denotes d/dz . Substituting expressions for x and y in Eq. (3c), we obtain a third-order differential equation for A :

$$\begin{aligned} \ddot{A} - (i\delta - 2i\epsilon hy_0)\dot{A} + 2\epsilon hy_0(2\delta - \epsilon hy_0)A \\ + \frac{2\epsilon fh}{ig}(\dot{A}A^* - \dot{A}^*A)(\dot{A} - i\delta A) \\ - ifghA + 2i\epsilon y_0\delta(\epsilon hy_0 - \delta)A = 0, \end{aligned} \quad (4)$$

in which we have introduced a small parameter ϵ to tag all terms containing y_0 , which is a small quantity for most FEL's. We will eventually set ϵ to unity.

Equation (4) can be solved by a WKB method. We write $A = A_0 \exp[(\sum_{n=0}^{\infty} \epsilon^n S_n)]$, where A_0 is a constant and $S_n = S_n(z)$ are slowly varying functions of z . We assume that $\dot{S}_n = \epsilon \dot{S}_n$ ($n=0, 1, 2, \dots$) and $\ddot{S}_0 = \epsilon^2 \ddot{S}_0$. Using the conservation relation $y_0 + (f/g)(|A|^2 - |a_0|^2) = 0$ and the assumption $|A| \gg |a_0|$, we can then solve Eq. (5) by equating coefficients of ϵ^n . To $O(\epsilon^0)$, we obtain

$$\dot{S}_0^3 - i\delta \dot{S}_0^2 - ifgh = 0, \quad (5)$$

which reduces to the well-known linear cubic eigenvalue equation¹⁶ $\lambda_0^3 - \delta \lambda_0^2 + fgh = 0$ if we set $\dot{S}_0 = i\lambda_0$. To $O(\epsilon)$, Eq. (4) gives

$$\ddot{S}_1 + (3\dot{S}_0 - i\delta)\dot{S}_1 + (3\dot{S}_0^2 - 2i\delta\dot{S}_0)\dot{S}_1 = Qy_0, \quad (6)$$

where $Q \equiv -\dot{S}_0^2 + 2i\delta\dot{S}_0 - (\dot{S}_0 - \dot{S}_0^*)\dot{S}_0 + i\delta(\dot{S}_0 - \dot{S}_0^*) + \delta^2$. We now transform from z to y_0 as the new independent variable by writing $d/dz = (d|A|^2/dz)(d/d|A|^2)$, whereupon using the WKB representation and the energy conservation relation we obtain $d/dz \simeq (\dot{S}_0 + \dot{S}_0^*)y_0(d/dy_0)$ and $d^2/dz^2 \simeq (\dot{S}_0 + \dot{S}_0^*)^2 y_0(d/dy_0)$ to the lowest order in ϵ . Equation (6) then reduces to

$$ay_0 \frac{d\dot{S}_1}{dy_0} + b\dot{S}_1 = Qy_0, \quad (7)$$

where $a \equiv (\dot{S}_0 + \dot{S}_0^*)(4\dot{S}_0 + \dot{S}_0^* - i\delta)$ and $b \equiv 3\dot{S}_0^2 - 2i\delta\dot{S}_0$. Equation (7) can be integrated with the initial condition $\dot{S}_1 = 0$ when $y_0 = 0$ (the linear regime). The solution is $\dot{S}_1 = [Q/(a+b)]y_0$. To $O(y_0)$, we thus obtain the index of refraction of the electron beam in the nonlinear regime, $n = 1 + (\dot{S}_0 + \dot{S}_1)/ik_s \equiv 1 + \lambda/\lambda_s$, where $\lambda = \lambda_0 + \beta|A|^2$, and

$$\beta = -\frac{2fh}{g} \frac{(\lambda_0 - \delta)(\lambda_0 + 2\text{Re}\lambda_0 - \delta)}{2\text{Im}\lambda_0[2\text{Im}\lambda_0 - i(3\lambda_0 - \delta)] - 3\lambda_0^2 + 2\delta\lambda_0}. \quad (8)$$

We remark that the quadratic dependence of n on $|A|$ means that in the saturation regime, even when gain is negligible, refractive optical guiding can, in principle, aid the confinement of radiation in a FEL. This effect has been observed in numerical simulations,^{7,17} but remains to be verified experimentally.¹⁸

In Fig. 1, we compare the numerical results obtained by integrating the original FEL equations (2) with those obtained from the reduced equations (3) for a typical set of parameters. On the same plot, we show $A(z) = A_0 \exp(i\lambda z)$ obtained from the WKB analysis.

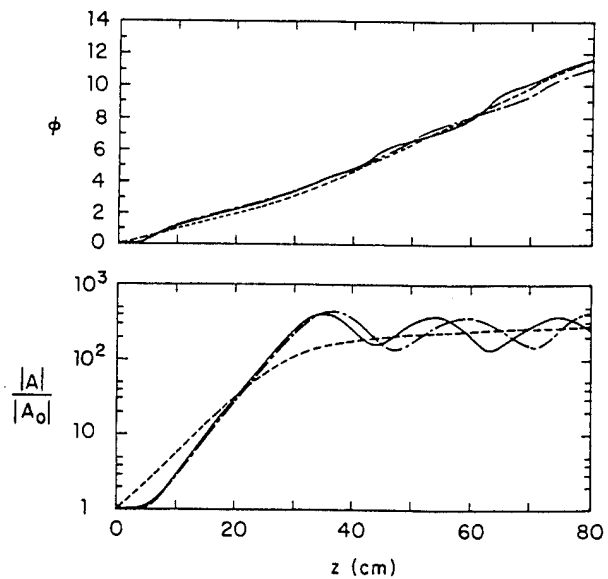


FIG. 1. Comparison of $|A|$ and ϕ calculated from the original equations (2) (solid lines), reduced equations (3) (dashed-dotted lines), and WKB analysis (dotted lines).

Whereas the analytical solution is remarkably good in predicting the phase shift, the prediction for $|A|$ is less accurate. In particular, the analysis predicts the approximate average saturation level for $|A|$, but cannot reproduce the oscillations caused by synchrotron motion. [The average intensity of the saturated radiation field can be estimated by simply setting $\text{Im}(n)=0$, and is given by $|A|^2 = -\text{Im}\lambda_0/\text{Im}\beta$.] In order to account for the oscillations at saturation, higher-order WKB calculations are needed. Note, however, that neglect of these higher-order terms in the nonlinear analysis for $|A|$ does not mean that the physics of synchrotron oscillations has been eliminated altogether. These oscillations are implicitly contained in the electron dynamical equations that involve Eqs. (3b) and (3c).

We have considered so far the single-frequency FEL equations. In the presence of multiple frequencies, it is extremely difficult to obtain a description of FEL dynamics in terms of a reduced set of equations involving collective variables. Instead, we exploit the analogy between the electron beam and an optical fiber to obtain heuristically an equation for the radiation field. We consider an optical signal of the form $\mathcal{A}(z, t) = A(z, t)\exp(ikz - i\omega_0 t)$, where $k_0 = \omega_0/c$, and $A(z, t)$ is a slowly varying amplitude. Note that by including the time dependence in the amplitude $A(z, t)$, we have allowed for the excitation of multiple modes. At a given point $z = z_0$, the Fourier transformation of this signal is defined by the relation

$$\tilde{\mathcal{A}}(z_0, \Delta\omega) = \frac{1}{\sqrt{2\pi}} \int_{-\infty}^{+\infty} dt' \exp(ik_0 z_0 + i\Delta\omega t') A(z_0, t'), \quad (9)$$

where $\Delta\omega = \omega - \omega_0$. Each frequency component is advanced along z according to the relation

$$\tilde{\mathcal{A}}(z_0 + dz, \Delta\omega) = \tilde{\mathcal{A}}(z_0, \Delta\omega) \exp\{i[\omega/c + \lambda(\omega)]dz\}.$$

The inverse Fourier transform of $\mathcal{A}(z_0 + dz, \Delta\omega)$ in the limit $dz \rightarrow 0$ then gives

$$\begin{aligned} \frac{\partial A(z, t)}{\partial z} &= \frac{i}{2\pi} \int_{-\infty}^{+\infty} d\Delta\omega \int_{-\infty}^{+\infty} dt' A(z, t') \\ &\quad \times \exp[i\Delta\omega(t' - t)] \\ &\quad \times \left[\frac{\Delta\omega}{c} + \lambda(\omega) \right]. \end{aligned} \quad (10)$$

For a FEL, $\lambda(\omega)$ usually has a narrow bandwidth around the maximum linear gain frequency ω_0 . We can, therefore, expand $\lambda(\omega)$ in a Taylor series around ω_0 , and write

$$\begin{aligned} \frac{\Delta\omega}{c} + \lambda(\omega) &\approx \lambda_0(\omega_0) + \beta|A|^2 + v_g^{-1}\Delta\omega \\ &\quad + \frac{1}{2}(\alpha_1 + i\alpha_2)\Delta\omega^2 + \dots, \end{aligned} \quad (11)$$

where $v_g = c/(1 + c\partial\lambda/\partial\omega)$ is the group velocity of the signal, $\alpha_1 + i\alpha_2 = \partial^2\lambda_0/\partial\omega^2|_{\omega=\omega_0}$, α_1 is the group velocity dispersion and α_2 is the gain dispersion, and β is the complex coefficient defined by Eq. (8). Substituting Eq. (11) in

(10) yields

$$\frac{\partial A}{\partial z} = i\lambda_0(\omega_0)A - v_g^{-1} \frac{\partial A}{\partial t} - \frac{i(\alpha_1 + i\alpha_2)}{2} \frac{\partial^2 A}{\partial t^2} + i\beta|A|^2 A, \quad (12)$$

which can be reduced to the GLE (1) by transforming to variables $z' = z$, $t' = t - z/v_g$, $\alpha \equiv \alpha_1 + i\alpha_2$.

The GLE (1), with complex coefficients, is not integrable in general.¹² This rules out the possibility of spontaneous soliton formation during the nonlinear evolution of a FEL. However, special solitary wave solutions can be constructed following the methods described in Refs. 11 and 12. These solutions are

$$A(z', t') = \frac{q \exp(-i\Omega z')}{[\exp(Kt') + \exp(-Kt')]^{1+i\sigma}}, \quad (13)$$

where $\lambda_0 = \zeta - i\chi$, $\beta = \beta_r + i\beta_i$,

$$|q|^2 = \frac{8\chi(\alpha_1 + i\alpha_2)(1+i\sigma)(2+i\sigma)}{\beta[\alpha_2(1-\sigma^2) + 2\sigma\alpha_1]}, \quad (14a)$$

$$\Omega = \frac{\chi[\alpha_1(1-\sigma^2) - 2\sigma\alpha_2]}{\alpha_2(1-\sigma^2) + 2\sigma\alpha_1} + \zeta, \quad (14b)$$

$$K = \left[\frac{2\chi}{\alpha_2(\sigma^2 - 1) - 2\alpha_1\sigma} \right]^{1/2}, \quad (14c)$$

and σ satisfies the quadratic equation

$$\sigma^2 - 3 \frac{\alpha_1\beta_r + \alpha_2\beta_i}{\alpha_2\beta_r - \alpha_1\beta_i} \sigma - 2 = 0. \quad (15)$$

Equation (15) has two real roots, and produces two families of solitary-wave solutions. In order to obtain simple analytical formulas for these solutions, we make certain approximations. First, we note that for a FEL operating near the maximum linear gain frequency ω_0 , $\text{Re}(n)$ is approximately a linear function of ω .¹⁷ Therefore, we set $\alpha_1 \approx 0$ in Eq. (15), which reduces to $\sigma^2 - 3(\beta_i/\beta_r)\sigma - 2 \approx 0$. For the case $|\beta_i| > |\beta_r|$, which is satisfied by the parameters of the FEL's considered here, the two roots obey the inequalities $\sigma_1^2 \gg 1$ and $\sigma_2^2 \ll 1$. When $\sigma^2 = \sigma_1^2 \gg 1$, $K_1 \approx [2\chi/(\alpha_2\sigma_1^2)]^{1/2}$ is real, and Eq. (13) gives

$$|A|^2 = \frac{|q|^2}{4 \cosh^2(K_1 t')}. \quad (16)$$

The solution (16) for $|A|^2$ has a single peak at $t' = 0$ ($z = v_g t$) with the half-width $\Delta t_1 \approx K_1^{-1}$. In the case $\sigma = \sigma_2$, $K_2 \approx i\sqrt{2\chi}/\alpha_2$, and Eq. (13) gives

$$|A|^2 = \frac{|q|^2}{4 \cos^2(K_2 t')}. \quad (17)$$

The solution (17) exhibits periodic, finite-time singularities, as shown in Fig. 2. The width of each peak is given by $\Delta t_2 \approx K_2^{-1}$, and the separation between neighboring peaks is $\Delta T \approx \pi K_2^{-1}$. Clearly, at the singularities, our model breaks down, and higher-order terms in the expansion of $\lambda(\omega)$ become significant.

We now show that the frequency of the periodic solution (17) has the same parametric dependence and is of the same order of magnitude as the amplitude oscillation frequency expected from sideband theory.³ To see this, we note that the frequency of solution (17) is $\Delta\omega = \sqrt{-2\chi/\alpha_2}$. Since at saturation $|A| = \sqrt{\chi/\text{Im}\beta}$, we write $\Delta\omega = [(-2a_s/\alpha_2)\sqrt{\chi/\text{Im}\beta}]^{1/2}$. From the cubic equation $\lambda_0^3 - \delta\lambda_0^2 + fgh = 0$, assuming $\delta \approx 0$, we obtain $\lambda_0^3 \approx -fgh$, which gives $\zeta = -\frac{1}{2}(fgh)^{1/3}$ and $\chi = (\sqrt{3}/2)(fgh)^{1/3}$. Also, from the cubic equation, it follows by straightforward algebra that $\alpha_2 \equiv \text{Im}(\partial^2\lambda_0/\partial\omega^2) \approx [-\sqrt{3}/(36\omega^2)][h^2/(fgh)^{1/3}]$. From Eq. (8), we get $\text{Im}\beta \approx (36\sqrt{3}/241)(fh/g)$. Using these expressions for α_2 , χ , and $\text{Im}\beta$, we then obtain

$$\Delta\omega \approx 0.9 \left[2\omega \left[\frac{a_s a_w}{1 + a_w^2} \right]^{1/2} \right]. \quad (18)$$

The expression in parentheses on the right-hand side of Eq. (18) is the same as the frequency separation of a sideband from the carrier signal predicted by standard sideband theory.³ We also note that solutions resembling the solitary-wave solutions can be generated by the time-dependent FEL equations, which include the effect of slippage. We have used our computer code¹⁹ to carry out simulations of the experiment in Ref. 5. The simulation shows "spikes" of width $\Delta t \approx 25$ psec separated by periods of 80 psec. [See Fig. 3(a) of Ref. 5.] For the FEL described in Ref. 5, we calculate numerically the parameters $\chi = 0.11 \text{ cm}^{-1}$ and $\alpha_2 = 5.3 \times 10^{-21} \text{ sec}^2/\text{cm}$. The analytical solutions (17) then predict periodic spikes of width $\Delta t_2 \approx 154$ psec. The experimentally measured width ~ 150 psec.

We now compare the analytical solutions with results from the experiment of Ref. 4, for which $\lambda_w = 2.7 \text{ cm}$, $a_w = 0.8$, $\lambda_s = 9.85 \text{ }\mu\text{m}$, $I = 39.3 \text{ A}$, $r_b = 0.1 \text{ cm}$, and $\gamma_0 = 42.7$. From the linear cubic equation (5), we find $\chi = 0.018 \text{ cm}^{-1}$ and $\alpha_2 = 2.0 \times 10^{-27} \text{ sec}^2/\text{cm}$; then Eq. (17) gives $\Delta t_2 \approx 0.24$ psec. The experimentally observed width is 0.2 psec.⁴

Finally, in the FEL experiment in Ref. 6, the pulse separation (not width) is measured by an autocorrelation technique and is confirmed by numerical simulations. By using the parameters given in Ref. 6 (except that the energy spread is taken to be zero and the electron-beam radius to be 0.02 cm) in the cubic equation, we get $\chi = 0.026 \text{ cm}^{-1}$, $\alpha_2 = 1.24 \times 10^{-24} \text{ sec}^2/\text{cm}$. The theoretically predicted pulse separation for the solution (17) is $\Delta T \approx 0.22$ psec. The experimentally measured separation

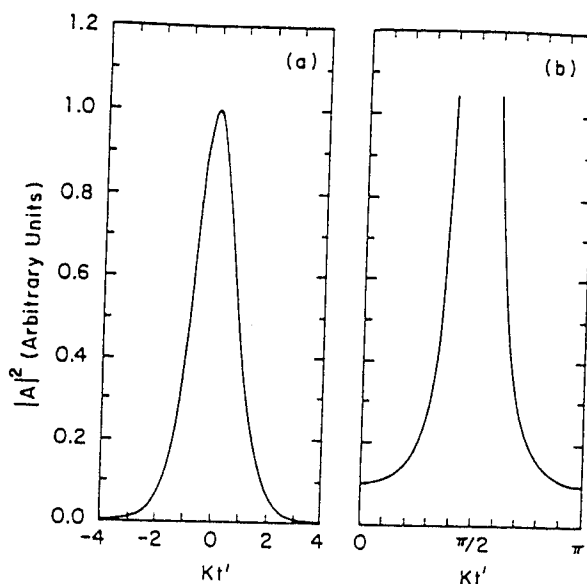


FIG. 2. Solitary-wave solutions of the Ginzburg-Landau equation. Solution (16) is plotted in (a) and solution (17) in (b).

is 0.8 psec.

We emphasize that our model is rather simple, and the remarkable accord with experimental results (from Refs. 4 and 5) should therefore be taken with a grain of salt. However, we believe that the essential idea of spikes as a form of solitary wave propagating in the "fiber," that is, the electron beam, is qualitatively supported by experimental results.

In comparing theory with experiments, we have so far used the singular, periodic solution (17). The solution (16), which is nonsingular but aperiodic, also predicts spike widths that are of the same order as those obtained from (17). Clearly, initial and boundary conditions, as well as issues of stability, will determine the dominance of particular solitary-wave solutions in a given experiment.

Note added in proof. After the completion of this work, we found that for a small-gain oscillator, a Ginzburg-Landau equation (of rather different form than has been presented in this paper) has been given by Colson and Ride.²⁰

We are deeply indebted to Professor T. C. Marshall for many stimulating discussions, and to Mr. J. Cao for his involvement and interest. This work is supported by the Office of Naval Research, Grant No. N0014-89-J-1652 and the National Science Foundation, Grant No. ECS-89-122581.

¹See, for instance, T. C. Marshall, *Free Electron Lasers* (MacMillan, New York, 1985), and the recent review paper by C. W. Roberson and P. Sprangle, *Phys. Fluids B* 1, 3 (1989).

²N. M. Kroll, P. L. Morton, and M. N. Rosenbluth, *IEEE J. Quantum Electron.* QE-17, 1436 (1981); A. T. Lin and J. M. Dawson, *Phys. Rev. Lett.* 42, 1670 (1979); P. Sprangle, C.-M. Tang, and W. M. Mannheimer, *ibid.* 43, 1932 (1979).

³N. M. Kroll and M. N. Rosenbluth, in *Physics of Quantum Electronics* (Addison-Wesley, Reading, MA, 1980), Vol. 7, p. 147.

⁴R. W. Warren, J. C. Goldstein, and B. E. Newnam, *Nucl. Instrum. Methods Phys. Res. A* 250, 104 (1986).

⁵J. W. Dodd and T. C. Marshall, *IEEE Trans. Plasma Sci.* 18, 447 (1990).

⁶B. A. Richman, J. M. J. Madey, and E. Szarmes, *Phys. Rev. Lett.* 63, 1182 (1989).

⁷A. Bhattacharjee, J. Cao, and S. Y. Cai, in *Proceedings of the International Conference on Free Electron Lasers*, 1989, Naples, Florida (IEEE Lasers and Electro Optics Society, Naples, 1989), p. 35; see also J. Cao, A. Bhattacharjee, and S. Y.

- Cai, Bull. Am. Phys. Soc. **34**, 1983 (1989).
- ⁸E. T. Scharlemann, A. M. Sessler, and J. S. Wurtele, Phys. Rev. Lett. **54**, 1925 (1985).
- ⁹See, for instance, A. E. Siegman, *Lasers* (University Science, Mill Valley, CA, 1986), p. 395.
- ¹⁰A. Hasegawa and F. Tappert, Appl. Phys. Lett. **23**, 142 (1973); **23**, 171 (1973).
- ¹¹Here, the term "soliton" describes "a pulselike nonlinear wave (solitary wave) which emerges from a collision with a similar pulse having unchanged shape and speed" [A. C. Scott, F. Y. F. Chu, and D. W. McLaughlin, Proc. IEEE **61**, 1443 (1973)].
- ¹²F. Cariello and M. Tabor, Physica D **39**, 77 (1985).
- ¹³N. Bekki and I. Nozaki, Phys. Lett. **110**, 133 (1985).
- ¹⁴I. Gjaja and A. Bhattacharjee, Opt. Commun. **58**, 201 (1986); **62**, 39 (1987), and references cited therein.
- ¹⁵R. Bonifacio, F. Casagrande, and L. De Salvo Souza, Phys. Rev. A **33**, 2836 (1986).
- ¹⁶R. Bonifacio, C. Pellegrini, and L. M. Narducci, Opt. Commun. **50**, 373 (1984).
- ¹⁷S. Y. Cai, A. Bhattacharjee, and T. C. Marshall, IEEE J. Quantum Electron. QE-**23**, 1651 (1987).
- ¹⁸A. Bhattacharjee, S. Y. Cai, S. P. Chang, J. W. Dodd, A. Fruchtman, and T. C. Marshall, Phys. Rev. A **40**, 5081 (1989).
- ¹⁹S. Y. Cai, A. Bhattacharjee, S. P. Chang, J. W. Dodd, and T. C. Marshall, Phys. Rev. A **40**, 3127 (1989).
- ²⁰W. B. Colson and S. K. Ride, in *Physics of Quantum Electronics* (Ref. 3), Vol. 7, p. 377.

“Spiking” Radiation in the Columbia Free Electron Laser

JAMES W. DODD, STUDENT MEMBER, IEEE, AND T. C. MARSHALL

Abstract—We report the observation of “spikes” of high-intensity radiation emitted from a 2-mm wavelength Raman free electron laser (FEL) oscillator. The spikes are correlated with a well-developed sideband spectrum, including several sideband harmonics, together with the carrier. A pulse width ~ 150 ps is obtained from analysis of data obtained with a two-slit “Young’s experiment.” An even shorter pulsewidth results from a numerical model. Using an elementary model of the spike, we estimate that the peak spike pulse power is ~ 100 MW.

I. INTRODUCTION

SPIKES, which are narrow, high-intensity radiation pulses, are believed to be a feature of free electron laser (FEL) operation at high power with substantial sideband production. They have been identified as a feature in numerical simulations by Colson and Freedman [1], [2] and Quimby [3] and have been studied numerically and experimentally by the FEL group at Los Alamos [4]. A physical model of the evolution of the spike has been outlined by Warren *et al.* [4]; beginning with a carrier accompanied by sidebands (frequency modulation), this wave can develop amplitude modulation (pulse formation) by an energetically favored interaction between the fm wave and electrons. An electron originally in resonance with the carrier loses energy to the wave and drops into resonance with the low-frequency sideband. This causes the low-frequency sideband to grow, and the wave develops amplitude modulation which, in the nonlinear limit, causes a “spike.”

Further study by numerical simulation has shown [4] that the energy radiated in a spike is drawn from the energy of electrons in the slippage distance $N\lambda$, and involves an interaction time of about half a synchrotron period in the strong field of the spike. The spiking can become chaotic.

In this paper we show first, numerically, that it is possible to form spikes in our Raman FEL that have a duration ~ 100 ps. The remainder reports experimental data from which we infer the existence of such short high-intensity pulses.

II. BACKGROUND OF THE EXPERIMENT

The Columbia FEL is a millimeter-wavelength device which produces several MW of power in single pulses that last ~ 100 ns [5]. The operating parameters of the device are listed in Table I. For this research the FEL is operated as an oscillator with one output mirror serving as an etalon. The carrier wavelength of 1.95 mm is accompanied by sidebands as well as longer wavelength sideband harmonics. The long-wavelength sideband harmonics have been studied analytically and numerically by Riyopoulos and Tang [6]; we have studied such sidebands numerically [5], and more recently we have found that the long-wavelength sideband harmonics appear as well.

Experimentally, we observe the FEL spectrum using a grating spectrometer. The sidebands can be prominent features of the FEL spectrum. In Fig. 1(a) we show a well-developed sideband spectrum consisting of the carrier at 1.95 mm, an upper and lower sideband, and two “harmonics” of the long-wavelength sideband. The different sideband frequencies are not mathematically harmonics, nor is it expected that they should be related in that way. In Fig. 1(b) we show the simulated spectrum; the primary sidebands are indicated by arrows. The long-wavelength “harmonic” spectrum is complicated and does not correspond to the experimentally observed peaks, although it is situated in the correct band of wavelengths; but the primary sidebands are in the correct location, consistent with the laser power. Although we have found from numerical studies [7] that it is the TE_{11} mode which is excited by the FEL interaction, the high-power operation may introduce some beam asymmetry which could excite higher order waveguide modes that would complicate the interpretation of this spectrum. The experimental spectrum is not corrected for the response characteristic of the detector: The data at the longest wavelengths should be multiplied by a factor ~ 0.4 to account for the increasing sensitivity of the detector at long wavelengths.

Having observed strong sidebands in the Columbia FEL [8], it is not surprising that we find spikes as well. The spike is found in a resonator configuration where substantial power is developed. The spikes may appear randomly or individually or occasionally as a set of “mode-locked” pulses spaced by the bounce time of radiation in the resonator. An example is shown in Fig. 2. However, not all shots produce spikes, and when they occur, they are superimposed on the “background” level of FEL radiation.

Manuscript received July 17, 1989; revised December 22, 1989. This work was supported by the Office of Naval Research by Grant N00014-89-J-1652.

The authors are with the Department of Applied Physics, Columbia University, New York, NY 10027.

IEEE Log Number 9035363.

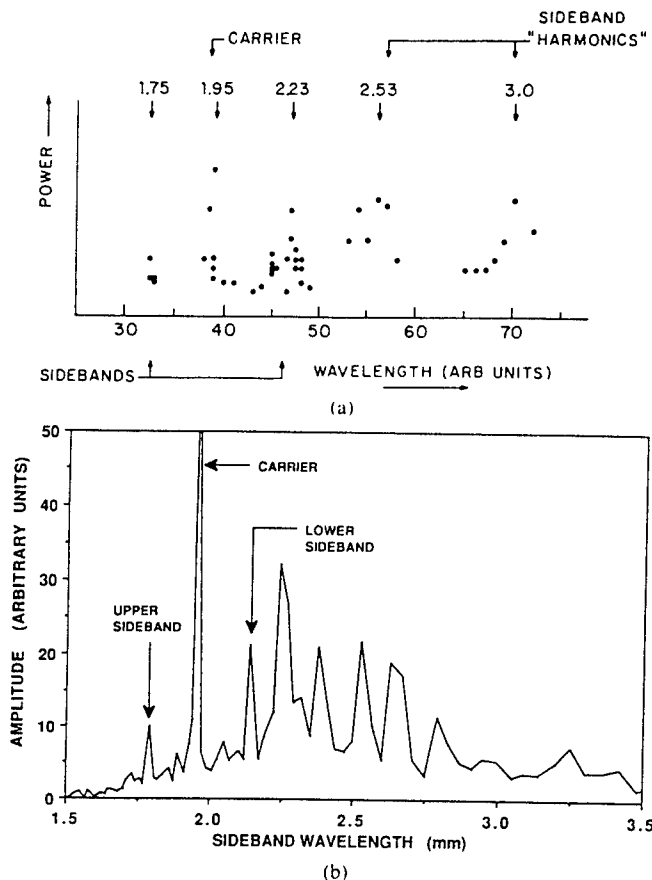


Fig. 1. (a) The spectrum of sideband radiation in the FEL oscillator. Gaps in the data-point ensemble correspond to the very low power recorded. (b) The numerically generated sideband spectrum using a multifrequency code (courtesy of S. Y. Cai) and using the numerical method outlined in reference [5].

TABLE I
FEL OPERATING CONDITIONS

Undulator period (helical)	1.7 cm
Undulator length	70 cm
Electron beam energy	800 kV
Electron beam current	120 A
Electron beam current density	$\sim 1 \text{ kA/cm}^2$
Electron beam diameter	4 mm
Electron beam pulse length	150 ns
Waveguide diameter	18 mm
Guiding field strength	9.5 kG
Wiggler strength, $\gamma v_{\perp} / v = a_u$	0.28
FEL wavelength	2 mm
Synchrotron period (typical operation)	$\sim 20 \text{ cm}$
Power output	several MW
Configuration	oscillator

A puzzling feature initially was the apparent width of the spike, perhaps $\sim 1\text{--}2 \text{ ns}$; however, we believe this results from the finite bandwidth of the electronics, and actually the spikes are far narrower. A 1-D time-dependent simulation [5] of the experiment, including sidebands and their harmonics, reveals a "spike" feature of the laser output which is roughly 40 ps in length (Fig. 3). The code is time-dependent and the picture is obtained by plotting the amplitude of the laser signal as a function of time in one interval T , introduced for the convenience of the compu-

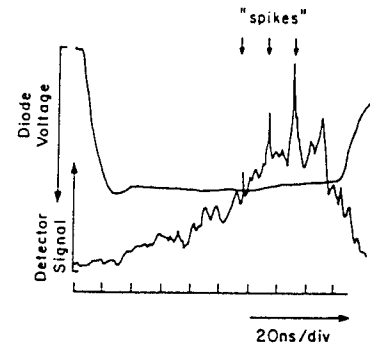


Fig. 2. A tracing of the diode (accelerator) voltage waveform (above) and the FEL power output at $\sim 2\text{-mm}$ wavelength, showing spikes.

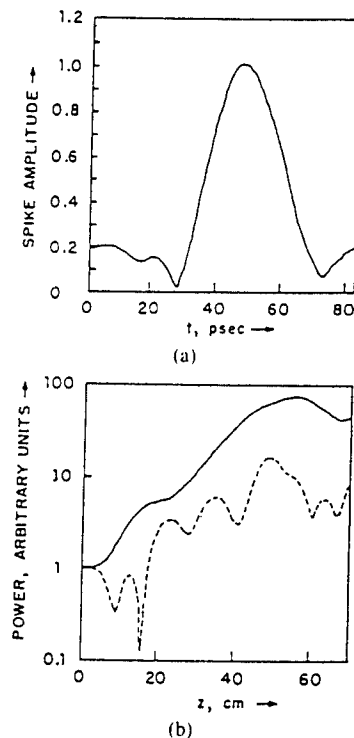


Fig. 3. A numerical study of the sideband radiation, showing the formation of a spike. (a) Time-dependent power output at the end of the FEL. (b) The growth of the long wavelength (upper curve) and short wavelength (lower curve) sidebands. Parameters are as in Table I, with $a_u = 0.3$, $\gamma = 2.55$, $k = 40 \text{ cm}^{-1}$, $\Delta\omega/\omega = 7.4\%$, and $a_z(0) = 0.0012$, where the a quantities are normalized vector potentials. The spike is synthesized from the sideband harmonics (courtesy of S. Y. Cai).

tation, $T = 2\pi/\Delta\omega$, where $\Delta\omega$ is the difference between the frequencies of the carrier and the sideband with the maximum growth rate. The Schottky-barrier detectors we use will respond to pulses this short [9], but the response observed will be degraded by the electronics bandwidth (500 MHz) and the cables. We have determined that the length of cable used accounts for an attenuation of a factor of three for the spike signals.

In Fig. 4 is shown simultaneous radiation at the carrier wavelength (1.95 mm) and the long wavelength sideband (2.2 mm). Spiking on the carrier and sidebands appears to be correlated, as well as on the sideband harmonics; however, it is not a good idea to observe spikes through the spectrometer in view of the limited bandwidth.

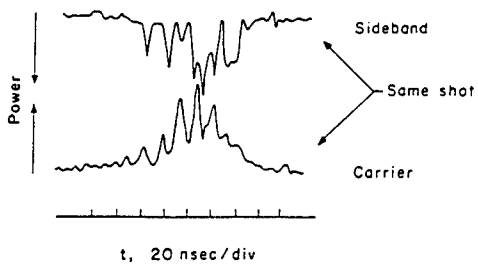


Fig. 4. Simultaneous output of the sideband and carrier observed through the spectrometer, showing spiking features: the spikes may be partly dispersed by the finite spectrometer bandwidth ($\sim 1\%$).

III. THE SPIKE EXPERIMENT

The spike pulse length can be determined with the aid of a "two-slit" Young's experiment (Fig. 5). Neglecting for the moment the structure of the diffraction pattern of the slit (determined by the slit width) and the spacing of the interference fringes (made sufficiently close by a wide slit separation), we examine how the intensity of the FEL radiation emitted by the two slits depends on the separation of the two-square-law Schottky-barrier detectors *A* and *B*, as shown. The detector *A* is placed at the symmetric location where the travel time from the two slits is equal. The spike emitted simultaneously from each slit will be superimposed coherently at detector *A*, resulting in an output response of $4E_0^2$, where E_0 is the field contribution from each slit taken separately. However, if detector *B* is moved sufficiently far from *A* and the radiation travel time from the two slits differs, say, by an amount greater than the spike width, then detector *B* will give a signal of $2E_0^2$ since the two pulses do not coherently superimpose at detector *B*. From the geometry the pulse width can be determined. For pulses ~ 100 ps-long, a slit separation of 25 cm with detectors located 1 m beyond the mask will do; the slit width is 3 mm to generate a broad diffraction pattern.

Fig. 6 shows experimental data obtained from two detectors, positioned as shown in Fig. 5. The ratio of the amplitude of corresponding spikes is measured as a function of the angle between the two detectors, keeping S_A on the axis of symmetry. The movable detector is turned as it moves in such a way that the horn remains pointed at the point halfway between the two slit radiators; in this way the receiver radiation pattern will respond equally to power emitted from each slit. It is seen that the change of power ratio emitted in spikes is about a factor of two as the movable detector is moved through about 20° , and that the characteristic falloff point is roughly 10° . From the geometry we find a pulse width of the spike of roughly 150 ps, which can be compared with the slippage distance ~ 7 cm, or 230 ps, taking a signal wavelength of 1.9 mm. The slippage distance is also the approximate coherence length of the FEL radiation. For comparison, the ratio of the average power obtained from the detector is plotted as well, but this data (diamond points) is obtained from the nonspiking part of the FEL power pulse; this will show power falloff due to diffraction as well as the much longer

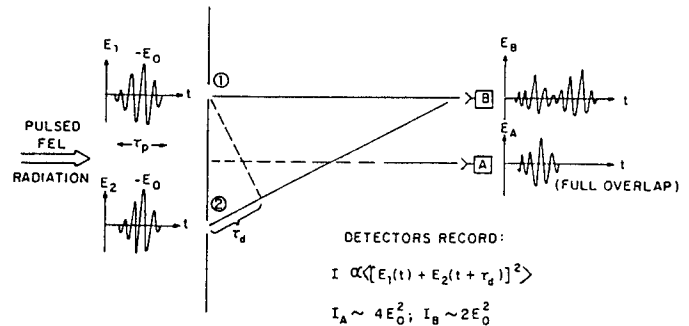


Fig. 5. Schematic of the two-slit interference experiment, showing the superposition of a short pulse of radiation emitted simultaneously from the two slits and observed by two detectors.

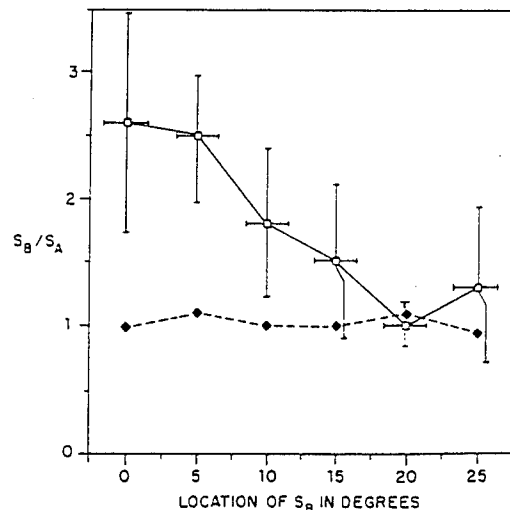


Fig. 6. Experimental data for the ratio of spike power amplitude from the two detectors (upper curve) and the ratio of the average power (lower curve).

coherence length of the laser, the latter depending on the cavity length.

Fig. 7 is a photograph of the FEL power showing an unusual double-spike emission. From the photo, the spike separation is ~ 1 – 2 ns, and from the rise of signal in between the two spikes, one might surmise that the resolution is excellent; in any event, a small fraction of the spacing. The two spikes are separated by a distance of between one-half and one unit of the undulator length; that is, by an amount which is larger than the synchrotron length but much less than the resonator length.

If we calculate the radiation intensity that would cause a synchrotron period of roughly twice the spike width, we find that the spike maximum intensity is ~ 300 – 400 MW/cm² near the electron beam, or a peak power of ~ 100 MW for the system. This corresponds to a net spike energy radiated ~ 8 – 10 mJ, which can be compared with the amount of energy in the electron beam in a slippage distance of 7 cm: 25 mJ. This shows that the spike is an efficient converter of electron beam energy into radiation. The spike power is enhanced roughly a factor of ten over the average FEL power.

The high-intensity and short pulse width of the spike

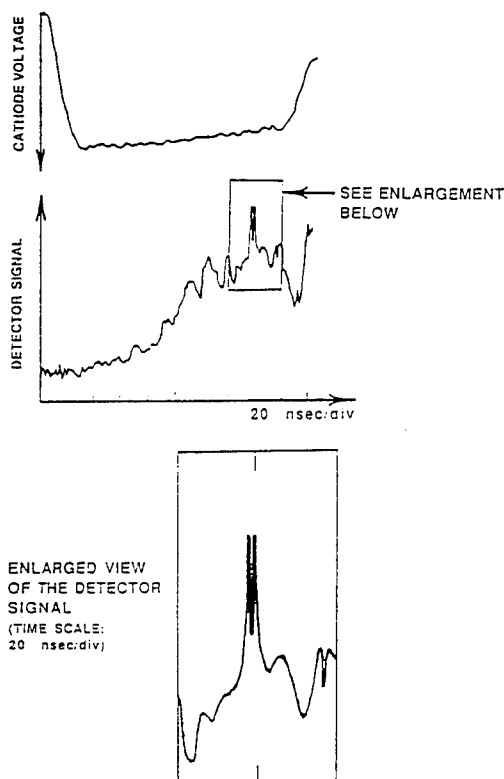


Fig. 7. FEL power pulse showing an unusual double spike feature: the accelerator voltage shows appreciable droop here.

make it an attractive feature of the FEL for particular applications: however spiking requires further study and development of new techniques to render the spikes as reproducible features before these advantages will be useful. Direct observation of spiking behavior has been reported recently on 3- μm wavelength radiation emitted from the MKIII FEL at Stanford [10].

ACKNOWLEDGMENT

The authors appreciate the assistance of Dr. S. Y. Cai with the sideband and spike calculations.

REFERENCES

- [1] W. B. Colson, "Chaotic optical modes in FELs," *SPIE*, vol. 453, pp. 290-296, 1983.
- [2] W. B. Colson and R. A. Freedman, "Synchrotron instability for long pulses in FEL oscillators," *Opt. Commun.*, vol. 46, pp. 37-42, 1983.

- [3] D. C. Quimby, J. M. Slater, and J. P. Wilcoxon, "Sideband suppression in FEL's with multiple synchrotron periods," *IEEE J. Quantum Electron.*, vol. QE-21, pp. 979-987, 1985.
- [4] R. W. Warren, J. C. Goldstein, and B. E. Newnam, "Spiking mode operation for a uniform period wiggler," *Nucl. Instrum. Methods*, vol. A250, pp. 19-25, 1986.
- [5] S. Y. Cai, A. Bhattacharjee, S. P. Chang, J. W. Dodd, and T. C. Marshall, "Effects of optical guiding on sideband instabilities in a free electron laser," *Phys. Rev.*, vol. A40, pp. 3127-3135, 1989.
- [6] S. Riyopoulos and C. M. Tang, "The structure of the sideband spectrum in free electron lasers," *Phys. Fluids*, vol. 31, pp. 1708-1719, 1988.
- [7] A. Bhattacharjee *et al.*, "Theory and observation of optical guiding in a free electron laser," *Phys. Rev.*, vol. A40, pp. 5081-5091, 1989.
- [8] F. G. Yee, J. Masud, T. C. Marshall, and S. P. Schlesinger, "Power and sideband studies of a Raman FEL," *Nucl. Instrum. Methods*, vol. A259, pp. 104-106, 1986.
- [9] Hughes Aircraft Co., private communication.
- [10] B. A. Richman, J. M. J. Madey, and E. Szarmes, "First observation of spiking behavior in the time domain in a free electron laser," *Phys. Rev. Lett.*, vol. 63, pp. 1682-1684, 1989.

*



James W. Dodd (S'83) was born in Pasadena, CA, on December 30, 1959. He received the B.S. degree in physics from Harvey Mudd College, Claremont, CA, in 1982, and the M.S. and Ph.D. degrees in applied physics from Columbia University, New York, NY, in 1983 and 1990, respectively.

He was a member of the technical staff—physics at the Hughes Aircraft Company, Electron Dynamics Division, Torrance, CA, between 1983 and 1986, where he worked on the development and manufacture of traveling wave tube amplifiers. He was a part-time Instructor in the Physics Department at California State University, Long Beach, during the 1985 spring term. Presently he holds a postdoctoral position as an Assistant Research Physicist with the Center for Advanced Accelerators in the Department of Physics at the University of California, Los Angeles. His research interests include free electron lasers and quantum electronics.

Dr. Dodd is a member of the American Physical Society, the International Society for Optical Engineering, the Optical Society of America, and Sigma Xi.

*

T. C. Marshall, photograph and biography not available at the time of publication.

Solitary Wave Spikes Emitted from a Microwave Free-Electron Laser

Li-Yi Lin and T. C. Marshall

Department of Applied Physics, Columbia University, New York, New York 10027

(Received 1 February 1993)

Narrow, high-power "spikes" can be emitted by a 24-GHz free-electron laser (FEL). Spikes, ~ 450 psec long, may occur randomly or in a sequence which is not the mode-locked period of the resonator. The slippage of the FEL is varied by changing the diameter of the drift tube. The slippage is zero when the electron axial speed is the same as the wave group velocity. Spiking was observed with and without slippage. Measurements of the FEL spectrum are reported and we compare the spike width with a solitary-wave theory. The experiment rules out the sideband instability or superradiance as a cause for this spiking.

PACS numbers: 41.60.Cr

When the free-electron laser (FEL) is operated under conditions of high power, it is possible that the emission can break up into narrow pulses of high-intensity radiation which are called "spikes." This feature has been observed in numerical simulations [1-3] as well as experiments [4,5] where the radiation field is high enough to make the synchrotron period shorter than the undulator length. While these observations relate to the nonlinear state of saturated power in an oscillator, narrow pulses of mode-locked radiation also have been observed by Jerby, Bekefi, and Wurtele [6] under conditions where the radiation field is still in the linear regime of exponential growth; these spikes may have been initiated by pulses in the electron beam current. A model has been proposed by Warren, Goldstein, and Newnam that connects the spiking to the sideband instability [3]; this instability has been studied [7,8] experimentally in a millimeter-wave FEL device at Columbia. The latter experiments were all conducted under conditions where there is finite "slippage," which depends on the difference between the group velocity (v_g) of light waves and the axial speed ($v_{||}$) of the electrons. Spikelike pulses of radiation are also believed to occur from superradiance, which itself requires slippage of the radiation pulse off a pulse of

bunched electrons in an FEL [9-12].

We report an experiment where the FEL can be operated at nearly zero slippage under conditions where the electron beam pulse is essentially infinitely long; our finding is that spiking persists. A model of the nonlinear state of the FEL has been developed by Cai and Bhattacharjee [13] and Bonifacio, Maroli, and Dragan [14]; in the former work, it is shown that the radiation field satisfies a Ginzburg-Landau (GL) equation which has solitary-wave solutions, among them being singularities which resemble spikes and which we compare with our data. In this Letter we show by an experiment and a numerical study of the GL theory that spiking survives the zero-slippage condition where the sideband instability should become stable [15].

Our experiment was done using a Pulseline accelerator, which delivers a 150-nsec, 600-800-kV pulse to a diode (field emission cathode) immersed in a guiding field ~ 1 T. The experiment is operated as a microwave FEL near 24 GHz, using a bifilar helical undulator with period of 4 cm. The FEL operates (Fig. 1) as either a 24-GHz amplifier using signal from a magnetron, or as an oscillator (at high gain the device oscillates due to reflection at the end of the drift tube). A spectrometer was used to

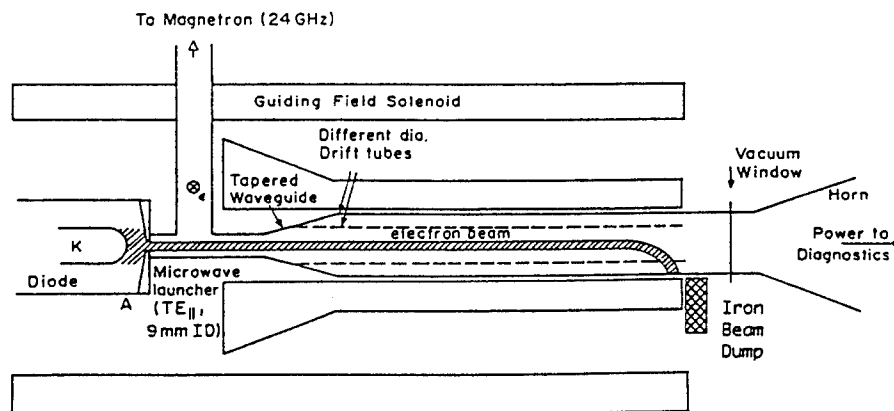


FIG. 1. Experimental apparatus, showing how the bifilar undulator winding is positioned over the drift tube. The magnetron is used only for particular experiments described in the text; ordinarily the FEL is made to oscillate for a sufficiently large undulator field, > 0.8 kG, corresponding to an undulator parameter ~ 0.5 in the guide field of 0.95 T.

monitor radiation from 19 to 35 GHz emitted from the FEL. In order to change the slippage, we use drift tubes having different inside diameter. The larger drift tube (i.d. 24 mm) is for "conventional" FEL operation with finite slippage at a beam energy of 620 kV, while zero slippage can be obtained at 22 GHz for a 710-kV beam with a drift tube i.d. of 17 mm. The larger drift tube had a ratio of electron parallel velocity to wave group velocity of 0.91 under operating conditions. For a twenty-period undulator, this gives a slippage time ~ 300 psec at 24 GHz for the larger tube; however, in the smaller drift tube the slippage time varies from zero to ~ 100 psec across the band of frequencies that we observe to be emitted.

Calibration of the undulator magnetic field was done for each configuration, as the penetration of the field from the pulsed capacitor bank which powers the undulator depends on the diffusion of field through the stainless steel walls of the drift tube. The undulator has a 10-cm entry zone where the helical field gradually increases. The undulator is pulsed to produce a field of 0.9 kG, which causes a transverse beta of 0.22 (undulator parameter, 0.5) in the guiding field. The microwave coupler is designed to launch a TE₁₁ mode into the drift tube from the rectangular waveguide that connects to the magnetron. The diode voltage of the accelerator is adjusted to amplify radiation at 24 GHz. Most of the data were taken with the FEL in an oscillator mode, with the magnetron off. The FEL output signal lasts about 100 nsec and

reaches a power of approximately 10 MW.

Figure 2 shows portions of two typical shots where spiking appears. The data were taken with a Tektronix SCD 5000 Transient Digitizer, which has a maximum acquisition rate of 200 GS/sec and an analog bandwidth of 4.5 GHz. Data obtained from several shots permit a measurement of the spike FWHM, 450 ± 100 psec. Spikes may occur singly with random spacing, or in a periodic array (as in Fig. 2) throughout the duration of the saturated FEL power pulse. The periodicity is not related to the round trip travel time of radiation in the drift tube, which is 7 nsec.

Spiking was observed under all conditions of operation, for near zero and finite slippage, for spectra which showed sidebands, and for spectra which showed more nearly coherent emission obtained by using a resonant reflector. Spikes are emitted from the oscillator even when a strong "seed" signal (~ 20 kW, 24 GHz) is injected into the system; this signal causes the oscillator to emit a much narrower band of frequencies centered on 24 GHz. The average spike width was not found to depend on the size of the drift tube.

The spectrum of the radiation was obtained with a grating spectrometer; the 24-GHz magnetron was used to

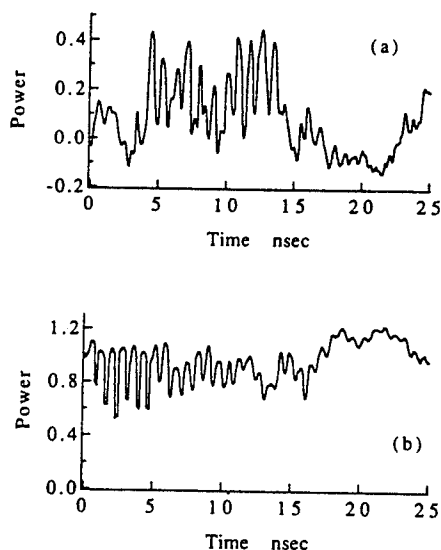


FIG. 2. Examples of spiking on the high power output of the FEL. (a) Operating near 24 GHz as an oscillator with a Bragg reflector at nearly zero slippage (710 kV, 17-mm drift tube); (b) oscillator with much larger slippage (620 kV, 24-mm drift tube). Spiking occurs from 4 to 13 nsec in (a), and from 0 to 11 nsec in (b). Power scale is in arbitrary units. Note FEL power level in (a) is lower than in (b). These portions of the laser pulse are taken following saturation.

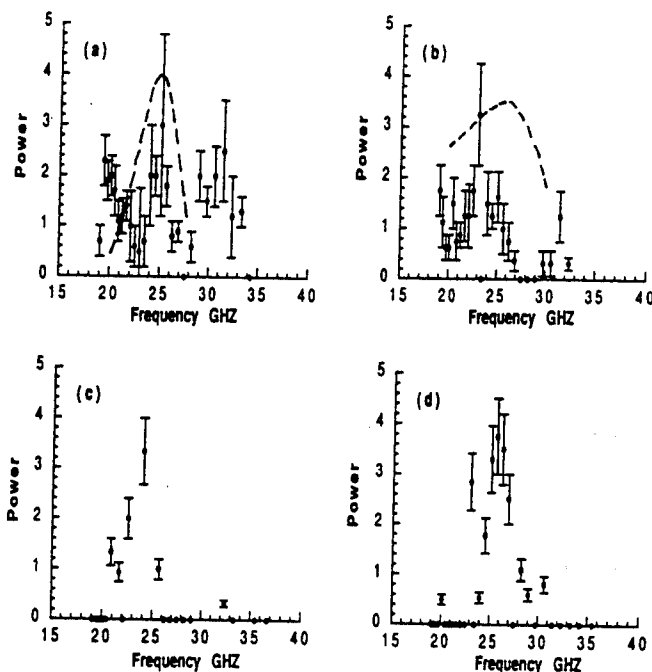


FIG. 3. Power spectrum (arbitrary units). (a) 24-mm i.d. drift tube FEL oscillator ($V=620$ kV); (b) 17-mm i.d. drift tube FEL oscillator ($V=710$ kV); (c) same as (b), but with a 20-kW signal injected at 24 GHz; (d) same as (b), but with a Bragg reflector installed at the output of the FEL. (a) and (b) also show the single-pass unsaturated power gain (dashed curve), calculated using the code described in Ref. [8]; this shows the spectral zone over which appreciable power output can occur. "Error bars" indicate the range over which the experimental data fluctuate.

calibrate the wavelength scale. Several spectra are shown in Fig. 3: 3(a) is the output of the oscillator operated with a 24-mm drift tube (620 kV), while 3(b)–3(d) are spectra of the 17-mm drift tube (710 kV). In Fig. 3(a) there appear what might be sidebands, which have about the correct displacement from the 24-GHz carrier, $\sim \pm 15\%$, considering the synchrotron period and the slippage [8]. The carrier is identified by the beam energy for which the magnetron signal at 24 GHz shows maximum gain. In Fig. 3(b) we find the sidebands are much less prominent. The gain spectrum becomes very wide when the “tangency” condition ($v_{\parallel} = v_g$) applies, as indicated by a numerical calculation of the single pass power gain in the small signal limit (dashed line). In Fig. 3(c) a high-power “seed” signal is injected into the oscillator, and we find that the oscillation now occurs at the same frequency as the input, with no sidebands apparent (at tangency condition, the sideband instability is suppressed [15]). Finally, in Fig. 3(d) we show the spectrum of the 17-mm drift tube FEL oscillator under conditions when the output power is reflected by a 26-GHz Bragg reflector [16], showing a much more coherent [17] operation than in Fig. 3(b); there appear to be no sidebands of the type found in Fig. 3(a). Spiking nevertheless has been observed under all conditions. The detectors in the spectrometer average over the spiking phenomena, and therefore the spectra that we show here describe the FEL output in some “average” sense, so that a Fourier transform of these spectra would not necessarily result in a spike pulse.

We now compare the observed spiking with the prediction of a solitary wave theory [13] applicable to our experiment. This theory represents the gain and dispersive behavior of the FEL signal by a Ginzburg-Landau equation:

$$\frac{\partial A}{\partial z} = i\lambda_0(\omega_0)A - v_g^{-1} \frac{\partial A}{\partial t} - \frac{i}{2}(\alpha_1 + i\alpha_2) \frac{\partial^2 A}{\partial t^2} + i\beta|A|^2 A. \quad (1)$$

In the above, A represents the amplitude of the electromagnetic wave, α_1 is the group velocity dispersion, α_2 is the gain dispersion, $\lambda_0(\omega_0)$ is the optimum eigenvalue of the signal growth at frequency ω_0 , and β is a complex coefficient which determines the signal saturation and is obtained by a WKB analysis of the reduced FEL equations in Ref. [13]. Two types of analytic solutions were obtained for the solitary-wave type of pulse: a periodic array of very narrow spike singularities and a broader isolated spike [see Eqs. (17) and (16), respectively, of Ref. [13]]. In the case of our experiment, the first solution predicts spikes of FWHM ~ 7 psec and spacing ~ 22 psec, which is too fast for our apparatus to record. The broader spike is predicted by the theory (see below) to have FWHM $T \sim 330$ psec, which compares with the experimental measurement of FWHM (450 ± 100) psec.

This broader spike solution has a power profile varying as $\sim 1/\cosh^2(1.76t/T)$, which we have found to be an acceptable representation of a typical observed spike in Fig. 2(a). In Ref. [13], it was pointed out that the analytic solitary-wave solutions come in two families, but it is not possible to determine which class of solutions will actually occur. This may depend on the initial conditions of the experiment, for example, irregularities of the electron beam current.

We have programmed the solution of the GL equation to study the evolution of spikes from different initial conditions. The coefficients in Eq. (1) are determined using a numerical simulation [8] to obtain $\lambda(\omega)$ (thus the waveguide and the beam filling factor are accounted for), and for the experimental data appropriate to Fig. 2(a), $v_g/c = 0.91$, $\text{Im}(\lambda_0) = 0.084 \text{ cm}^{-1}$, $\alpha_1 = 2.2 \times 10^{-23} \text{ sec/cm}^2$, $\alpha_2 = 7.2 \times 10^{-24} \text{ sec/cm}^2$ [the experimental value for $\text{Im}(\lambda_0)$ is 0.05 cm^{-1}]. The beta ($\beta_r = 20 \text{ cm}^{-1}$, $\beta_i = 4.7 \text{ cm}^{-1}$) is obtained from $\lambda(\omega)$. If one injects a small amplitude initial spike that resembles the analytic solution with the correct phase, it will grow to several MW intensity, maintaining a width of 330 psec throughout the growth as shown in Fig. 4(a). If one chooses an initial spike that has the correct amplitude profile, but not the correct phase, then as it grows and reaches saturation, it

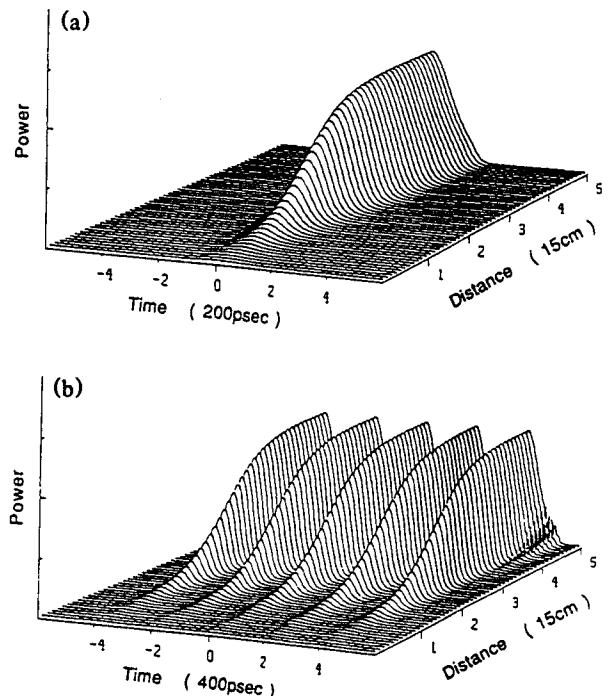


FIG. 4. (a) Growth and saturation of a solitary pulse along the electron beam of the microwave FEL using a numerical solution of the GL equation; parameters are appropriate to the data shown in Fig. 2(a) and give a pulse 330 psec FWHM. (b) A group of spikes, 330 psec wide, spaced 800 psec apart, obtained from the GL equation, similar to those found in Fig. 2. The vertical scale is the same in (a) and (b) and the calculation extends to 75 cm.

will become broadened. Thus it is possible for certain irregularities of the excitation that satisfy the initial conditions to grow into spikes in accord with the analytical solution while others may not. The experiment also showed sequences of closely spaced spikes, which we simulated with a string of initial pulses each of which has the amplitude and phase of the exact solution of the GL equation. If the spacing of the spikes is a few FWHM times, each pulse evolves almost independently, maintaining its width. When the spacing is narrowed excessively, in deep saturation there appear additional pulses of FWHM ~ 10 psec from the interference (our microwave detector cannot resolve such a short pulse). In Fig. 4(b), the spike spacing is 800 psec, as found in the data of Fig. 2, but if the spacing is reduced to one FWHM, the individual spike feature disappears.

We have found that the FEL has the capability to produce narrow pulses of high-power radiation in both the linear as well as the nearly saturated regime, even in the case of almost zero slippage and very long electron pulse. Thus we rule out the sideband instability and superradiance in connection with the spiking we have observed. The Ginzburg-Landau equation model of the FEL shows that spike pulses that have amplitude and width which agree with our experimental observations can evolve. Although the model also predicts the existence of periodic spiking solutions, thus far we are unable to quantitatively account for the interpulse spacing observed experimentally. Injection of a single solitary pulse at the input of a traveling-wave FEL amplifier as described above would result in a solitary wave with interesting features.

The authors acknowledge the help of Michael Cecere with the Transient Digitizer system, discussions with Professor A. Bhattacharjee, and the cooperation of Dr. Mary Potasek in connection with the program of the Ginzburg-Landau equation. This research was supported by the

ONR.

-
- [1] W. B. Colson and R. A. Freedman, *Opt. Commun.* **46**, 37 (1983).
 - [2] D. C. Quimby, J. M. Slater, and J. P. Wilcoxon, *IEEE J. Quantum Electron.* **21**, 979 (1985).
 - [3] R. W. Warren, J. C. Goldstein, and B. E. Newnam, *Nucl. Instrum. Methods Phys. Res., Sect. A* **250**, 19 (1986).
 - [4] B. A. Richman, J. M. J. Madey, and E. Szarmes, *Phys. Rev. Lett.* **63**, 1182 (1989).
 - [5] J. W. Dodd and T. C. Marshall, *IEEE Trans. Plasma Sci.* **18**, 447 (1990).
 - [6] E. Jerby, G. Bekefi, and J. S. Wurtele, *Nucl. Instrum. Methods Phys. Res., Sect. A* **304**, 107 (1991).
 - [7] F. G. Yee, J. Masud, T. C. Marshall, and S. P. Schlesinger, *Nucl. Instrum. Methods Phys. Res., Sect. A* **259**, 104 (1986).
 - [8] S. Y. Cai, A. Bhattacharjee, S. P. Chang, J. W. Dodd, and T. C. Marshall, *Phys. Rev. A* **40**, 3127 (1989).
 - [9] R. Bonifacio, C. Maroli, and N. Piovela, *Opt. Commun.* **68**, 369 (1988).
 - [10] W. M. Sharp *et al.*, *Nucl. Instrum. Methods Phys. Res., Sect. A* **285**, 217 (1989); see also **296**, 535 (1990).
 - [11] S. Y. Cai, J. Cao, and A. Bhattacharjee, *Phys. Rev. A* **42**, 4120 (1990).
 - [12] G. T. Moore and N. Piovela, *IEEE J. Quantum Electron.* **27**, 2522 (1992).
 - [13] S. Y. Cai and A. Bhattacharjee, *Phys. Rev. A* **43**, 6934 (1991).
 - [14] R. Bonifacio, C. Maroli, and A. Dragan, *Opt. Commun.* **76**, 353 (1990).
 - [15] S. S. Yu *et al.*, *Nucl. Instrum. Methods Phys. Res., Sect. A* **259**, 219 (1987).
 - [16] M. C. Wang, V. L. Granatstein, and R. A. Kehs, *Appl. Phys. Lett.* **48**, 817 (1986).
 - [17] B. G. Danly *et al.*, *Phys. Fluids B* **4**, 2307 (1992).

A solitary wave theory for spiking pulses emitted by a Raman free electron laser

Li-Yi Lin, T.C. Marshall *, M.A. Cecere

Department of Applied Physics, Columbia University, New York City 10027, USA

We have extended a solitary wave theory for high power spike pulses emitted from a FEL by including the space charge wave and treating the radiation field in two dimensions so as to allow for the waveguide. In this manner we derive the “collective variables” equations which describe the physics of the Columbia Raman FEL. The refractive index of the electron beam and the saturation intensity of the radiation field are obtained from a WKB theory. It is shown that the nonlinear behavior of the radiation field can be modeled by the Ginzburg–Landau (GL) equation using coefficients which are obtained from the collective variables analysis. The GL equation has solitary wave solutions that have a spiking character, lasting a few hundred ps. We program the GL equation to study the spike evolution from different initial conditions: an isolated spike resembles a solitary wave solution of the GL equation and is compared with experiment. We have examined how spikes grow from “noisy” initial conditions in the signal field as well as fluctuations in the beam current.

In four recent publications [1–4], we have reported on spiking radiation pulses that we have observed emitted from a Raman free electron laser operating at centimeter and millimeter wavelengths (see Table 1). These pulses of radiation, a few hundred ps in width, appear under conditions of high power saturated output, during “long-pulse” operation, either with or without slippage or sideband radiations. Spikes can be distinguished from the more nearly random fluctuations in signal amplitude which can be caused by the interaction of the various cavity longitudinal modes. Spiking output from FELs has also been studied using numerical models [5–7], and so we might regard this mode of operation of the FEL as perhaps typical. Spiking output may or may not be useful, depending on the intended application of the FEL. Our purpose in this paper is to present a radiation model for the FEL which has, as a result of certain conditions, predicted solitary wave type spiking pulses of radiation.

Our physical model for the FEL is that of an optical fiber, where signal propagation is characterized by parameters such as group velocity, dispersion, etc. The customary coupled electron–radiation equations for the FEL are replaced by a single radiation equation [8] which is a nonlinear Schrödinger equation with com-

plex coefficients, commonly known as the Ginzburg–Landau [GL] equation:

$$\frac{\partial A}{\partial z} = i\lambda_0(\omega_0)A - v_g^{-1} \frac{\partial A}{\partial t} - \frac{i}{2}(\alpha_1 + \alpha_2) \frac{\partial^2 A}{\partial t^2} + i\beta|A|^2 A. \quad (1)$$

In this equation, A represents the amplitude of the electromagnetic wave, α_1 is the group velocity dispersion, α_2 is the gain dispersion, $\lambda_0(\omega_0)$ is the optimum eigenvalue for signal growth at frequency ω_0 , and β is a complex coefficient which determines the signal saturation and which is obtained by a WKB analysis of the reduced FEL equations in ref. [8]. The coefficients in the GL equation are obtained from a suitable model of the FEL, such as the “collective variable” equations [9]. The advantage of considering the GL equation is that the behaviour of the signal includes a range of frequencies unlike that obtained by the full set of FEL equations, which are accessible only via numerical study. In particular, the GL equation has two types of analytical solutions for a solitary-wave type of pulse: a periodic array of very narrow singularities and a broader, isolated type of spike. The theory has been compared with experimental results [4] obtained under conditions where there is no slippage or evidence for sideband instability, where nevertheless spiking pulses were observed.

* Corresponding author.

Table 1
Operating parameters

Undulator period (helical)	4 cm
Undulator length	80 cm
Electron pulse length	150 ns
Electron beam diameter	6 mm
Beam current density	~ 2 kA/cm ²
Drift tube (waveguide) diameter	24 mm 17 mm
Electron beam energy	620 keV 720 keV
Slippage time	~ 300 ps 0–60 ps
Wiggler parameter	~ 0.5
FEL wavelength	~ 12.5 mm

In what follows, we shall refine the collective variables theory to include the effects of a waveguide (important for our experiment) as well as the space charge effects that occur for Raman operation. This will provide us with a more accurate model with which to predict the coefficients to be used in the GL equation. We then present computations which start the signal from random noise, and demonstrate that spikes could possibly arise from irregularities in the electron beam current.

The analysis begins by casting the 2-D FEL equations for a Raman FEL with a helical undulator and no slippage [10] into the “collective variables” formulation [9]. The EM field is represented as a TE₁₁ mode. Defining:

$$x \equiv \langle e^{-i(\psi_r - \psi_s - \phi)} \rangle,$$

$$y \equiv \langle \frac{\gamma_j - \gamma_0}{\gamma_0} e^{-i(\psi_j - \psi_s - \phi)} \rangle,$$

$$A = ue^{i\psi_r},$$

where ψ_r is defined by the relation $d\psi_r/dz = k_\omega(1 - \gamma_r^2/\gamma_0^2)$ and γ_0 is the energy of the electron beam, we find the FEL equations become:

$$\frac{dA}{dz} = i(\delta + p - k_s)A + igx, \quad (2a)$$

$$\frac{dx}{dz} = -ihy, \quad (2b)$$

$$\begin{aligned} \frac{dy}{dz} = & ifA - 2ihy_0(y - xy_0) + 2i\delta xy_0 \\ & - 2if(x^*A + A^*x)x - iBx, \end{aligned} \quad (2c)$$

where

$$\begin{aligned} \delta = & k_\omega(1 - \gamma_r^2/\gamma_0^2), \quad f = k_\omega a_\omega / 2\gamma_0^2, \\ g = & \omega_p^2 a_\omega k_s \xi / 2\gamma_0^2, \quad h = k_s(1 + a_\omega^2) / \gamma_0^2, \\ B = & \omega_p^2 / k_s \gamma_0 c, \quad \xi = r_b^2 \frac{F}{p^2(R^2 - 1/\kappa^2)J_1^2(\kappa R)}. \end{aligned}$$

Compared with the 1-D Compton FEL set of equations, Eqs. (2) have the extra terms $i(p - k_s)A = k_s A$

in Eq. (2a) and the iBx term in (2c). These equations can be reduced to the third order equation for A :

$$\begin{aligned} \ddot{A} - (i\Delta - 2i\epsilon hy_0)\dot{A} + [2\epsilon hy_0(\Delta - \epsilon hy_0 - \delta) + Bh]A \\ - ih(fg + BA + 2\epsilon y_0 \delta \Delta)A \\ + \frac{2\epsilon fh}{ig}[-2\Delta|A|^2 + (\dot{A}A^* - A\dot{A}^*)] \\ (\dot{A} - i\Delta A) = 0, \end{aligned} \quad (3)$$

where the overdots denote d/dz and $\Delta = (\delta + p - k_s)$. A small parameter ϵ is introduced to tag all terms containing y_0 which is a small quantity; initially, ϵ is set to unity. Eq. (3) can be solved by a WKB analysis described in ref. [8]; from this analysis comes the unstable root λ of the linear cubic equation as well as the saturation parameter β :

$$\begin{aligned} \lambda = & \lambda_0 + \beta|A|^2, \\ \lambda_0^3 - \Delta\lambda_0^2 - Bh\lambda_0 + h(fg + B\Delta) = & 0, \\ \beta = & -\frac{fh}{g} \\ & \times \{(\lambda_0 - \Delta)[2\lambda_0 + 4\text{Re } \lambda_0 + 4i\Delta + 2\delta(\lambda_0 + \Delta)] \\ & \times [2\text{Im } \lambda_0[2\text{Im } \lambda_0 - i(3\lambda_0 - \Delta)] - 3\lambda_0^2 \\ & + 2\Delta\lambda_0 + Bh]\}^{-1}. \end{aligned} \quad (4)$$

The coefficients α_1 and α_2 are obtained by examining the gain spectrum, $\lambda(\omega)$. A comparison of the power growth in the Columbia FEL as predicted by the FEL equations, the collective variables equations, and the WKB analysis finds a small-signal linear power growth rate $\sim 0.07/\text{cm}$ (compared with the experimental value of $0.06/\text{cm}$) and saturation level in the ~ 5 MW range, again in accord with experiment; the WKB model does not show the detail of the synchrotron oscillations at saturation.

As described in ref. [8], the WKB analysis then provides the coefficients for the GL equation. In ref. [4] it is described how a choice of these parameters consistent with our experiment will produce a solitary wave with width ~ 450 ps, which is the experimental result. In this paper, we report on two numerical results which have a bearing on why we see such spikes. To mimic the experimental signal startup, we choose input conditions for the GL equation to be random noise *both* in amplitude and in phase, and then follow the evolution of the growing signal along the electron beam. Fig. 1a shows the power evolution from random noise at $z = 0$ cm taking one random value every 32 ps; after a few cm distance, the narrow pulses emerge from noise, grow, and tend to stabilize. There is a region of growth where there is little change in spike width (Fig. 1b); however, as full saturation is reached, the spike pulses become broadened or merge

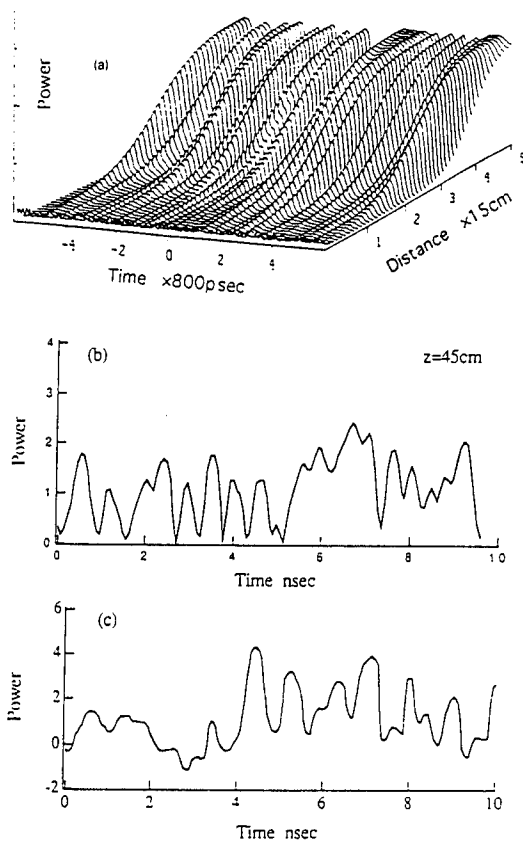


Fig. 1. (a) View of the growth and saturation of a time-varying random noise signal input at $z = 0$ cm using the GL equation with parameters appropriate to the experiment [4]. (b) The time-dependent power signal observed at $z = 45$ cm, obtained from the data of (a). (c) Experimental FEL power output signal data showing features which are qualitatively similar to those in (b). Power scale is in arbitrary units in each case.

when two pulses are close enough. By repeating the run several times with different initial noise, we find on the average that the spike width is ~ 300 ps from the code. If the amplitude (only) of the input is random noise, but not the phase, the initial pulses merely spread out. Fig. 1c shows experimental data of the spiking for comparison. Much of the spiking we observe is perhaps characteristic of incompletely saturated signal growth, but it is possible that a noise fluctuation may make a pulse that by chance is a solitary wave.

On the other hand, it is likely that startup of the FEL signal is dependent upon rapid variations in the electron current. The latter, as shown by the experimental example Fig. 2, is far from constant, and indeed shows some narrow pulse features where the current fluctuates by a factor ~ 2 which can initiate signal fluctuations [11]. To understand how these irregulari-

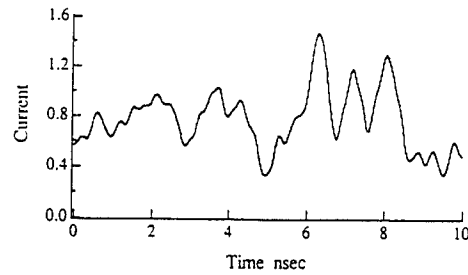


Fig. 2. Current (arbitrary units) drawn by a low inductance coaxial wire probe in the electron beam: the current pulse is 150 ns long, but this shows only a 10 ns "window". The average current is about 100 A (as determined by a Faraday cup). Note the three pulses of current between 6 and 8 ns. When the probe is out of beam, there is no noise level.

ties in current may grow into spikes, we use a crude model of a small current pulse superimposed on an otherwise uniform current (Fig. 3). As the FEL interaction commences, a current pulse will result in a signal pulse, since the gain depends on the beam density. We first obtain the power and phase profile caused by the current pulse at a short distance (20 cm) into the undulator, using FEL equations code. Further along the undulator, a larger power and phase variation across the signal pulse can be obtained, and it resembles the top half of a GL solitary wave solution. Then this is fed into the GL code as an initial pulse, and in Fig. 4 we show how a pulse having FWHM ~ 200 ps is produced. The width of the pulse enlarges very slowly with propagation, and resembles a solitary wave. This suggests that solitary wave pulses might be prepared in the FEL by causing pulses of approximately the same width to appear on the electron beam current. This can be done, for example, by irradiating the cathode with a

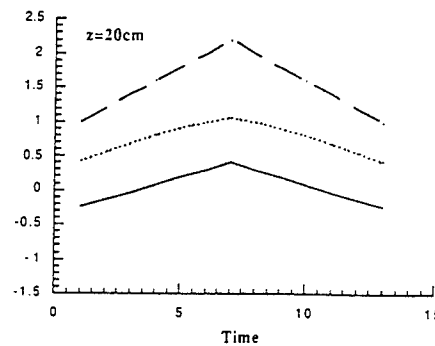


Fig. 3. A model of a current fluctuation: dashed line is a model current pulse, dotted line is the resulting FEL power and signal phase variation (solid line), in arbitrary units. Power and signal phase are calculated using the standard FEL equations which are solved numerically to generate the power and phase at $z = 20$ cm downstream along the electron beam. Time is in arbitrary units.

IV. THEORY

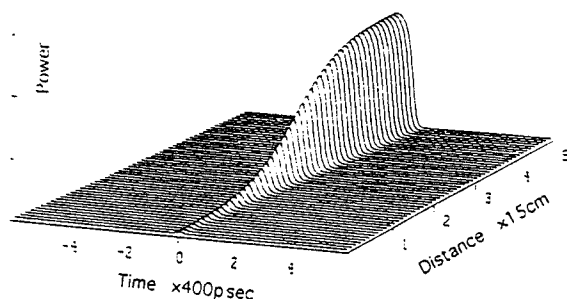


Fig. 4. Evolution of a small signal pulse. FWHM ~ 180 ps, obtained from Fig. 3 data input at $z = 50$ cm and followed downstream from there into saturation.

short pulse of intense light, e.g. a CO_2 laser pulse incident upon a cold field-emitting cathode. In this way, single, powerful solitary pulses may be produced.

We briefly summarize here our experiments with spiking as observed using a tapered undulator. Actually, two undulators were used: a constant period (1.7 cm) undulator, and a "hybrid" undulator consisting of a constant period (1.7 cm) section 30 cm in length followed by a tapered zone 46 cm in length where the period uniformly decreases to 1.4 cm at the end. Experiments were done with both undulators, in an oscillator configuration, using a 750 kV electron beam pulse. Spiking pulses of width 490 ± 70 ps were observed from the tapered undulator FEL, whereas the spiking pulses obtained from the constant period undulator were 410 ± 60 ps in length for the same conditions (a Tektronix SCD 5000 Transient Digitizer was used for these measurements and the current pulses). The wavelength radiated was ≥ 2 mm. Thus tapering

does not "destroy" the spiking phenomenon. Calculations which adapt the GL theory to the tapered undulator configuration are currently being done at Columbia.

Acknowledgment

This research was supported by the ONR.

References

- [1] J.W. Dodd and T.C. Marshall, IEEE Trans. Plasma Sci. PS-18 (1990) 447.
- [2] J.W. Dodd and T.C. Marshall, Nucl. Instr. and Meth. A 296 (1990) 4.
- [3] L.-Y. Lin and T.C. Marshall, Nucl. Instr. and Meth. A 331 (1993) 144.
- [4] L.-Y. Lin and T.C. Marshall, Phys. Rev. Lett. 70 (1993) 2403.
- [5] R.W. Warren, J.C. Goldstein and B.E. Newnam, Nucl. Instr. and Meth. A 250 (1986) 19.
- [6] G.T. Moore and N. Piovella, IEEE J. Quantum Electron. QE-27 (1992) 2522.
- [7] R. Bonifacio, L. de Salvo, P. Pierini, N. Piovella and C. Pellegrini, these Proceedings (15th Int. Free Electron Laser Conf., The Hague, The Netherlands, 1993) Nucl. Instr. and Meth. A 341 (1994) 181.
- [8] S.Y. Cai and A. Bhattacharjee, Phys. Rev. A 43 (1991) 6934.
- [9] R. Bonifacio, C. Pellegrini and L. Narducci, Opt. Commun. 50 (1984) 313; Also, R. Bonifacio et al., Phys. Rev. A 40 (1989) 4467.
- [10] S.Y. Cai, A. Bhattacharjee and T.C. Marshall, IEEE J. Quantum Electron. QE-23 (1987) 1651.
- [11] L.-Y. Lin, doctoral thesis, Department of Applied Physics, Columbia (1993).

Experimental test of the inverse free-electron-laser accelerator principle

Iddo Wernick and T. C. Marshall

Department of Applied Physics, Columbia University, New York, New York 10027

(Received 12 February 1992)

A free-electron laser was configured as an autoaccelerator to test the principle of accelerating electrons by stimulated absorption of radiation ($\lambda = 1.65$ mm) by an electron beam (750 kV) traversing an undulator. Radiation is produced in the first section of a constant period undulator ($l_{w1} = 1.43$ cm) and then absorbed ($\sim 40\%$) in a second undulator, having a tapered period ($l_{w2} = 1.8\text{--}2.25$ cm), which results in the acceleration of a subgroup ($\sim 9\%$) of electrons to ~ 1 MeV.

PACS number(s): 41.60.Cr, 41.75.Ht, 29.17.+w

The principle of using free-electron-laser (FEL) physics to accelerate electrons was described by Palmer [1] in 1972; however, despite the extensive development of the FEL there has been no demonstration of the stimulated absorption of a laser pulse accompanied by acceleration of a group of electrons while the electron beam is traversing an undulator [inverse FEL (IFEL)]. The idea has been reexamined in more detail [2–4] and appears to offer some promise to achieve an acceleration gradient ~ 1 MV/cm in linear accelerators. In the electron rest frame, the magnetostatic field of the undulator is transformed into an electromagnetic wave which beats with the laser; acceleration occurs by keeping the phase of the electrons constant, with respect to the beat wave, by varying the undulator period and/or magnetic field as the particle energy increases. We have devised a relatively simple experiment, done at the Columbia University FEL facility [5], which demonstrates that acceleration does occur.

The Columbia University FEL operates at a wavelength of 1.6 mm and produces about 5 MW from a 750-kV electron beam. As there is no powerful laser source at this wavelength, we have configured the experiment as an “autoaccelerator” (IFELA) in which a subgroup of electrons is accelerated by the “inverse FEL” mechanism at the expense of the average energy of the entire beam. This is done by separating the undulator into two sections. The first section (Fig. 1) together with a pair of 75% reflecting coaxial mirrors develops FEL radiation which grows from noise to saturated intensity and causes a bunching of the electrons. These particles then enter the second section of the undulator where the period is increased and then tapered along the axis so that a subgroup of electrons is accelerated as stimulated absorption of the wave occurs. We report measurements of this nonlinear absorption together with the electron energy spectrum. The accelerator section acts as a load for the oscillator, but its absorption is not high enough to prevent oscillation of the entire system.

Table I summarizes the parameters of the IFELA experiment. The undulator is a bifilar helical winding which provides a transverse field of order 600 G following an adiabatic entry region. The beam is guided and focused along the drift tube by a uniform solenoidal field

~ 1 T which causes “group I” orbits [6]. The FEL power examined by a grating spectrometer shows a carrier wavelength of 1.6 mm together with a pair of sidebands which carry about one-third of the total power; it was found that only the carrier was absorbed by the acceleration process [7]. The downstream mirror is polished graphite with a small hole on its axis followed by a collimator which forms the objective of the electron-beam optics. A focusing solenoid guides the electrons beyond the fringe field of the solenoid. A dipole field using triangular polefaces deflects the beam and disperses the electrons onto a quartz viewing plate where the impact causes substantial Čerenkov light [8] (the quartz is painted with an opaque graphite film on the vacuum side). The light from the energetic electrons is directed to two lead-shielded photomultipliers located in a shielded room with the other electronics. The magnetic spectrometer is calibrated by using the electron beam with no undulator. The use of two photocells permits one photocell to monitor the principal group near the injection energy while the other scans the energy channels for the accelerated electrons.

The undulator in the IFELA section is designed using a numerical model to choose the appropriate field and taper. We use a set of equations [5] that models the electron motion in one dimension (1D) along a single pass through the system and a self-consistent set of 2D field equations. A “Raman” term which accounts for the lon-

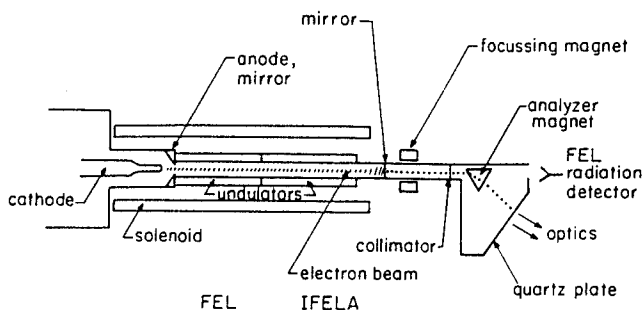


FIG. 1. Schematic of the IFELA and the magnetic spectrometer. Electron emission occurs from a cold graphite cathode in a field-immersed diode, the beam is formed by a 4-mm-diam aperture in a graphite anode, which also serves as the upstream mirror of the resonator.

TABLE I. Operating conditions of the Columbia University IFELA.

Beam energy	750–800 kV
Beam diameter	4 mm
Beam current	150 A
Pulse length	150 nsec
Drift tube diameter	11 mm
Undulator: first section	$l_{w1} = 1.4$ cm $B_1 = 600$ G length = 40 cm
Undulator: second section	$l_{w2} = 1.8$ – 2.25 cm taper = $\frac{1}{l_w} \frac{dl_w}{dz} = 0.0067$ cm $^{-1}$ $B_1 = 400$ G length = 37.5 cm

gitudinal space-charge electric field from the electron bunches is included and is necessary to obtain the correct growth rate in the FEL section and the correct interaction in the IFELA section. The electron beam in the experiment has normalized parallel momentum spread $\sim 1\%$ [9], and is represented in the numerical study as a “cold” beam, since the trapping width $\Delta\gamma/\gamma \propto \sqrt{a_s a_w}$, where a_s and a_w are the normalized vector potentials of the signal and undulator fields, is much larger than 1%.

The magnetic field of the FEL undulator section was chosen so that the power would grow roughly a factor of 25 in 40 cm. This gain will sustain oscillation and results in a signal which reaches power saturation at the point where the electrons enter the IFELA section. The saturated power intensity on the beam axis, ~ 10 MW/cm 2 , is consistent with the power output from an FEL oscillator device very similar to this one [10]. It is found numerically that the wave amplitude is reduced by one-half as it reaches the end of the IFELA undulator as a subgroup of the trapped electrons is accelerated to ~ 1 MV. The code includes no slippage and therefore does not account for sideband radiation; hence the measured absorption of the FEL power by the accelerator module will be less than the model predicts. The taper of the undulator which optimizes the absorption and acceleration is found through trial and error of the numerical study and corresponds to an acceleration gradient of ~ 7 kV/cm in this test experiment. The taper is used to generate a variable-period helix which is mapped onto a section of phenolic tube and then cut to specification “by hand.” Measurements of the actual undulator-period taper and magnetic-field taper are then incorporated into the code to simulate the actual experimental situation. Once the taper is chosen, a series of simulations show that the acceleration is not very sensitive to variation in FEL power or undulator field, however, increasing the power input to the IFELA section will accelerate more electrons. The field in the IFELA undulator can be varied independently of the FEL undulator; both are powered by a capacitor bank discharge synchronized to the accelerator timing system.

A set of representative data is shown in Fig. 2. Shots are selected for a relatively flat diode voltage history, with electron energy near resonance. A determining sig-

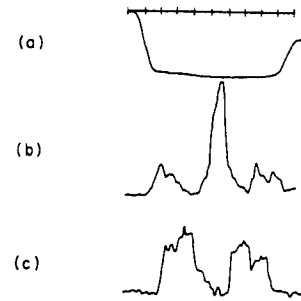


FIG. 2. Representative signals obtained in the experiment. (a) Accelerator voltage, -800 kV maximum; (b) signal from photodiode monitoring 1-MV electrons, showing a burst of electrons at middle of trace; (c) FEL power transmitted through the IFEL stage, showing absorption in middle of trace; 10 nsec/div, horizontal scale.

nature as the electron-beam energy reaches the design value is a decrease of transmitted FEL power accompanied by an increase of light signal in the photomultipliers which respond to the accelerated electrons. The energy bins are separated by the resolution of the electron-beam optics. Background light, obtained from operation of the apparatus with zero undulator field, is subtracted from the signal. The transmitted FEL power is monitored by a Schottky-barrier diode detector located along the beam axis. It is found that the fraction of power absorbed does not depend sensitively upon the power level itself. This behavior is to be expected from

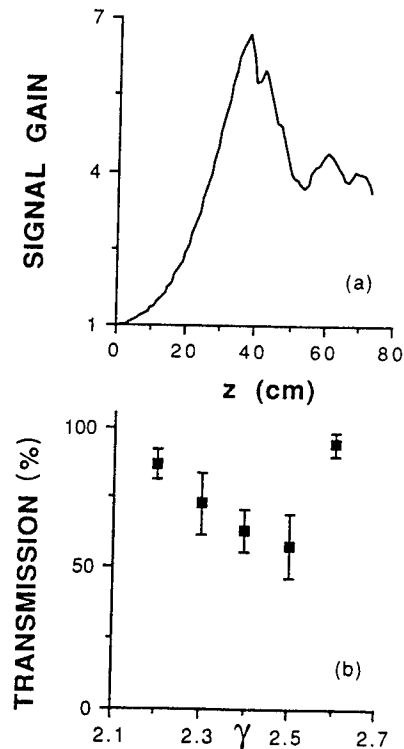


FIG. 3. (a) Numerical result showing growth of FEL signal (initial intensity 0.3 MW/cm 2) and attenuation in the IFELA section (begins at $z = 37.5$ cm). Parameters of simulation taken from Table I. (b) Radiation transmitted through the IFELA section as a function of initial electron-beam energy. Error bars indicate standard deviation of the data.

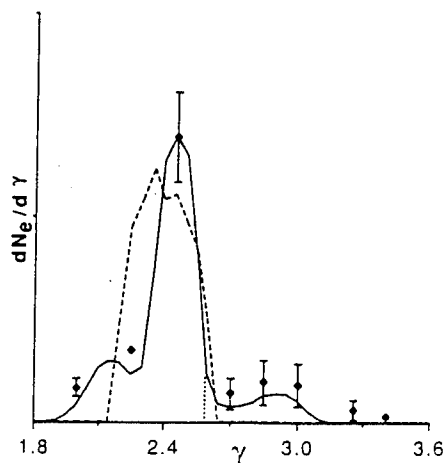


FIG. 4. Measured electron energy spectrum (solid points); electron energy spectrum obtained from simulation, at the exit from the IFELA (solid line); electron energy spectrum obtained from simulation, at entry to the IFELA section (dashed line). The dotted vertical line denotes the injection energy.

the model, which shows that increases in power absorbed result in more accelerated electrons but not necessarily higher electron energy.

Figure 3(a) displays results from a numerical simulation of the experiment showing the growth of the FEL signal, followed by the attenuation of the wave in the accelerator section. Figure 3(b) shows experimental data giving the FEL power transmitted through the accelerator section. This shows that there is a reduction of emitted power by $\sim 40\%$ in the vicinity of the resonant energy of the design. By reducing the undulator field in the accelerator section to 250 G, the amount of observed absorption decreases to about 25% of the incident power. The study of the FEL spectrum [7] shows that the sidebands of the FEL power spectrum are not absorbed by the accelerator to a measurable amount, and therefore the reduction of the incident carrier intensity ($\sim 75\%$) indicated in the numerical simulation is larger than would be obtained if the sideband power is included in the measurement, as was the case.

Figure 4 shows the measured electron energy spectrum. The data are compared with the numerical simula-

tion, run according to the experimental conditions. The computed spectrum is processed so that the ordinate corresponds to the number of simulation electrons contained in a bin having the same width as the experimental bin. The relative number of electrons accelerated and the acceleration energy are in good agreement with the numerical model. According to numerical simulation the smaller peak which occurs at $\gamma \approx 2.2$ does not result from the acceleration process. For comparison, the dashed line on Fig. 4 shows the electron spectrum computed (but not observed) at the end of the FEL section only; one notes there is a rapid cutoff of electrons having energy in excess of $\gamma = 2.7$, which is well below the energy of the accelerated group. Thus electrons at ~ 1 MV have energy beyond the broadened distribution which results from the bunching and trapping of electrons from the FEL interaction. Electrons above the injection energy in FELs have been observed [11,12], however they are not "accelerated" by the IFEL mechanism. The number of accelerated electrons is about 9% of the total number, as can be estimated from Fig. 4. The ratio of the power required to accelerate these electrons to the overall power of the electron beam is about 3%, which is less than the efficiency of the FEL (4–6 %).

In an actual IFEL where the radiation is supplied by an external laser, the undulator field can be considerably larger (roughly a factor of ten greater than in our experiment) and the intensity of the laser wave can be higher by perhaps a factor of a thousand, taking a $10.6\text{-}\mu\text{m}$ laser wavelength as an example. Then our observed acceleration gradient ~ 7 kV/cm would scale up by a factor of ~ 100 for such a device. Techniques exist to control synchrotron-radiation losses which are no longer negligible at high energy [3]. Our success with the experiment and its interpretation suggests that the IFEL is a promising technology for an "advanced accelerator" demonstration.

This research is supported by the NSF, Grant No. ECS-89-13066, U.S. DOE Grant No. 02-91ER40669, and ONR Grant No. N00014-89-J-1652. The assistance of Y.-P. Chou in the early stages of this project is greatly appreciated.

- [1] R. B. Palmer, *J. Appl. Phys.* **43**, 3014 (1972).
- [2] P. Sprangle and C.-M. Tang, *IEEE Trans. Nucl. Sci.* **NS-28**, 3346 (1981).
- [3] E. D. Courant, C. Pellegrini, and W. Zakowicz, *Phys. Rev. A* **32**, 2813 (1985).
- [4] A. van Steenbergen and C. Pellegrini (private communication).
- [5] A. Bhattacharjee, S. Y. Cai, S. P. Chang, J. W. Dodd, A. Fruchtmann, and T. C. Marshall, *Phys. Rev. A* **40**, 5081 (1989).
- [6] L. Friedland, *Phys. Fluids* **23**, 2376 (1980).
- [7] T. C. Marshall, A. Bhattacharjee, S. Y. Cai, Y.-P. Chou, and I. Wernick, *Nucl. Instrum. Methods Phys. Res. A* **304**, 683 (1991).
- [8] B. Kulke, M. J. Burns, and T. J. Orzechowski, LLNL Report No. UCRL-95598, 1988 (unpublished).
- [9] S. C. Chen and T. C. Marshall, *IEEE J. Quantum Electron.* **QE-21**, 924 (1985).
- [10] F. G. Yee, T. C. Marshall, and S. P. Schlesinger, *IEEE Trans. Plasma Sci.* **16**, 162 (1988).
- [11] A. H. Lumpkin and R. B. Feldman, *Nucl. Instrum. Methods Phys. Res. A* **259**, 19 (1987).
- [12] T. I. Smith, J. C. Frisch, R. Rohatgi, H. A. Schwettman, and R. L. Swent, *Nucl. Instrum. Methods Phys. Res. A* **296**, 33 (1990).

Enhanced harmonic emission from a “complex” undulator

Yung-Ping Chou and T.C. Marshall

Department of Applied Physics, Columbia University, New York, NY 10027, USA

The traditional scheme for generating harmonic emission from FELs requires a large ($K > 1$) undulator field to cause a sizable zeroth-order axial modulation in the electron trajectory. We propose a different concept based on the observation that the electron bunching in the nonlinear state has various harmonics. These bunches can be coupled into growing harmonic radiation fields using appropriately phased sections of undulators. An example is to use a right-polarized helical undulator in conjunction with sections of a left-polarized helical undulator; the phasing, field strength, and section length of the left-polarized elements can be optimized for a given harmonic. The two undulators can have concentric windings and several sections can be used. The first left-polarized element is located where the fundamental radiation is intense but not fully saturated, so the nonlinear bunching is sustained without the fundamental depriving the electrons of most of their free energy. Although the overall undulator is more complex, it is not difficult to build and operates at low field ($K \sim 0.3$). We will present numerical studies illustrating the potential for harmonic generation using our millimeter wavelength FEL facility.

1. Introduction

The motivation for developing harmonic radiations in an FEL device is, among others, to secure shorter wavelength for a given energy electron beam. This is of great advantage for FELs which operate with energy less than 1 MV, where one might wish to generate radiations at 0.5–1.0 mm wavelength for the purpose of electron cyclotron heating of Tokamak fusion devices. A reduction of energy by a factor of two or more would permit a much less expensive technology to be used for the production of CW FEL energy.

The standard theory of harmonic generation in an FEL is described by Davidson [1] and harmonic radiation was observed in experiments by Bamford [2] and Warren [3]. An electron beam passing through a strong, linearly polarized undulator field ($a_w \geq 1.0$) experiences a significant longitudinal velocity modulation and, hence, excites growing harmonic radiation at odd harmonics. However, use of large a_w tends to defeat the purpose of producing shorter-wavelength radiations since it causes an increase of FEL wavelength, as well as a broader FEL gain spectrum.

We have therefore considered how one might obtain appreciable FEL power at the second or third harmonic using $a_w \ll 1.0$. Such a weak undulator field cannot cause strong harmonic electron motion, therefore most of the available electron energy flows into the fundamental and harmonic radiations never grow beyond threshold in an oscillator. Thus one must suppress not only the radiation growth at unwanted harmonics but also at the fundamental. One approach

described by LANL [3] is the “compound” undulator, where different windings are arranged longitudinally so that only one prescribed harmonic will experience growth throughout the entire device.

It has been observed [2,4] that an FEL oscillator will emit harmonic radiation, although the level is orders of magnitude less than the fundamental. This phenomenon is due to the harmonic currents of the bunched electron beam which occur in the nonlinear state. The harmonic power remains small because the undulator provides no higher harmonic magnetic fields and so it dephases the harmonic emissions. The energy flow from the fundamental to the harmonic is quite small. These points were established by others [2,4] but we present in fig. 1a our own numerical computation for reference, using parameters appropriate for the Columbia FEL. When the growth of the fundamental saturates, the level of the harmonic radiation is several orders of magnitude lower. At millimeter wavelengths, the harmonics are too weak to detect.

In order to convert the energy of the fundamental radiation into harmonics, it is necessary to stop the growth of the fundamental short of saturation. We do this in the following manner: the fundamental is grown from noise or a small signal in a length of helical undulator with say right-hand helicity. At a suitable point, the helicity will switch to left-handedness, but with the same period. The remainder of the undulator will consist of short sections “macroperiods” each of a few periods arranged with alternating helicity. There is also the possibility of introducing a jump of winding phase at each macroperiod in order to optimize the

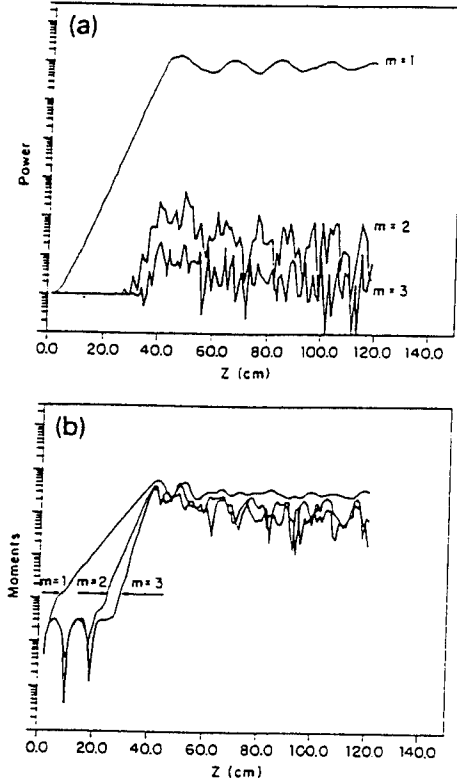


Fig. 1. (a) The fundamental, the second, and the third harmonic power in a conventional helical FEL amplifier: $a_w = 0.3$, $\lambda_w = 1.5$ cm, $\gamma_0 = 2.17$ (600 keV), and $\lambda_s = 1.81$ mm. (b) The harmonic components of the electron bunching, $\langle e^{im\psi} \rangle$, $m = 1, 2, 3$; under the same conditions as (a).

conversion to higher harmonic radiations. This last point has been noted by others [5]. We find that an improved level of harmonic power can be generated, especially at the second harmonic. Unlike other harmonic schemes, the undulator field remains "weak": $a_w \ll 1$, and we consider Raman FEL operation [6].

2. Theory

We now construct a model for the harmonic generation of an FEL. The normalized vector potential a_w of the undulator field can be most generally represented by

$$a_w = -[a_1 \hat{x} \cos k_w z + a_2 \hat{y} \sin(k_w z + \beta)] \\ = -\frac{1}{2}[\alpha(\hat{x} + \eta \hat{y}) + \text{c.c.}],$$

where $\alpha \equiv a_1 e^{i k_w z}$ and $\eta \equiv a_2 / a_1 e^{i(\beta - \pi/2)}$. The field is one-dimensional since the electron beam is on the axis of the undulator. By changing the values of η and β , this form of undulator field allows various field structures. Two limiting cases are:

- helical undulator: $\eta = -i$, $\beta = 0$.

- linear undulator: $\eta = 0$.

We take the following form of the vector potential:

$$a_s(z, t) = \sum_m [u_m \hat{x} \cos(m\psi + \phi_m) \\ - \bar{u}_m \hat{y} \sin(m\psi + \phi_m - \beta)] \\ = \frac{1}{2} \sum_m [(u_m e^{im\psi} + \text{c.c.}) \hat{x} \\ + (\bar{u}_m e^{im\psi} + \text{c.c.}) \hat{y}],$$

where $\psi \equiv k_s z - \omega_s t$, $u_m \equiv a_m e^{i\phi_m}$, and $\bar{u}_m \equiv \bar{a}_m e^{i(\phi_m - \beta - \pi/2)}$. The following assumptions are used to simplify the problem: the complex functions u_m , \bar{u}_m depend on z only (one-dimensional, nonslippage); u_m and \bar{u}_m are slow functions of z (eikonal); no waveguide; no guide field.

To obtain dimensionless equations, we normalize z to $1/k_w$ and ω_s to $k_w c$. The dynamical variables of an electron are the energy, γ , and the phase, ψ . The equations advancing these variables are:

$$\frac{d}{dz} \gamma_j = \frac{i\omega}{2\gamma_j \beta_{zj}} \sum_m m (U_m e^{im\psi_j} - \text{c.c.}) \\ - i\epsilon\omega \sum_l \frac{1}{l} (\langle e^{-il\psi} \rangle e^{il\psi} - \text{c.c.}) \quad (1)$$

$$\frac{d}{dz} \psi_j = -\frac{\omega}{2\gamma_j^2} \left[1 + \frac{1}{2} \text{Re}(\alpha \alpha_w) \right. \\ \left. - \sum_m (U_m e^{im\psi_j} + \text{c.c.}) \right] \quad (2)$$

The first term on the right-hand side of eq. (1) is the ponderomotive wave. The second term is due to space charge. The wave equations of the m th harmonic field, u_m and \bar{u}_m , are:

$$\frac{d}{dz} u_m = i\epsilon\omega\beta_{0j} \frac{\text{Re}(\alpha)}{m} \left\langle \frac{e^{-im\psi}}{\beta_{zj}\gamma} \right\rangle, \quad (3)$$

$$\frac{d}{dz} \bar{u}_m = i\epsilon\omega\beta_{0j} \frac{\text{Re}(\eta\alpha)}{m} \left\langle \frac{e^{-im\psi}}{\beta_{zj}\gamma} \right\rangle, \quad (4)$$

where $\psi_j \equiv k_s z - \omega_s \tau(z, \zeta_j)$, $\tau(z, \zeta_j) \equiv \zeta_j + \int_0^z dz' / v_{zj}$, τ is the time for j th electron with initial time ζ_j to arrive at z , $\alpha_w \equiv (1 + \eta^2)\alpha + (1 + |\eta|^2)\alpha^*$, $\epsilon \equiv (\omega_p/\omega)^2$, and $U_m \equiv \text{Re}(\alpha)u_m + \text{Re}(\eta\alpha)\bar{u}_m$.

There is a conservation law of energy from these equations.

$$\frac{1}{2} \sum_m m^2 (|u_m|^2 + |\bar{u}_m|^2) + \beta\epsilon(\gamma) = \text{constant},$$

which can be used to check the accuracy of computation. A Fourier analysis of the electron distribution in the nonlinear state in an FEL shows the existence of various harmonics (fig. 1b), and the induced harmonic current will produce harmonic radiation.

We now analyze the growth of harmonic radiation in a conventional helical undulator. A phenomenological form, $u_1 = a_0 e^{Kz}$, for the growing fundamental is assumed; then we calculate the electron bunching caused by the fundamental and incorporate this into the harmonic wave equation. The eqs. (1)–(4) are reduced to simpler forms by setting $\eta = -i$, $\beta = 0$ and $\beta_z = \beta_0$ and $\gamma_j = \gamma_0(1 + \delta\gamma_j)$, $\delta\gamma_j \ll 1$:

$$\frac{d}{dz}\psi_j = -\frac{\omega}{2\gamma_0^2}(1 - \delta\gamma_j)\left[1 + a_0^2 - (\alpha u_1 e^{i\psi_0} + \text{c.c.})\right]. \quad (5)$$

$$\begin{aligned} \frac{d}{dz}\delta\gamma_j &= \frac{i\omega}{2\gamma_0^2\beta_0}(1 - \delta\gamma_j)(\alpha u_1 e^{i\psi_0} - \text{c.c.}) \\ &\quad - i\frac{\epsilon\omega}{\gamma_0}(\langle e^{-i\psi} \rangle e^{i\psi_0} - \text{c.c.}), \end{aligned} \quad (6)$$

and

$$\frac{d}{dz}u_m = i\frac{\epsilon\omega\alpha^*}{\gamma_0 m}(\langle e^{-im\psi} \rangle - \langle \delta\gamma e^{-im\psi} \rangle). \quad (7)$$

Assume the electron phase, ψ_j , is composed of two parts, $\psi_j = \psi_{0j} + \psi_{1j}$, ψ_{0j} coming from the modulation of the undulator field and ψ_{1j} from bunching. Since ψ_0 and ψ_1 are of different order, we may first write down the equation for ψ_{0j} from eq. (5):

$$\frac{d}{dz}\psi_{0j} = -\frac{\omega}{2\gamma_0^2}(1 + a_0^2).$$

And the solution is $\psi_{0j} = \xi_{0j} - bz$, where $b = (\omega/2\gamma_0^2)(1 + a_0^2)$, and ξ_{0j} is the initial phase. The equation for ψ_{1j} is:

$$\frac{d}{dz}\psi_{1j} = b\delta\gamma_j + \frac{\omega}{2\gamma_0^2}(\alpha u_1 e^{i\psi_{0j}} + \text{c.c.}). \quad (8)$$

For a Raman FEL where a_w is small, the equation for $\delta\gamma_j$ becomes:

$$\frac{d}{dz}\delta\gamma_j = -i\frac{\epsilon\omega}{\gamma_0}(\langle e^{-i\psi} \rangle e^{i\psi_0} - \text{c.c.}).$$

The ensemble averaged term on the right-hand side can be obtained from eq. (7) with $m = 1$:

$$\langle e^{-i\psi} \rangle = -i\frac{\gamma_0 K u_1}{\epsilon\omega\alpha^*}.$$

Solving for $\delta\gamma_j$ and maintaining $e^{Kz} \gg 1$ we obtain:

$$\begin{aligned} \delta\gamma_j &= -2\frac{Ku_1}{a_w}\frac{1}{K^2 + \Delta^2}\left[K\cos(\Delta z - \xi_{0j})\right. \\ &\quad \left.+ \Delta\sin(\Delta z - \xi_{0j})\right] \\ &= -2\frac{u_1}{a_w}\cos(\xi_{0j} - bz), \end{aligned}$$

where $\Delta = b - 1$, $|\Delta| \ll 1$.

Inserting $\delta\gamma_j$ into eq. (8), the solution of ψ_{1j} is:

$$\psi_{1j} = -\frac{b}{Ka_w^2}u_1(\alpha e^{i\psi_{0j}} + \text{c.c.}).$$

After putting the newly solved ψ_{0j} , ψ_{1j} , and $\delta\gamma_j$ on the right-hand side of the second-harmonic wave equation, we find that the linear terms vanish after being ensemble averaged (therefore, the second harmonic radiation amplitude is one order smaller than the fundamental). What remains is:

$$\frac{d}{dz}u_2 = \frac{\epsilon\omega}{\gamma_0}\frac{b^2}{K^2}\frac{1}{a_w^3}\left(\frac{K}{b} + e^{iKa_w z}\right)u_1^2.$$

Thus the second harmonic has a growth which scales as e^{2Kz} , but the term, $e^{iKa_w z}$, dephases the growth, and hence u_2 does not reach a significant level in a conventional helical undulator. But the other term, K/b , which is due to the space-charge effect (Raman-type operation), does not dephase the resonance and helps maintain the second harmonic signal. Thus it is easier to excite harmonic radiation in a Raman FEL.

The above analysis shows the main difficulty of producing harmonic radiation in a simple helical undulator is the dephasing term coming from the undulator field configuration. If we are able to interfere with the oscillation of this term, even through a small distance, the high linear growth rate at the harmonic might give rise to appreciable harmonic power. This motivates the idea of a complex undulator, the first part of which is a conventional helical undulator of length shorter than that required for saturation of the fundamental. In this way we promote appreciable bunching of the beam. The second part of the undulator is composed of a series of shorter sections with alternating helicities, which will suppress further growth of the fundamental and allow the remaining free energy of the electrons to flow into the harmonic fields.

3. Simulation

The model for numerical simulation is the set of FEL eqs. (1)–(4). We have investigated electron energy from 600–800 keV, and undulator strength a_w from 0.3–1.0, choosing different complex undulator field structures. The undulator period is set at 1.5 cm, the beam current density, 1600 A/cm², and the overall undulator length, 120 cm. We explored the first three harmonics in most examples; the fourth and fifth harmonics were observed in a few cases, but their power was rather small.

Fig. 1a shows the harmonic emission in a conventional helical undulator. The power of the second and the third harmonic is small and irregular, unlike the case of a linear undulator where only odd harmonics

are excited; the second harmonic power is always one order of magnitude greater than that of the third. The low harmonic power is due to the lack of a zeroth-order longitudinal modulation in electron motion in the helical undulator field. Increasing the pump strength can increase the harmonic power but does not stabilize the output power.

Figs. 2a and 2b show the harmonic generation at different beam energy (600 and 790 keV) in an undulator where the first "half" is a helical winding and the second "half" is composed of small sections of alternating helicity, each having three periods. Figs. 3a and 3b are harmonic power curves in an undulator where the first "half" is a helical winding and the second "half" is a sequence of linear-helical-linear-helical fields. In the mathematical model, the drastic change of undulator field is done by changing the relative phase among the shorter sections in the second portion

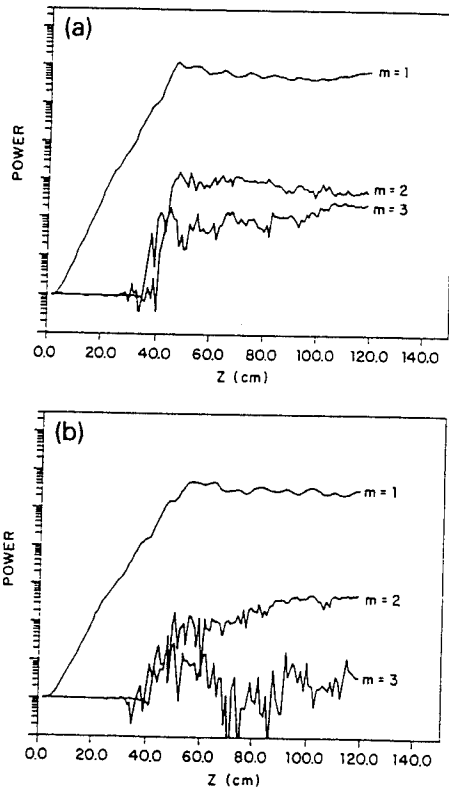


Fig. 2. (a) The fundamental, the second, and the third harmonic power in a "complex" undulator field (alternating helicity in the second half, starting at 23 cm); $a_w = 0.3$, $\lambda_w = 1.5$ cm, $\gamma_0 = 2.17$ (600 keV), $\lambda_s = 1.81$ mm, macro-period of the second half is $3\lambda_w$. (b) The first three harmonic power curves in the same undulator, but with different electron energy, $\gamma_0 = 2.55$ (790 keV), and $\lambda_s = 1.34$ mm.

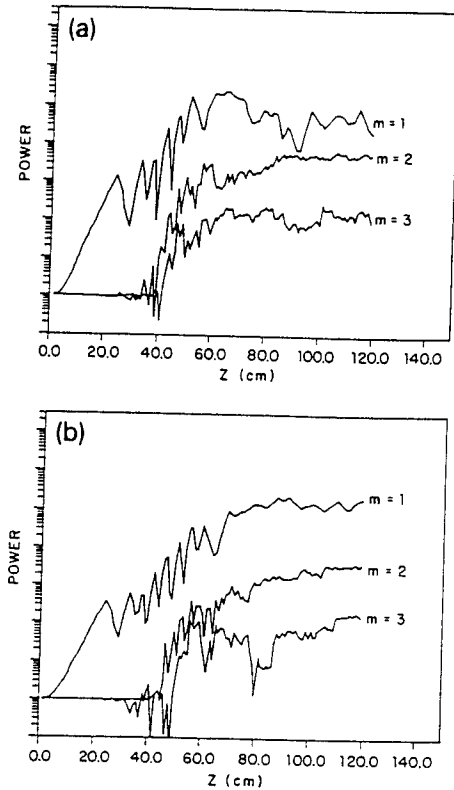


Fig. 3. (a) The fundamental, the second, and the third harmonic power in a "complex" undulator field (linear-helical-linear-helical... in the second half, starting at 23 cm); $a_w = 0.3$, $\lambda_w = 1.5$ cm, $\gamma_0 = 2.17$ (600 keV), $\lambda_s = 1.81$ mm, macro-period of the second half is $3\lambda_w$. (b) The first three harmonic power curves in the same undulator field, but with different electron energy, $\gamma_0 = 2.55$ (790 keV), and $\lambda_s = 1.34$ mm.

of the undulator. The harmonic power, especially the second, is significantly increased (by two orders of magnitude) in the second "half" of the undulator. Meanwhile, the fundamental radiation decreases, which means that some of the fundamental wave energy has flowed into the higher harmonics. More important, the harmonic power is not only increased but also stabilized; this makes possible the buildup of the harmonic power in an oscillator.

We found that changing the relative phase shift among the small sections in the second part of the undulator helps optimize the harmonic emission, but it does not change the power drastically. Also, the optimal structure of the undulator field depends on the injection energy of the electron beam. It is essential to insure the stability of electron trajectories; for the cases described here, the electrons are well-confined in the beam, even in the presence of a guide field ~ 1 T.

4. Conclusion

To sum up the results from the simulation show that harmonic power output can be improved, using a "complex" undulator, especially at twice the fundamental frequency. If the fundamental power is about 1 MW, we find the second harmonic power is about 10 KW, while the third is one order of magnitude smaller than the second, measured at the end of a single-pass FEL amplifier.

Acknowledgements

This research was supported by the ONR.

References

- [1] R.C. Davidson, in: *The Physics of Nonneutral Plasmas* (Addison-Wesley, 1990) section 7.11.
- [2] D.J. Bamford and D.A.G. Deacon, *Phys. Rev. Lett.* 62 (10) (1989) 1106.
- [3] R.W. Warren, L.C. Haynes, D.W. Feldman, W.E. Stein and S.J. Gitomer, *Nucl. Instr. and Meth.* A296 (1990) 84.
- [4] S. Benson, D.A.G. Deacon, J.N. Eckstein, J.M.J. Madey, K. Robinson, T.I. Smith and R. Taber, *J. Phys. (Paris) Coll.* 44 (1983) C1-353.
- [5] C.J. Elliott and M.J. Schmitt, *Nucl. Instr. and Meth.* A259 (1987) 177.
- [6] R. Bonifacio, L. de Salvo Souza, P. Pierini and E.T. Scharlemann, *Nucl. Instr. and Meth.* A296 (1990) 787.

A Free Electron Laser Experiment on "Angular Steering"

M. Cecere and T. C. Marshall

Abstract—A paper by Jerby [1] has discussed a number of mechanisms whereby FEL radiation may be directed electronically into different radiation patterns. We have devised an experiment [2] to test this concept using the Columbia microwave FEL, which amplifies radiation at 24 GHz to a level <1 MW. A 4 mm dia. electron beam (580 kV) is propagated in a guiding field of 0.8T inside an overmoded 24 mm dia. cylindrical waveguide. A TE₁₁ mode is grown in a 33 cm long first undulator section (period 3.36 cm), and upon entering the following undulator section (period 2.26 cm, length 40 cm), the electron bunches convert to TM₁₁ radiation which is further amplified. The far-field pattern of the TM₁₁ emitted power is distinct from the TE₁₁ pattern. Numerical and experimental studies are described in this paper showing the resulting radiation pattern.

I. INTRODUCTION

A PAPER by Jerby [1] has described a number of ways in which the power radiated by a Free Electron Laser (FEL) can be cast in different directions by electronic means. This is done by controlling the phasing of the bunches, or by coupling to different waveguide modes which have off-axis radiation patterns. His analysis treated the FEL in the "linear" regime; however, operation of the device typically involves saturated output, and so it is of interest to test this concept in the laboratory, as well as by numerical study. In particular, our work considers the particular application which he refers to as "angular steering," which we test in our microwave FEL. The electron beam is injected into a "buncher" undulator, which is followed immediately by a "radiator" undulator.

Conceptually, the technique can be understood as follows (see Fig. 1). In an FEL which uses a constant period helical undulator and a smooth-bore cylindrical waveguide, the dominant interaction occurs when the "beam line"

$$\omega = (k_z + k_w)\beta_{||}C - \omega_p/\gamma \quad (1)$$

intersects the "waveguide line," usually the circular TE₁₁ mode

$$\omega^2 = c^2(k_{\perp}^2 + k_z^2) = k_z^2 c^2 \quad (2)$$

as illustrated in the lower curve; in (1) we note the "Raman Shift" from the plasma frequency of the electrons. Here, k_z is the axial wavenumber of the radiation; $k_w = 2\pi/(\text{undulator}$

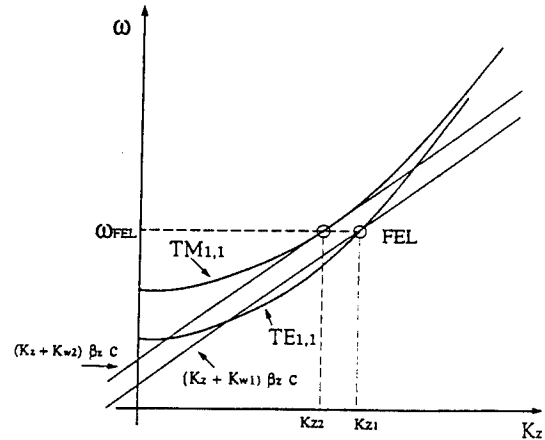


Fig. 1. Sketch of a dispersion plot, showing intersection (intersection points) of waveguide curves (parabolas) and the electron beam wave lines.

period, l_w); ω is the circular frequency; k_{\perp} is the transverse waveguide wavenumber; $\beta_{||}$ is the ratio of the axial component of electron speed to the speed of light, c ; and ω_p is the plasma frequency. The TE₁₁ radiation pattern is such that maximum power is radiated on the axis (Fig. 2(a)). We now add a refinement to this simple affair. Suppose the undulator were to be made of two sections, the first section having longer period than the second section. As the electron stream enters the first section of undulator, the TE₁₁ interaction builds up from noise or some low-level coherent source signal, and the beam becomes bunched. This beam now enters the second section of undulator, where the period is chosen so that the intersection with a higher order mode, say TM₁₁, occurs at the same frequency (Fig. 1). Then the bunched beam will rapidly develop an interaction with the TM₁₁ mode, which has a much different radiation pattern (Fig. 2(b)). The second undulator can be "switched on" electronically, and thereby the antenna pattern of the FEL will be changed (this is also described in Jerby's paper, see his Fig. 5). The experimental study of this is the purpose of this investigation.

There are potentially two flaws in this technique. First, one can appreciate that the upper beam line in Fig. 1 can still intersect the TE₁₁ mode at a yet higher frequency: this opens the possibility of a parasitic radiation. Secondly, the "switching" may not be complete in that both TM₁₁ and TE₁₁ radiations will be present in the output at the same frequency. We have encountered both these problems in this work, although we have also had success with the electronic switching of the radiation pattern. In what follows,

Manuscript received August 31, 1993; revised May 11, 1994. This work was supported by the ONR.

The authors are with the Department of Applied Physics, Columbia University, New York City 10027 USA.

IEEE Log Number 9405692D.

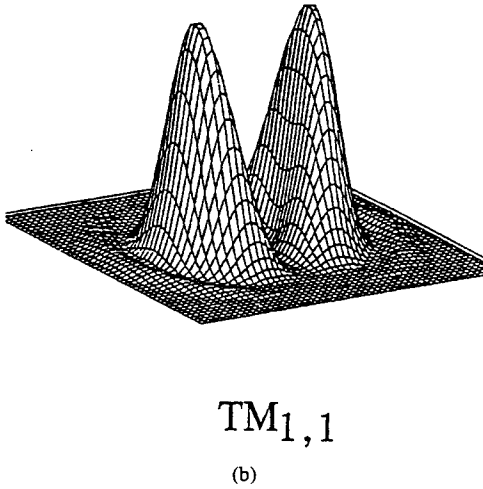
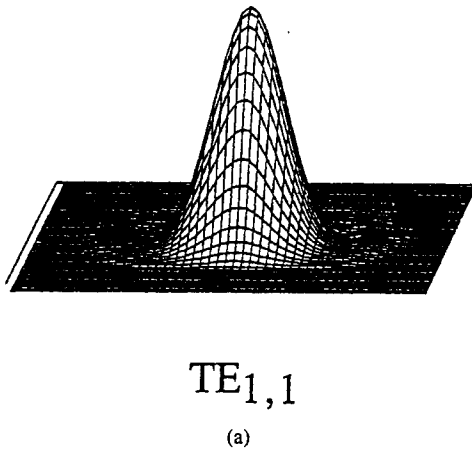


Fig. 2. (a) TE₁₁ radiation pattern; and (b) TM₁₁ radiation pattern from a conical horn, computed from reference [3].

we describe the numerical study we have done, and then discuss the experimental hardware, in particular the undulator. We conclude with our observation of the radiation pattern of the FEL.

II. THE EXPERIMENT

The equipment consists of a pulseline accelerator which provides a 150 nsec pulse of ~600 kV to a cold cathode in a diode geometry [4]; a cylindrical electron beam then flows down the axis of a drift tube (overmoded waveguide) surrounded by the helical undulator windings. Radiation is emitted by a conical horn, and is studied by a detector which can sense radiation in various directions (Fig. 3). This detector can be located inside a grating spectrometer, which then serves as a narrow-band filter, or it can detect the total power emitted. We operate the FEL as a travelling wave amplifier using a magnetron as a source of ~10 kW at 24 GHz. Beam focussing is provided by a solenoidal field of about 7.5 kG. Table I provides a list of the relevant experimental parameters.

To begin, the device was studied with a code [5] that simulates the set of three first order FEL differential equations which follow the particle energy, γ_j and phase, ψ_j , and the

TABLE I
OPERATING PARAMETERS

Electron Beam Energy	600 KeV	
Electron Pulse Length	150 nsec	
Electron Beam Diameter	4 mm	
Beam Current Density	~ 2 kA / cm ²	
Drift Tube (waveguide)	24 mm dia.	
Guiding Field	7800 Gauss	
FEL wavelength	1.25 cm, 24 GHz	
Undulator	1st Section	2nd Section
Period	3.36 cm	2.26 cm
Length	30 cm	40 cm
Fields	510 Gauss	390 Gauss
Parameter	aw = -0.5	aw = +0.5

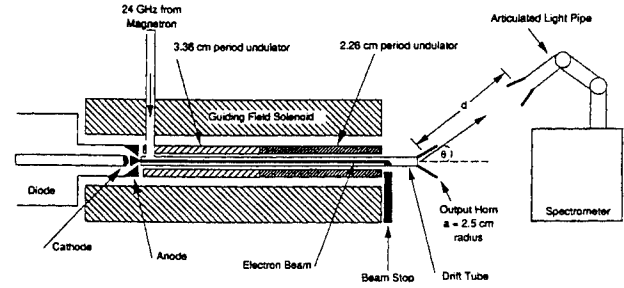


Fig. 3. Apparatus, showing FEL (approximately 1 m long) and spectrometer geometry.

radiation field amplitude, u :

$$\frac{d\gamma_j}{dz} = -\frac{k_s a_s a_w}{\gamma_j} \sin \psi_j + \frac{2\omega_p^2}{k_s c^2} [\langle \cos \psi \rangle \sin \psi_j - \langle \sin \psi \rangle \cos \psi_j] \quad (3)$$

$$\frac{d\psi_j}{dz} = k_w + k_s - \frac{\omega_s}{c} \left[1 - \frac{\mu^2 - 2a_w a_s \cos \psi_j}{\gamma_j^2} \right]^{-1/2} + \frac{\partial \phi}{\partial z} \quad (4)$$

$$\left(\nabla_{\perp}^2 + 2ik_s \frac{\partial}{\partial z} \right) u(r, z) = -\frac{\omega_p^2 a_w}{c^2} \left\langle \frac{e^{-i(\psi - \phi)}}{\gamma} \right\rangle \quad (5)$$

$$\psi_j = \int_0^{z_j} (k_s + k_w) dz' - \omega t + \phi. \quad (6)$$

The normalized vector potentials of the radiation and undulator fields are respectively $a_s = eE_s / K_s m c^2$, and $a_w = eB_{\perp} / k_w m c^2$, $\mu^2 = 1 + a_w^2$, and ϕ is the phase shift of the radiation field. This is a "zero slippage" computation which models the FEL as a travelling wave amplifier, given an input signal. In the code, 5000 "test" monoenergetic electrons are distributed uniformly at $z = 0$, on the axis as well as within the beam diameter. The orbit of the electron is represented by the parameter $a_w = \gamma v_{\perp} / c$.

In Fig. 4 we show a result which applies to the undulator that was finally built, for the electron energy of 600 kV. The input signal is TE₁₁, and this grows exponentially in the small-signal "linear" regime in the first 33 cm of the undulator. The amplitude of the radiation field (u) is represented by Bessel functions appropriate to the two modes under consideration, the TE₁₁ and the TM₁₁; the source term on the right hand

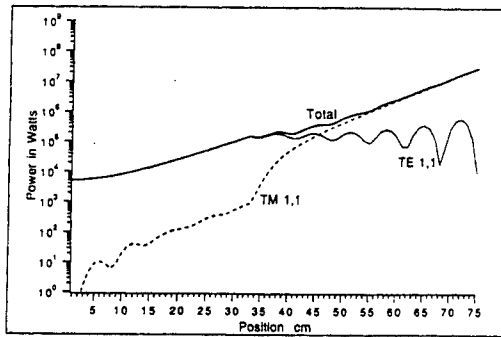


Fig. 4. Growth of radiation along the undulator (simulation); parameters are those given in Table I. In the simulation, the first undulator section ends at 33 cm and the second undulator section extends 40 cm beyond that.

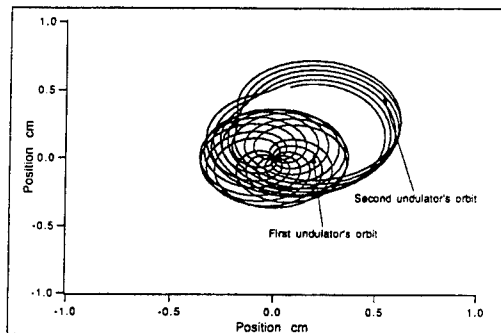
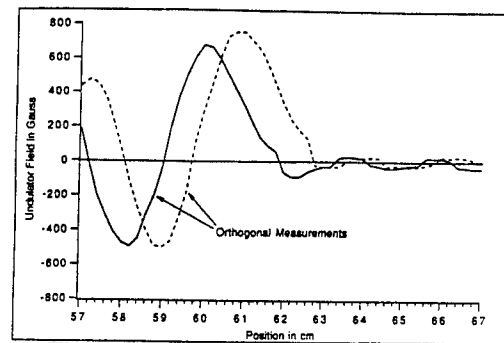


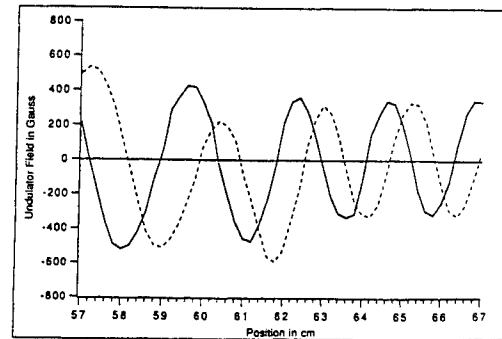
Fig. 5. Typical orbits showing Type I to Type II transition; electron starts motion at (0, 0) in the transverse plane. Parameters are given in Table I.

side of (5) drives both modes through the bunching current term (heavy brackets denoting the ensemble average over the injected electrons). There is some low-level excitation of the TM11 mode in the first undulator due to the progressive bunching of the electrons which is caused by the more powerful TE11 signal. This "prebunching" from the first undulator then causes a rapid buildup of the TM11 signal in the second undulator where the TM11 wave is resonant. The TE11 signal grows much less in the second section of the undulator, and would not grow further were it not for the overlap of the gain-bandwidths for each interaction. As the representative electrons used in the simulation move from the first into the second section of the undulator, the phase increments at a different rate, as given by (6), since k_w changes. This is an approximation to the more complex changes that should occur as the electron begins to move on a different trajectory (see Fig. 5 and discussion). Fig. 4 is the result of a choice of parameters which "optimizes" the growth of the TM11 radiation. Although the calculation shown in Fig. 4 shows that the signals are still in the linear regime of exponential growth at the end of the undulator, if we run the output to TM11 saturation, we find the TE11 signal remains at the low level it reached at the end of the first undulator section.

The need for a guiding field makes an interesting situation here. We compare the "undulator frequencies" in each section, $\beta_{||}c/l_w$, with the gyrofrequency of electrons in the guiding field, $eB_0/\gamma mc$. The latter is approximately 10 GHz at a field of 7.5 kG taking $\gamma \sim 2.1$, whereas in the first section the undulator frequency is 7.6 GHz and in the second section,



(a)



(b)

Fig. 6. (a) Undulator field, transition zone, "bucking" mode; (b) Same, but for both sections energized; the dotted line is for measurements taken with the pickup loop at 90° with respect to the orientation of the probe for the solid line.

11.4 GHz. The difference between the undulator frequency and the gyrofrequency has a large effect on the electron motion; in theory [6], the electron motion must switch between what is known as the "Type II" orbit into a "Type I" orbit as the electron moves from the first into the second section of the undulator. We have studied this effect using a code which follows the particle orbits in the undulator and guiding magnetic fields. Fig. 5 shows an electron that starts at $x, y = 0$ in the first section of undulator and spirals into the second section. The change of orbit at the transition is very apparent, but the electron does not hit the wall (radius = 12 mm) and the motion remains regular. In fact, studies of the electron propagation along the device using a "witness plate" showed no appreciable loss of intensity or change in beam shape.

The undulator was wound as a single turn bifilar helix which rests in a groove cut by a lathe screw-thread. The second section is composed of two windings, which permits the adjustment of the field in that section relative to the first. Two options were used—a "bucking" current mode, which gave nearly zero field in the second section, and a full current mode which was used when it was desired to generate the TM11 radiation. In Fig. 6(a) we show the transition region between the first and second sections when operated in the "bucking" mode, and in Fig. 6(b) the same region when both sections are driving a helical field. In the latter case, the transition is reasonably smooth. Magnetic measurements on the undulator were made with a small calibrated \vec{B} coil. The undulator also has an adiabatic entry zone, where the field

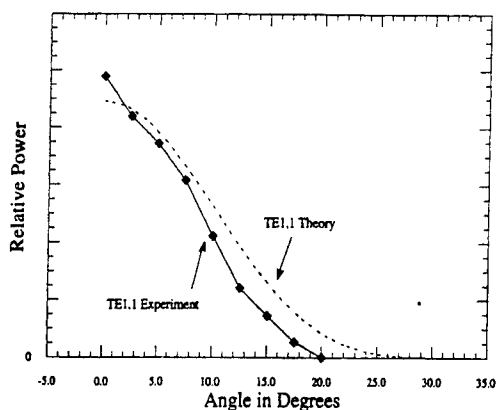


Fig. 7. Experimental radiation pattern of magnetron (no FEL radiation), with TE11 theory comparison.

builds up gradually over a few periods to its maximum (~ 500 G). The effective undulator parameter, $a_w = \gamma v_{\perp}/c$, is about 0.6 for each winding, taking into account the effect of the guiding field. The undulator is powered from a capacitor bank, the firing of which is timed with the accelerator so that the field maximum in the undulator occurs when the accelerator voltage pulse is present.

III. MEASUREMENTS OF RADIATION PATTERN

Operating conditions were chosen such that the FEL operated as an amplifier for the 24 GHz magnetron signal. This corresponded to operation at a diode voltage of approximately 580 kV and undulator fields of 510 G in the first section and 390 G in the second. However, it was noted that higher frequency radiations were occurring, possibly as an oscillator. Therefore, data was taken using our diffraction-grating spectrometer as a narrow band (~ 1 GHz) filter at 24 GHz. Referring to Fig. 3, the spacing between the radiating horn and the detecting horn is about 50 cm, which puts it in the Fraunhofer region ($\lambda/2a > 4a/d$, where a is the radius of the FEL horn aperture and d is the separation of the horns). This region is protected from reflections using microwave absorber pads. The receiving horn is on an articulated arm made up of 2.5 cm brass light pipe and two 90 degree reflectors, which permit swiveling the horn through an angle. The light pipe connects to a cylindrical taper (cutoff frequency 19 GHz), which then enters the spectrometer at the focal point of a polyethylene lens. The lens forms an approximately parallel wavefront microwave beam which is incident upon a "blazed" aluminum diffraction grating. Having reflected from the grating, the waves are focussed by a curved mirror onto a detector, which is provided with a small receiving horn. The resolution of the device was found to be about 5%, which is the reciprocal of the number of grating grooves illuminated (the groove spacing is 1.0 cm). The device is described in detail in reference [7]. Another detector fixed at $\theta = 0$ provides a signal monitor.

The measurement was first "calibrated" by observing the radiation pattern from the magnetron only; this is a TE11 mode which is launched into the cylindrical overmoded drift tube. This is presented in Fig. 7, which shows a forward-directed

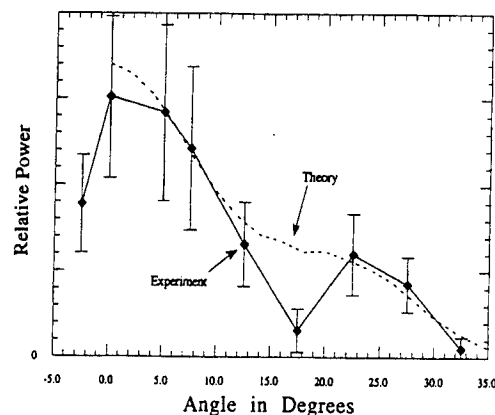


Fig. 8. FEL radiation pattern, with theory comparison, taking the total TM power to be 1.8 times as large as the TE power. The total power, as determined by a calibrated detector, is nearly 1 MW.

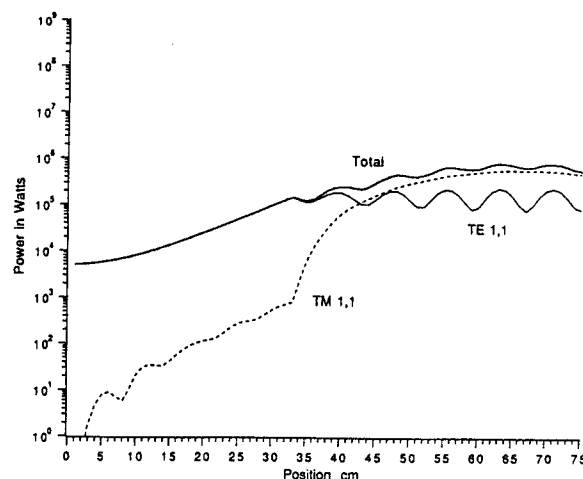


Fig. 9. Growth of radiation along the undulator: same conditions as Fig. 4, except that the electron energy is 583 kV.

power pattern with HWHM of nine degrees, in agreement with theory. Operating the first undulator section by itself does not change this radiation pattern. The 24 GHz signal radiated by the FEL with both undulator sections operating is shown in Fig. 8. There is first of all a new and distinctive feature which appears at $\theta = 23^\circ$, which is the predicted maximum of the off-axis TM11 mode pattern. However, the central feature characteristic of the TE11 radiation remains (note the TM11 pattern has a "hole" at $\theta = 0$). Our conclusion is the device is radiating a mixture of TE11 and TM11 radiation. A composite radiation pattern was calculated with a mixture of each type of radiation, and in Fig. 8 is shown the prediction of theory if the TM11 radiation is about twice as intense as the TE11 radiation. Apart from the discrepancy with the data at 17° , the fit is a good one.

Power measurements showed that the total power radiated by the device was under 1 MW, including possibly some radiation at a high frequency parasitic. However, Fig. 4 suggests the TM11 output should be much higher. While some of this discrepancy may be due to the simple numerical model (e.g. neglect of initial beam energy spread), another consideration

is that the experiment was actually run at a lower electron energy than that used in the simulation given in Fig. 4, which gave optimum output. A rerun of the numerical program at an electron energy of 583 kV shows that the TM11 power (~ 400 kW) is then predicted to be only about twice the TE11 power (Fig. 9). This shows the predicted power is very sensitive to the electron energy, which in any event we cannot measure to three significant figures.

REFERENCES

- [1] E. Jerby, "Angular steering of the free electron laser far field radiation beam," *Phys. Rev.*, vol. A41, pp. 3804–3811, 1990.
- [2] M. Cecere and T. C. Marshall, "A free electron laser experiment on angular steering," *Bull. Am. Phys. Soc.*, vol. 37, p. 1457, 1992.
- [3] Formulas used for the computation obtained from S. Silver, "Microwave antenna theory and design," *MIT Radiation Lab.*, New York: McGraw-Hill, 1949.
- [4] S. C. Chen and T. C. Marshall, "Parallel velocity spread induced in a relativistic electron beam by an undulator," *IEEE J. of Quantum Electron.*, vol. 21, pp. 924–930, 1985.
- [5] A. Bhattacharjee *et al.*, "Theory and observation of optical guiding in a free electron laser," *Phys. Rev.*, vol. A40, pp. 5081–5091, 1989.

- [6] L. Friedland, "Electron beam dynamics in combined guide and pump magnetic fields for free electron laser applications," *Phys. Fluids*, vol. 23, pp. 2376–2382, 1980.
- [7] J. A. Pasour and S. P. Schlesinger, "Multichannel grating spectrometer for millimeter waves," *Rev. Sci. Instrum.*, vol. 48, pp. 1355–1356, 1977.



M. Cecere was born in Farmingdale, NY on April 30, 1963. He received the B.S. in physics in 1985 from SUNY Oneonta, Oneonta, NY; the B.S. and M.S. in electrical engineering in 1986 and 1988 respectively from SUNY Buffalo, Buffalo, NY; and the M.S. in applied physics in 1993 from Columbia University, New York, N.Y.

He is presently working with Dr. Tom C. Marshall in the Free Electron Laser Laboratory at the Plasma Physics Lab of Columbia University.

T. C. Marshall, photograph and biography unavailable at time of publication.

Possibility of Generating a High-Power Self-Similar Radiation Pulse from a Free-Electron Laser

T. B. Zhang and T. C. Marshall

Department of Applied Physics, Columbia University, New York, New York 10027

(Received 5 August 1994)

Using 1D short-wavelength (8 μm) Compton free-electron-laser (FEL) equations with slippage, we explore propagation of a high-power pulse down a tapered undulator FEL traveling-wave amplifier. For an appropriate taper, a short pulse (~ 300 fsec FWHM) with regular features will propagate self-similarly as it grows in power, slipping through a much longer electron pulse. The power spectrum of the pulse is nearly Gaussian with no sidebands. The electron energy is depressed by $\sim 33\%$, but slippage causes the peak pulse intensity to be about the same as the electron-beam power density, $\sim 10 \text{ TW}/\text{cm}^2$.

PACS numbers: 41.60.Cr, 42.60.Jf

Under certain conditions, the free-electron-laser (FEL) oscillator has been found to provide an output of narrow, chaotic high-power "spike" pulses of radiation characterized by a wide irregular spectrum [1–3]. Furthermore, in the operation of a FEL oscillator, experiment [4] as well as numerical theory which carries the analysis well into the nonlinear regime [5] shows that the FEL can operate in a mode characterized by low efficiency together with a narrow spectrum, or in a mode that has higher efficiency and a wide spectrum. The latter has to do with the sideband instability [6] which has been observed experimentally [7,8] and which is also found in connection with superradiant spiking studies [9–13], since both [14] arise from slippage. However, there is also evidence that the sideband instability can be stabilized with an appropriately chosen taper of the undulator [15–17].

This Letter considers a traveling-wave, high-gain, Compton FEL which operates at nearly optimal efficiency using a variable-parameter undulator and which produces an intense "clean" output spike pulse with a nearly Gaussian spectrum free of sidebands. The hardware would include a laser "seed" source which supplies a high-power pulse having a Gaussian shape, as input to a high-efficiency FEL traveling-wave amplifier having an appropriately tapered undulator. Our findings are that one might expect to develop an infrared FEL pulse having peak power $\sim 10 \text{ TW}/\text{cm}^2$ and FWHM ~ 300 fsec using a 45 MeV, 150 A electron beam. We now develop a numerical model which establishes how such a FEL pulse can be prepared.

We shall study a short optical pulse which is propagating along a much longer pulse of electrons that is traversing an undulator. At FEL resonance, as the light wave moves down one undulator period, it slips ahead of the electrons by one optical wavelength λ_s . We shall study the case where the electron beam pulse is much longer than the overall slippage distance $L_s = N_w \lambda_s$, so that essentially no radiation appears ahead of or behind the electron pulse. (A number of recent publications have considered the wealth

of interesting effects which occur at the beginning and the end of the electron pulse, which involve "superradiance" [9–13].) We begin by studying a set of 1D equations which are appropriate for the Compton FEL:

$$\frac{\partial \gamma_j(x, y)}{\partial x} = -\frac{2\rho \gamma_j^2 A_s \sin \psi_j}{\gamma_j \beta_{j\parallel}}, \quad (1)$$

$$\frac{\partial \theta_j(x, y)}{\partial x} = \frac{1}{2\rho} \left[1 - \frac{k_s(1 - \beta_{j\parallel})}{k_w \beta_{j\parallel}} \right], \quad (2)$$

$$\frac{\partial A(x, y)}{\partial y} = i\gamma_r \left\langle \frac{e^{-i\theta}}{\gamma} \right\rangle. \quad (3)$$

The above equations are derived directly from the original 1D time-dependent FEL equations [6] by transforming the variables z and t into new independent variables x and y [9], i.e., $x = (ct - z)/l_c$, $y = (z - v_{\parallel}t)/l_c \beta_{j\parallel}$; here, $l_c = \lambda_s/4\pi\rho$ is the cooperation length which is defined as the minimum distance over which an electron may interact cooperatively with the radiation [10], $\rho = \gamma_r^{-1}(a_w \omega_p/4ck_w)^{2/3}$ is the Pierce parameter; $\beta_{j\parallel} = [1 - (\mu^2 - 2a_w a_s \cos \psi_j)/\gamma_j^2]^{1/2}$ is the axial velocity of the j th electron, $\mu^2 = 1 + a_w^2 + a_s^2$, a_w and a_s are the normalized vector potentials of the undulator ($eB_{\perp}/k_w mc^2$) and radiation field ($eE_s/k_s mc^2$); γ_j is the relativistic factor of the j th electron, $\psi_j = \theta_j + \phi$ is the relative phase of the j th electron with respect to the radiation pulse, $A(x, y) = A_s e^{i\phi}$ is the complex amplitude of the radiation pulse with $A_s = \omega_s a_s / \sqrt{\gamma_r \rho} \omega_p$, and ϕ is the phase shift of the radiation pulse. The angular brackets on the right-hand side of Eq. (3) indicate an ensemble average over all electrons. For the other quantities, γ_r is the resonant energy of electron in units of mc^2 , $k_w = 2\pi/l_w$ is the wave number of the undulator, and l_w is the undulator period; $k_s = 2\pi/\lambda_s = \omega_s/c$ is the wave number of the radiation pulse, λ_s is the radiation wavelength, l_w and λ_s satisfy the resonance condition $\lambda_s = l_w(1 + a_w^2)/2\gamma_r^2$, and $\omega_p = (4\pi e^2 n_e/m)^{1/2}$ is the plasma frequency for n_e electrons/cm³. The original FEL wave equations have been obtained assuming the field amplitude is a slowly varying function of time; this approximation has been

verified in the application for the short pulse propagation discussed here.

The numerical simulation is based on the computational model described by Eqs. (1)–(3). The FEL works as a traveling-wave amplifier. The spatial distribution of simulation electrons has a rectangular profile, the electrons are taken to be monoenergetic, and at the undulator entrance, they are uniformly distributed inside the beam length L_b with 1000 simulation electrons per radiation wavelength. For each wavelength-size “strip” of electrons, the relative phase location of the electrons with respect to the radiation field is uniformly distributed from $-\pi$ to π . The input radiation pulse is “seeded” inside the electron beam, with its initial amplitude $a_{s0} = 10^{-4}$ (200 MW/cm² at 8 μ m wavelength). The pulse profile and width can be varied so that we can study the evolution of various pulses. For the output format of the computational results, the electron-beam pulse and the radiation spike are plotted as the function of independent variables x and y , respectively, which implies two moving “windows” with the former at the speed of light c and the latter at the speed of electrons v_{\parallel} ; both are scaled in the units of the radiation wavelength λ_s from their leading edge. Since all these quantities are recorded at various undulator positions, these results will describe the time evolution of the pulses. In several test runs, we have carried out simulations for different FEL parameters, including different lengths of beam pulses and radiation pulses. Our results for superradiant pulse evolution are in a very good agreement with that of previous authors [9] and provide a calibration of our code.

Our main interest is to investigate an initial short radiation pulse propagating through a sufficiently long electron pulse. The initial radiation pulse has a Gaussian profile, shown in Fig. 1(a), and is injected into the rear part of the electron beam pulse; the peak of the initial pulse is located at $x = 225\lambda_s$. The radiation pulse starts from that position at the undulator entrance, and then moves toward the front of the electron pulse as it moves along the undulator. Shown in Fig. 1(b) is the Fourier-transformed spectrum, which has a central frequency $\omega_s = 2.36 \times 10^{14} \text{ sec}^{-1}$.

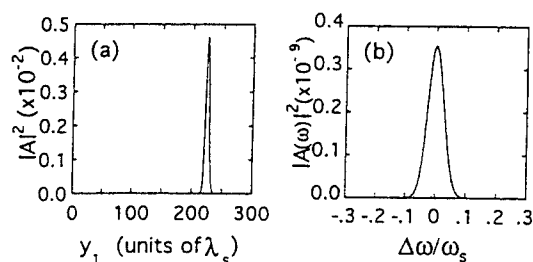


FIG. 1. The initial radiation pulse with a Gaussian profile, shown in (a), upon injection into a rectangular electron beam pulse, $y_1 = \beta_{\parallel} \ell_c y$. Shown in (b) is the Fourier-transformed spectrum; the central frequency is $\omega_s = 2.36 \times 10^{14} \text{ sec}^{-1}$ at $\Delta\omega = 0$.

TABLE I. Simulation parameters of radiation spike propagating in electron beam pulse.

Beam parameters	
Electron beam energy	$\gamma = 89.5$
Electron beam current	$I_b = 150 \text{ A}$
Beam intensity	5.4 TW/cm^2
Electron beam radius	$r_b = 0.02 \text{ cm}$
Beam pulse length	$L_b = 300\lambda_s$ (2.4 mm)
Undulator parameters	
Undulator period	$l_w = 2.5\text{--}1.5 \text{ cm}$; linear ramp
Undulator taper	$\eta = 2.6 \times 10^{-3} \text{ cm}^{-1}$
Undulator parameter	$a_w = 2.0$ (constant)
Undulator length	$N_w = 150$
Radiation pulse	
Radiation wavelength	$\lambda_s = 8.0 \mu\text{m}$
Spike length (FWHM, intensity)	$L_r = 12\lambda_s$
Initial pulse amplitude	$a_{s0} = 10^{-4}$ (200 MW/cm ²)
Peak spike amplitude	$a_s = 0.021$ (9 TW/cm ²)
Other parameters	
Pierce parameter	$\rho = 0.02$
Cooperation length	$l_c = 4.6\lambda_s$

Other simulation parameters of the FEL amplifier are listed in Table I, where a representative electron beam pulse length of 2.4 mm (~ 8 psec) is taken; the beam pulse is 300 wavelengths long, and so the optical pulse moves only halfway through as it traverses 150 undulator periods.

Figure 2 shows the pulse evolution in a constant period undulator ($l_w = 2.5 \text{ cm}$). The profiles of electron energy and the radiation spike together with its Fourier-transformed spectrum are shown at two undulator positions $N_w = 75$ [Figs. 2(a1)–2(a3)] and $N_w = 150$ [Figs. 2(b1)–2(b3)]. In these figures, the electron envelope is at rest and the optical spike propagates from the right to left as N_w increases. Figures 2(a2) and 2(b2) show that the optical pulse is amplified while the electron energy is reduced [Figs. 2(a1) and 2(b1)]. The “efficiency,” defined from the maximum drop in electron energy corresponding to maximum pulse intensity, is $\sim 10\%$, compared with the efficiency of a steady-state long continuous wave which is $\sim 3\%$. The radiation spike retains the initial profile until approximately 100 undulator periods where the growth becomes saturated. Saturation occurs when the loss of beam energy causes the interaction to drop out of resonance. A flat region and pulses beside the main spike develop from the two edges of the pulse after it propagates a long distance, and this causes a ragged energy profile [Fig. 2(b1)]. Figure 2(b3) shows a powerful long wavelength sideband comparable in intensity to the carrier; it has about the

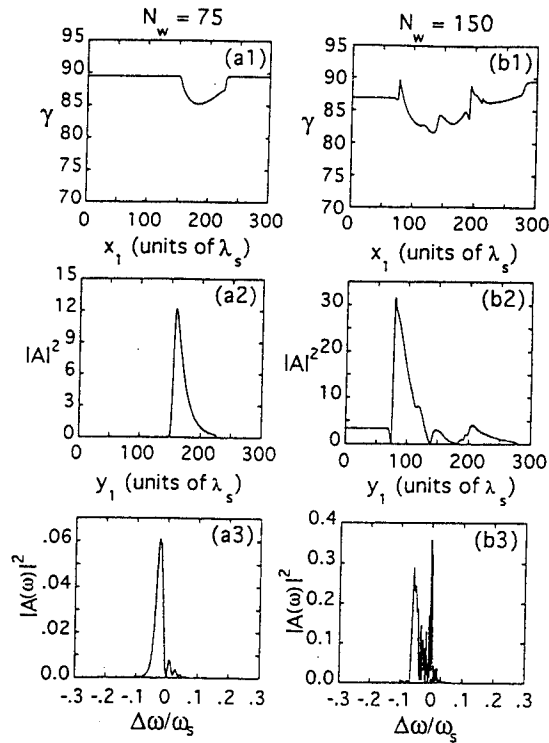


FIG. 2. Constant undulator period simulation. The radiation pulse slips forward into the electron beam from right to left, $x_1 = \ell_c x$. The beam energy distribution, radiation profile, and its Fourier-transformed spectrum (ordinate, arbitrary units) are shown in (a1)–(a3) at $N_w = 75$ and (b1)–(b3) at $N_w = 150$.

same displacement from the carrier [6] as the sideband instability.

If the undulator is tapered, we expect the growth of the sideband can be suppressed, and in Fig. 3 we show the results. The undulator period is linearly tapered from 2.5 to 1.5 cm in 150 periods. All other conditions are the same as in Fig. 2 and are obtained from Table I. In this numerical experiment, we did not optimize the undulator taper to pursue the highest efficiency enhancement: Instead, the appropriate taper was chosen for the purposes of obtaining the cleanest spike (however, this optimized taper is not very different from the taper which extracts maximum energy from the beam). Unlike the untapered cases, the radiation pulse at high amplitude does not radically change its shape, but displays a self-similar profile throughout the slippage region. The width of the initial Gaussian pulse is $\text{FWHM} \sim 7\lambda_s$ in intensity; it evolves and becomes broadened to about $\text{FWHM} \sim 12\lambda_s$ during the first 50 periods; it continues to grow in amplitude while keeping a nearly constant profile and width. We have tried various widths of the initial Gaussian pulse, as well as a different initial amplitude profile varying as $\sim 1/\cosh(\alpha y)$ (a solitary wave solution [18]), and we find the variation of initial choices converges to a similar output pulse profile and width, although the number of undulator periods needed to form the self-similar pulse profile may vary. This suggests that

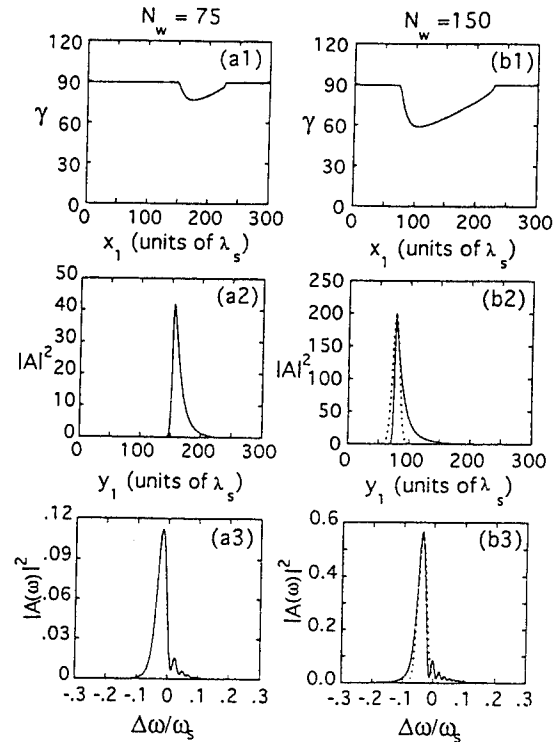


FIG. 3. The parameters are the same as in Fig. 2 except that the undulator period is linearly tapered from 2.5 to 1.5 cm. When the radiation spike slips over the electron beam, the beam energy is continuously extracted (a1) and (b1), while the spike keeps a self-similar profile (a2) and (b2). Its Fourier-transformed spectrum (amplitude in arbitrary units) is shown in (a3) and (b3). A Gaussian comparison pulse (dotted curves), described in the text, is shown in (b2), and its Fourier transform appears in (b3).

a short optical pulse may eventually evolve to a self-similar spike in the slippage region of the tapered undulator. The characteristic width of the spike is similar to the prediction of the Ginzburg-Landau solitary wave theory [19]. In the constant period undulator, the self-similar feature is lost when the FEL system goes out of resonance.

We should expect an efficiency enhancement in the tapered undulator. Comparing Fig. 3(b2) with Fig. 2(b2), one finds the efficiency is roughly a factor of 3.3 better than the same FEL with constant-period undulator. The maximum value of the normalized field amplitude $a_s = 0.021$ ($\sim 9 \text{ TW/cm}^2$) corresponds to an intensity of the same order as the beam kinetic energy intensity; this enhancement in power is caused by the slippage of the radiation pulse over “new” electrons as it moves down the undulator. Now the ragged profile of the electron energy in the constant undulator [Fig. 2(b1)] is found to disappear in the tapered undulator [Fig. 3(b1)]. The strong intensity of the spike forms a very deep potential well which may trap most of electrons even though they have an energy spread. The maximum bucket height $\delta\gamma_{\text{max}}$ may be obtained from $\delta\gamma_{\text{max}}/\gamma_r = 2\sqrt{a_w a_s}/\mu$, which gives the value of $\delta\gamma_{\text{max}} = 10$ at $N_w = 75$

and $\delta\gamma_{\max} = 12.5$ at $N_w = 150$. In this case, it is the undulator taper which helps maintain the resonant wave-particle interaction.

The choice of the $8\text{ }\mu\text{m}$ wavelength was arbitrary although this is representative of FEL performance with the chosen beam parameters. (The same qualitative features were obtained in another tapered undulator FEL simulation for a much lower beam energy and wavelength of 1.5 mm .) Considering diffraction, a Rayleigh range of about one-half the undulator length would require an optical beam larger than the electron-beam diameter we have chosen, or a shorter wavelength. Because of the large optical intensity achieved, one would not expect optical guiding to be effective beyond the region of exponential growth [20].

Finally, the sideband is suppressed in the tapered undulator FEL, as shown in Figs. 3(a3) and 3(b3). In this case, we have a comparatively clean spike in both time and frequency domains. Note also there is a frequency shift from the resonance in these spectra. Frequency shifting is an intrinsic characteristic of the time-dependent FEL equations [21]. We may estimate the frequency shift from the computed phase shift $\phi(x, y) = -i \ln(A/A_s)$, and $\Delta\omega/\omega_s = 2\rho \partial\phi/\partial x$, obtaining the values of $\Delta\omega/\omega_s = -0.014$; -0.032 at the two undulator positions $N_w = 75$; 150 which agree approximately with the numerical results. In Fig. 3(b2) is also shown a comparison Gaussian pulse having the same amplitude and FWHM as the self-similar pulse; in Fig. 3(b3) we find the Fourier transform of this comparison pulse (also Gaussian) is a rather good fit to the spectrum of the self-similar pulse. The solitary wave $1/\cosh(\alpha y)$ solution is also very close to the Gaussian fit.

In conclusion, we have found that injection of a single short radiation pulse into a long electron-beam pulse at the input of a tapered undulator traveling-wave FEL amplifier should result in the development of an intense spike which is comparatively clean in both time and frequency domains, and which propagates in a self-similar way along the undulator. Because of the slippage, the peak pulse intensity is enhanced and is of the same order as the electron-beam intensity. Since the pulse spectrum is regular and nearly Gaussian, the output pulse from the FEL is useful for technical applications and indeed might be compressed and intensified even further using standard optical techniques.

This work is sponsored by the Office of Naval Research.

-
- [1] R. W. Warren, J. C. Goldstein, and B. E. Newnam, Nucl. Instrum. Methods Phys. Res., Sect. A **250**, 19 (1986).
 - [2] B. A. Richman, J. M. J. Madey, and E. Szarmes, Phys. Rev. Lett. **63**, 1682 (1989).
 - [3] J. W. Dodd and T. C. Marshall, IEEE Trans. Plasma Sci. **PS-18**, 447 (1990).
 - [4] D. Iracane, V. Fontenay, P. Guimbal, S. Joly, S. Striby, and D. Touati, Phys. Rev. Lett. **72**, 3985 (1994).
 - [5] D. Iracane and J. L. Ferrier, Phys. Rev. Lett. **66**, 33 (1991).
 - [6] N. M. Kroll, P. L. Morton, and M. N. Rosenbluth, IEEE J. Quantum Electron. **QE-17**, 1436 (1981).
 - [7] R. W. Warren, B. E. Newnam, and J. C. Goldstein, IEEE J. Quantum Electron. **QE-21**, 882 (1985).
 - [8] F. G. Yee, J. Masud, T. C. Marshall, and S. P. Schlesinger, Nucl. Instrum. Methods Phys. Res., Sect. A **259**, 104 (1987).
 - [9] R. Bonifacio, B. W. J. McNeil, and P. Pierini, Phys. Rev. A **40**, 4467 (1989).
 - [10] R. Bonifacio, N. Piovela, and B. W. J. McNeil, Phys. Rev. A **44**, 3441 (1991).
 - [11] W. M. Sharp, W. M. Fawley, S. S. Yu, A. M. Sessler, R. Bonifacio, and L. DeSalvo Souza, Nucl. Instrum. Methods Phys. Res., Sect. A **285**, 217 (1989).
 - [12] G. T. Moore and N. Piovela, IEEE J. Quantum Electron. **QE-27**, 2522 (1991).
 - [13] S. J. Hahn and J. K. Lee, Phys. Rev. E **48**, 2162 (1993).
 - [14] R. M. Caloi, Phys. Rev. A **46**, 7934 (1992).
 - [15] F. G. Yee, T. C. Marshall, and S. P. Schlesinger, IEEE Trans. Plasma Sci. **PS-16**, 162 (1988).
 - [16] B. Hafizi, A. Ting, P. Sprangle, and C. M. Tang, Phys. Rev. A **38**, 197 (1988).
 - [17] R. P. Pila and A. Bhattacharjee, Phys. Plasmas **1**, 390 (1994).
 - [18] S. Y. Cai and A. Bhattacharjee, Phys. Rev. A **43**, 6934 (1991).
 - [19] Li-Yi Lin and T. C. Marshall, Phys. Rev. Lett. **70**, 2403 (1993).
 - [20] E. T. Scharlemann, in *Free Electron Lasers*, edited by W. Colson, C. Pellegrini, and A. Renieri, Laser Handbook Vol. 6 (North Holland, Amsterdam, 1990).
 - [21] G. Shvets and J. S. Wurtele, Phys. Plasmas **1**, 157 (1994).